REAL TIME IN SITU X-RAY STUDIES OF ORGANIC HETEROSTRUCTURE FORMATION

A Dissertation

Presented to the Faculty of the Graduate School

of Cornell University

in Partial Fulfillment of the Requirements for the Degree of

Doctor of Philosophy

by

Edward Robert Kish

August 2014

REAL TIME IN SITU X-RAY STUDIES OF ORGANIC HETEROSTRUCTURE FORMATION

Edward Robert Kish, Ph.D.

Cornell University 2014

This thesis presents several studies of the deposition and growth of thin films of organic semiconductors and the formation of organic-organic heterostructures. Organic semiconductors are of great interest due to their usefulness in electronic, optical and photovoltaic devices, compatibility with flexible substrates, and they can be processed at low temperatures compared to traditional, inorganic semiconductors. Thus, they are desirable for low cost device applications such as transistors, OLEDs, and photovoltaics. An organic photovoltaic device requires combining two different organic semiconductors into a single structure. An interface between a donor material and an acceptor material is necessary for a functioning organic photovoltaic device. In this work, the use of supersonic molecular beams to deposit organic thin films of pentacene and diindenoperylene on SiO_2 is directly compared to the use of thermal evaporation, and the effects on the nucleation of organic thin films are examined. Incident kinetic energy is found to have no influence on the critical nucleus size for pentacene and diindenoperylene. Supersonic molecular beams and in situ synchrotron x-ray scattering are used to investigate the mechanism of adsorption and dynamics of thin film growth of three perylene derivatives: N,N′-dipentylperylene-3,4,9,10-tetracarboxylic diimide (PTCDI-C_5), N,N′-dioctylperylene-3,4,9,10-tetracarboxylic diimide (PTCDI-C_8), and N,N′-ditridecylperylene-3,4,9,10-tetracarboxylic diimide (PTCDI-C_{13}) on

surfaces modified with organic self-assembled monolayers. Small changes in molecular structure, like changing the length of alkyl side chains on PTCDI-C_n molecules, results in significant changes for thin film growth. Shorter side chains result in smoother, more prolonged layer by layer growth. This thesis also reports on the growth of heterostructures of two different organic semiconductors, both simple bilayer stacks and more complex multilayer structures. While growth of PTCDI-C_n on films of pentacene results in smooth layer-by-layer growth, when pentacene is deposited on PTCDI-C_n films, the resulting films are extremely rough, and exhibit Volmer-Weber growth. When growing heterostructures by depositing alternating layers of pentacene and PTCDI-C_n, this effect causes increases in roughness after the deposition of pentacene. Interestingly, the roughness can be decreased after depositing a layer of PTCDI-C_n. This behavior suggests that the two materials are forming separate domains rather than a superlattice structure, which could be favorable for photovoltaic devices. This behavior is driven by differences in surface energy of pentacene and PTCDI-C_n. This result has implications for future work attempting to form heterostructures of two different organic semiconductors, highlighting the important of surface energy considerations.

BIOGRAPHICAL SKETCH

Edward was born in Mt. Laurel, New Jersey. He later moved to Pipersville, Pennsylvania and graduated third in his class from Central Bucks High School East in 2003. After this, he attended the Johns Hopkins University in Baltimore, Maryland. Edward graduated with honors, completing a Bachelor of Science degree with a double major in Chemical and Biomolecular Engineering and Physics. After graduating in January 2007, he began his graduate studies at Cornell University later that year. He completed his PhD in April 2014.

To my family, friends,

and everyone who believed

ACKNOWLEDGEMENTS

First, I want to thank the entire Engstrom Research Group, starting with my advisor, Prof. James R. Engstrom. His depth of knowledge and exacting standards have inspired my work and professional outlook. I also want to thank my fellow graduate students. Dr. Kevin Hughes showed me how to run a vacuum system. Dr. Tushar Desai . I want to thank Rambert Nahm for his help running and designing experiments at CHESS. Wenyu Zhang, Jiun-Ruey Chen and Jade Noble have all provided both assistance in the lab, and insight during research discussions. As well as the graduate students, I have had a few undergraduate researchers who were a great help to me, particularly Doug Greer and Harris Karsch. I also need to thank Dr. Arthur Woll for his guidance and expertise; I couldn't have survived a CHESS run without them.

I want to thank my family and friends for their unwavering support and encouragement.

I also gratefully acknowledge financial support from the Intel Foundation and Semiconductor Research Corporation Education Alliance. I would like to also recognize the experimental facilities that made my research possible, as well as their staff: CNF, CCMR, NBTC and CHESS.

TABLE OF CONTENTS

LIST OF TABLES

LIST OF FIGURES

CHAPTER 1

INTRODUCTION

In this thesis, I present studies of the thin film deposition of small molecule organic semiconductors and the fabrication of heterostructures of donor and acceptor molecules. Organic semiconductors are of great interest due to their usefulness in electronic, optical and photovoltaic devices and compatibility with flexible substrates. Additionally, as they can be processed at low temperatures compared to traditional, inorganic semiconductors (e.g. Si, GaAs), and can potentially be deposited via novel roll-to-roll methods, organic semiconductors show promise for use in low cost devices **[1,2]**. Potential device applications include flexible electronics, display technologies, sensors and photovoltaics. In contrast to inorganic materials, the bonds between organic semiconductor molecules are formed by weak, van der Waals interactions, and may crystallize in different phases, making epitaxial growth difficult. Due to this, it is possible to tune organic thin film growth by changing deposition techniques, substrates, process parameters, or the chemical structure of the molecule itself.

Organic semiconductors are classified as electron donors or electron acceptors, analogous to inorganic *p*-type or *n*-type semiconductors, based on whether the majority carriers are holes or electrons, respectively. Organic semiconductors are also split into small molecules (e.g. pentacene, C_{60}) and polymers (e.g. poly(3-hexylthiophene)). Polymers are typically deposited in the solution phase, while small molecules are deposited via vapor phase or solution phase (if the molecule is soluble). For both types, the best device performance is achieved when the molecules form a well-ordered crystal structure free from defects. In this work, the deposition of small molecules from the vapor phase is studied.

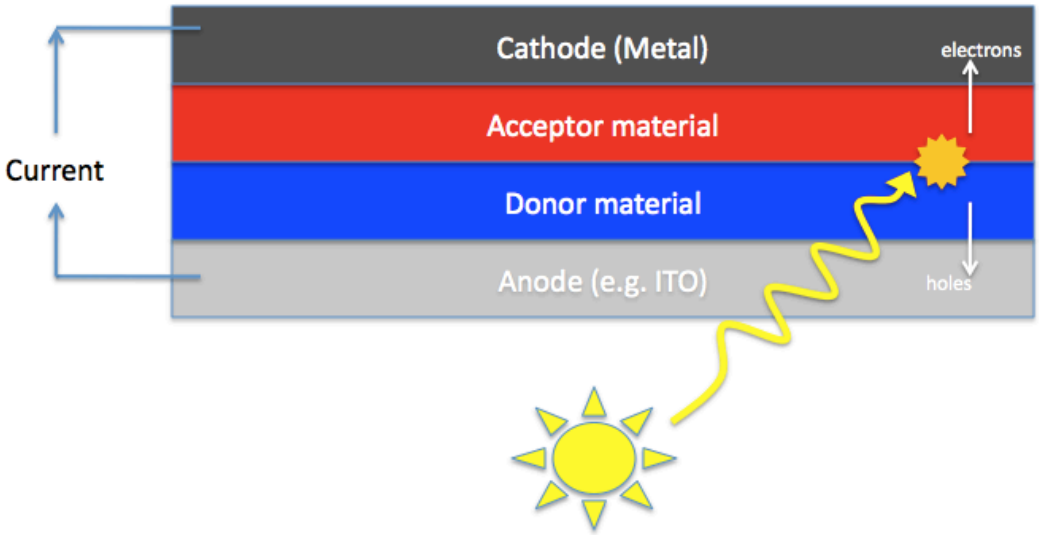

Figure 1.1: A schematic representation of an organic photovoltaic device. Light enters through the transparent anode (typically indium tin oxide) and is absorbed by the active layer to create an electron hole pair (exciton). The pair is split at the interface, with the hole being transported to the anode and the electron to the cathode, generating electric current.

An organic photovoltaic device is shown schematically in Figure 1.1. The device consists of a donor layer and an acceptor layer sandwiched between two electrodes. The device operates by absorbing a photon in the active layer, which promotes an electron to a higher energy level, leaving a hole behind. This electron-hole pair is referred to as an exciton. Unlike inorganic semiconductors, the electron and hole are localized and must be separated. At the interface between the donor and acceptor materials, the exciton can dissociate into a single electron and hole, which can then conduct through the acceptor and donor materials to the electrodes, creating current. It is critical for photovoltaic device operation to have both an interface between donor and acceptor layers and a continuous path to the electrodes **[3,4]**.

Similarly, studies of organic thin film transistors (OTFTs) have shown that the interface between the organic film and the dielectric is critical to charge transport, and the majority of carriers are generated in the first few monolayers (MLs) of the organic layer **[5-9]**. The properties of the interface will have a significant impact on growth and eventual device performance. This has been shown in studies of organic semiconductors deposited on self-assembled monolayers improving OTFT performance **[8-13]**. The precise causes of these improvements are still unclear, and a better understanding of interface formation is desirable.

Vapor phase deposition of organic semiconductors is typically done via thermal evaporation. Molecules are then incident on the substrate at thermal kinetic energies (e.g. 0.05 to 0.1 eV). The parameters most commonly used to control growth are growth rate and substrate temperature. An additional parameter that can be adjusted is the kinetic energy of the incident molecules. This can be controlled by using a supersonic molecular beam. Using a supersonic molecular

beam, the molecules are incident on the surface at hyperthermal energies (e.g. 1 to 15 eV). Details on supersonic molecular beams can be found in Sections 1.4 and 2.1.

This thesis discusses the effects of incident kinetic energy, both thermal and hyperthemal, and the nature of dielectric substrate (clean SiO_2, or SiO_2 modified with SAMs of varying thickness and chemical functionality) on the thin film processes occurring at the organic/dielectric interface. These processes include adsorption, nucleation and diffusion, and the filling of individual monolayers during growth. Additionally, the formation of heterostructures of donor and acceptor layers is studied. Two different donor molecules are considered: pentacene and diinenoperylene (DIP). Three different acceptor molecules are considered: N,N-dipentylperylene-2,4,9,10-tetracarboxylic diimide (PTCDI-C_5), N,N-ditoctylperylene-2,4,9,10-tetracarboxylic diimide (PTCDI-C_8),and N,N-ditridectylperylene-2,4,9,10-tetracarboxylic diimide (PTCDI-C_{13}). The structures of these molecules can be seen in Figure 1.2. Chapter 3 focuses on the effect of incident kinetic energy on the nucleation dynamics of pentacene and DIP deposited on SiO_2. Chapter 4 concerns the effects of kinetic energy and adsorption dynamics of PTCDI-C_5 and PTCDI-C_8 on surfaces modified with SAMs. Chapter 5 discusses the growth of the three perylene molecules on thin films of pentacene as well as the reverse: pentacene growth on thin films of PTCDI-C_n. Additionally, the growth of more complicated multilayer structures of PTCDI-C_n and pentacene will be discussed.

1.1 Organic semiconductors investigated

The five organic semiconductors examined in this work (see Figure 1.2) can be divided into donors and acceptors. The two donor molecules, pentacene and DIP, are similar, both being composed of fused benzene rings. The three acceptor molecules are very similar. Each has the same conjugated, perylene core, and alkyl side chains. The molecules differ only in the length of these side chains, ranging from 5 to 13 methyl groups.

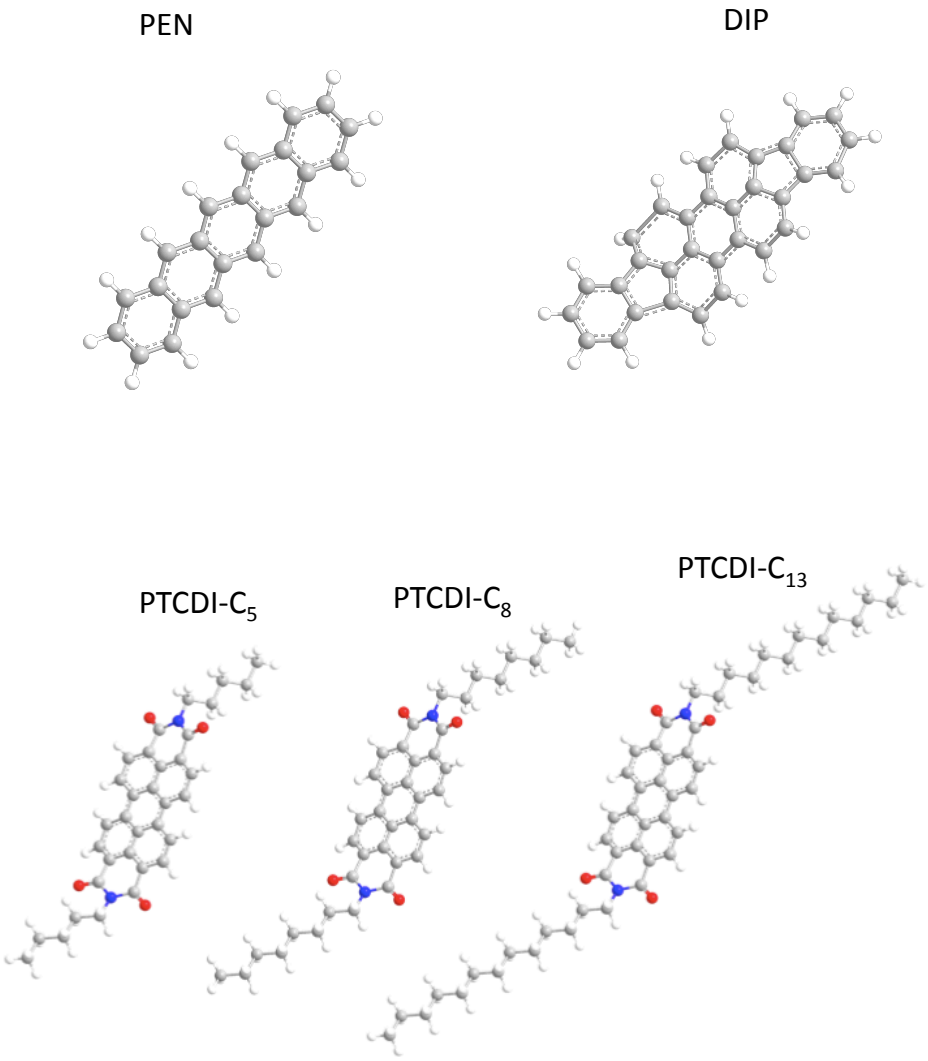

Figure 1.2: Ball and stick models of the five organic semiconductors studied in this work. Carbon atoms are gray, hydrogen atoms are white, oxygen atoms are red, nitrogen atoms are blue

1.1.1 Pentacene

The space filing model of pentacene is shown in Figure 1.2. Pentacene is one of the most widely studied organic semiconductors. It is a planar molecule composed of five fused benzene rings. It has a chemical formula of $C_{22}H_{14}$ with a molecular weight of 278 g/mol. It contains only carbon and hydrogen. Pentacene displays *p*-type semiconducting behavior, with a hole mobility as high as 3.3 cm^2-V^{-1}-s^{-1} reported **[14]**. Pentacene is known to form two crystal phases: a bulk phase and a thin film phase. In both phases, the molecule stands upright with its long axis perpendicular to the substrate. The difference is the tilt angle, resulting in different d-spacings: 15.4 Å for the thin film phase and 14.4 Å for the bulk. The crystal parameters for both phases can be found in Table 1.1.

1.1.2 Diindenoperylene (DIP)

The space filling model of DIP is shown in Figure 1.2. DIP is a planar molecule with a perylene core and two side indeno groups. It has a chemical formula of $C_{32}H_{16}$ with a molecular weight of 400 g/mol. Like pentacene, it contains only carbon and hydrogen and exhibits *p*-type semiconducting behavior with a mobility of up to 0.12 cm^2-V^{-1}-s^{-1} reported **[15]**. In the thin film phase, DIP stands upright with the long molecular axis oriented perpendicular to the surface. The crystal structure of DIP is shown in Table 1.1.

1.1.3 N,N′-dipentylperylene-3,4,9,10-tetracarboxylic diimide (PTCDI-C_5)

The space filling model of N,N′-dipentylperylene-3,4,9,10-tetracarboxylic diimide (PTCDI-C_5) is shown in Figure 1.2. This molecule consists of a perylene core and two 5 carbon alkyl side chains. The chemical formula is $C_{34}H_{30}N_2O_4$ with a molecular weight of 530 g/mol. It contains carbon, hydrogen, oxygen and nitrogen. It exhibits *n*-type semiconducting behavior with electron mobilities as high as 0.1 cm^2-V^{-1}-s^{-1} reported **[16]**. PTCDI-C_5 stands upright with the long molecular axis oriented perpendicular to the substrate and exhibits both a thin film and bulk phase. The crystal parameters for PTCDI-C_5 are listed in Table 1.1.

1.1.4 N,N′-dioctylperylene-3,4,9,10-tetracarboxylic diimide (PTCDI-C_8)

The space filling model of N,N′-dioctylperylene-3,4,9,10-tetracarboxylic diimide (PTCDI-C_8) is shown in Figure 1.2. This molecule consists of a perylene core and two 5 carbon alkyl side chains. The chemical formula is $C_{46}H_{42}N_2O_4$ with a molecular weight of 686 g/mol. It contains carbon, hydrogen, oxygen and nitrogen. It exhibits *n*-type semiconducting behavior with electron mobilities as high as 0.6-1.7 cm^2-V^{-1}-s^{-1} reported **[17,18]**. PTCDI-C_8 stands upright with the long molecular axis oriented perpendicular to the substrate and exhibits both a thin film and bulk phase. The crystal parameters for PTCDI-C_8 are listed in Table 1.1.

	a (Å)	b (Å)	c (Å)	α (deg)	β (deg)	γ (deg)
Pentacene **[19]**	6.266	7.775	14.530	76.475	87.682	84.684
Pentacene (thin film) **[20]**	7.58	5.91	15.43			90
DIP **[21]**	11.66	13.01	14.97	98.44	98.02	114.54
DIP (thin film) **[22]**	8.55	7.09	16.6			90
PTCDI-C_5 **[23]**	4.754	8.479	16.296	86.88	83.50	83.68
PTCDI-C_5 (thin film) **[23]**			18.3			
PTCDI-C_8 **[24]**	9.00	4.89	21.65	95.0	100.7	112.8
PTCDI-C_8 (thin film)**[24]**	8.50	4.68	19.72	88.43	94.01	97.21
PTCDI-C_{13} **[25]**	4.661	8.592	25.31	86.38	85.786	82.473

Table 1.1: Crystal structures of the organic semiconductors studied in this work.

1.1.5 N,N'-ditridecylperylene-3,4,9,10-tetracarboxylic diimide (PTCDI-C_{13})

The space filling model of N,N'-ditridecylperylene-3,4,9,10-tetracarboxylic diimide (PTCDI-C_{13}) is shown in Figure 1.2. This molecule consists of a perylene core and two 13 carbon alkyl side chains. The chemical formula is $C_{50}H_{62}N_2O_4$ with a molecular weight of 754 g/mol. It contains carbon, hydrogen, oxygen and nitrogen. It exhibits *n*-type semiconducting behavior with electron mobilities as high as 2.1 cm^2-V^{-1}-s^{-1} reported **[25]**. Like the other molecules studied here, PTCDI-C_{13} stands upright with the long molecular axis oriented perpendicular to the substrate. The crystal parameters for PTCDI-C_{13} are listed in Table 1.1.

1.2 Dielectric materials: self-assembled monolayers

Self-assembled monolayers (SAMs) are an organized layer of molecules formed spontaneously by the adsorption of a molecule on a solid surface. Each molecule consists of three components: an active headgroup which chemically bonds to a suitable substrate (in this case SiO_2), a functional tailgroup which can provide a variety of surface terminations, and the backbone which permits the ordering of a layer by van der Waals interactions with neighboring molecules. By fabricating SAMs of different backbone lengths and tailgroups, the chemical and physical nature of the resulting surface can be easily controlled. Figure 1.3 shows a schematic representation of a typical SAM. A good review on SAMs can be found in reference **[26]**. Figure 1.4 shows space-filling models of the SAMs studied in this thesis. For each of the SAMs studied here, the headgroup is a trichlorosilane group (R-$SiCl_3$). This trichlorosilane group reacts with the hydroxyl groups on the SiO_2 surface to form Si-O-Si linkages.

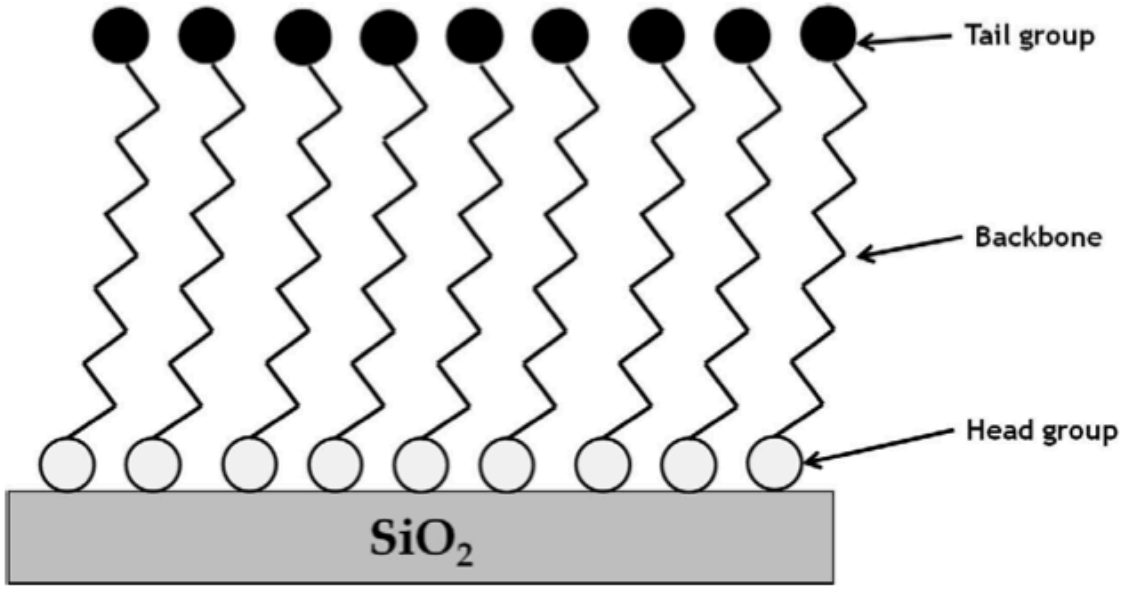

Figure 1.3: Diagram showing a self-assembled monolayer (SAM) deposited on SiO_2, with the three components of the SAM labeled: the headgroup, backbone and tailgroup.

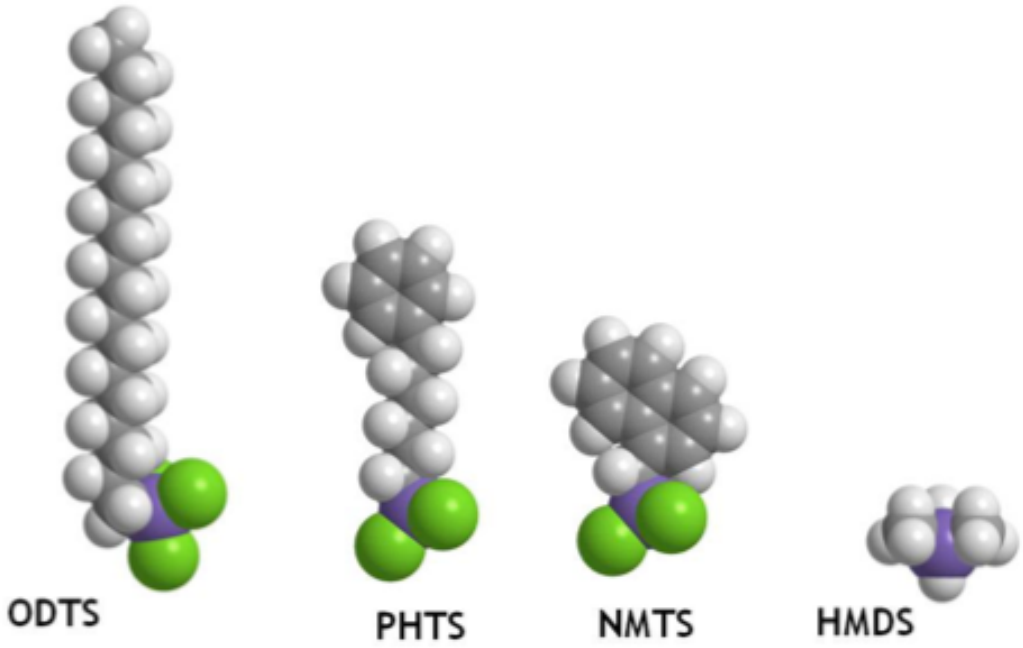

Figure 1.4: Space filling models of the self-assembled monolayers studied in this work. From left to right: octadecyltrichlorosilane (ODTS), 6-phenylhexyltrichlorosilane (PHTS), 1-napthylmethyltrichlorosilane (NMTS), and hexamethyldisilizane (HMDS).

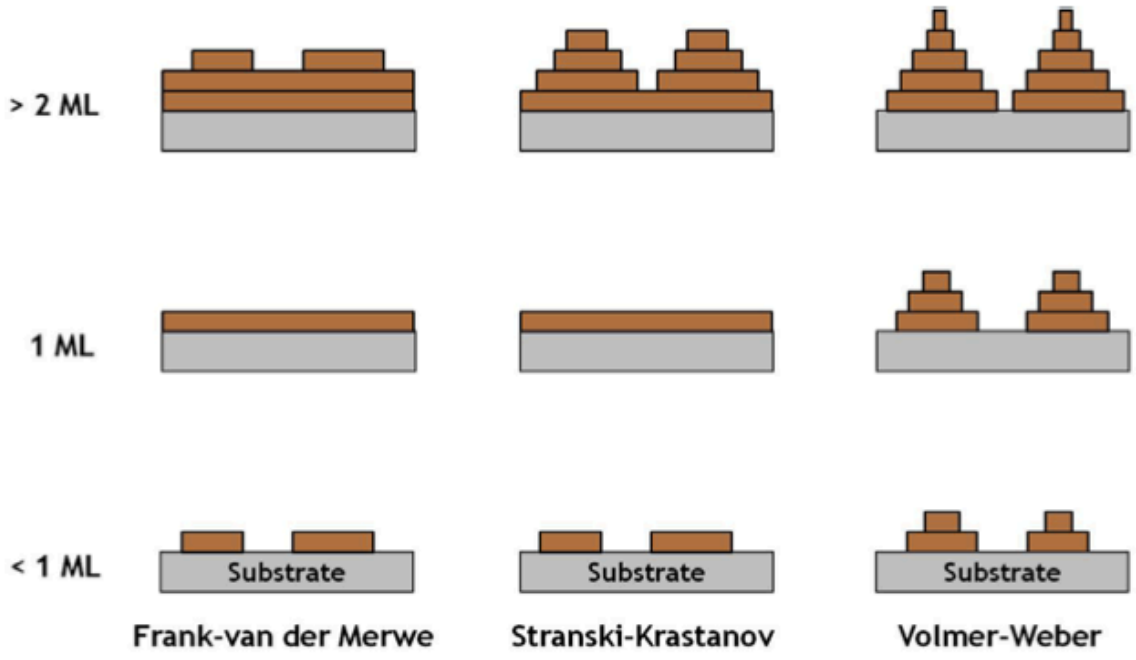

Figure 1.5: Schematic representation of three common thin film growth modes.

1.3 Thin film growth

In this work, the thin film growth of organic semiconductors has been investigated on various surfaces, including SiO_2, SiO_2 modified with SAMs, and thin films of other organic semiconductors. This has been done with the goal of better understanding how the chemical and physical nature of the substrate affects thin film growth processes and interface formation. The theoretical and experimental background of thin film growth is very rich, especially for simpler growth systems such as metal on metal or semiconductors **[27-29]**. This section provides a brief summary of thin film growth phenomena that pertain to organic thin film systems, common film growth modes, and sub-monolayer nucleation theory.

There are three common growth modes **[28]** that describe thin film morphology. These are described in Figure 1.5, showing film morphologies at coverages of less than one, one, and greater than two monolayers (MLs). Frank-van der Merwe growth comprises one extreme, where the film growths perfectly in a layer-by-layer (LbL) manner. Each monolayer fills completely before the next monolayer nucleates. The other extreme is described by the Volmer-Weber mode, where the film grows in a perfect island or three-dimensional mode (3D). The intermediate case is the Stranski-Krastanov mode, where growth is initially layer-by-layer, but transitions to 3D growth after a critical film thickness. This is sometimes described as layer-plus-island growth.

It should be noted that the aforementioned growth modes were initially predicted based on surface energy arguments described by capillary theory **[30]**:

$$\gamma_{film} + \gamma_{interface} \leq \gamma_{substrate} \tag{1.1}$$

Where γ_{film} is the surface energy of the film/vacuum interface, $\gamma_{substrate}$ is the surface energy of the substrate/vacuum interface and $\gamma_{interface}$ is the surface energy of the substrate/film interface. If this relationship holds for a growth system, then Frank-van der Merwe or LbL growth is favored. If it does not hold, then Volmer-Weber or island growth is favored. In Stranski-Krastanov growth, Equation 1.1 holds for an initially strained monolayer, after which the film switches to island growth mode as the increase in strain contributes to the increasing interface energy.

Arguments based on surface energy are based on thermodynamic equilibrium. However, thin film growth is not an equilibrium process. Instead, kinetic processes are responsible for the final observed thin film morphology. These processes are shown schematically in Figure 1.6. The first process is adsorption

as shown in Figure 1.6(a), where the kinetic energy of the incident molecule must be dissipated in order for it to become trapped onto the surface. The supersonic molecular beam deposition experiments reported in this work feature incident molecules of high kinetic energy. In order to trap onto the surface, this energy must be dissipated. This process of adsorption will have an associated sticking coefficient (S_A), and this may vary depending on the physical and chemical nature of the substrate, and whether the molecule is incident on the bare substrate ($S_{A,0}$) or the existing film ($S_{A,1}$). Molecules deposited via thermal evaporation are incident on the surface with much less kinetic energy to dissipate, and so can be assumed to have a sticking coefficient of unity.

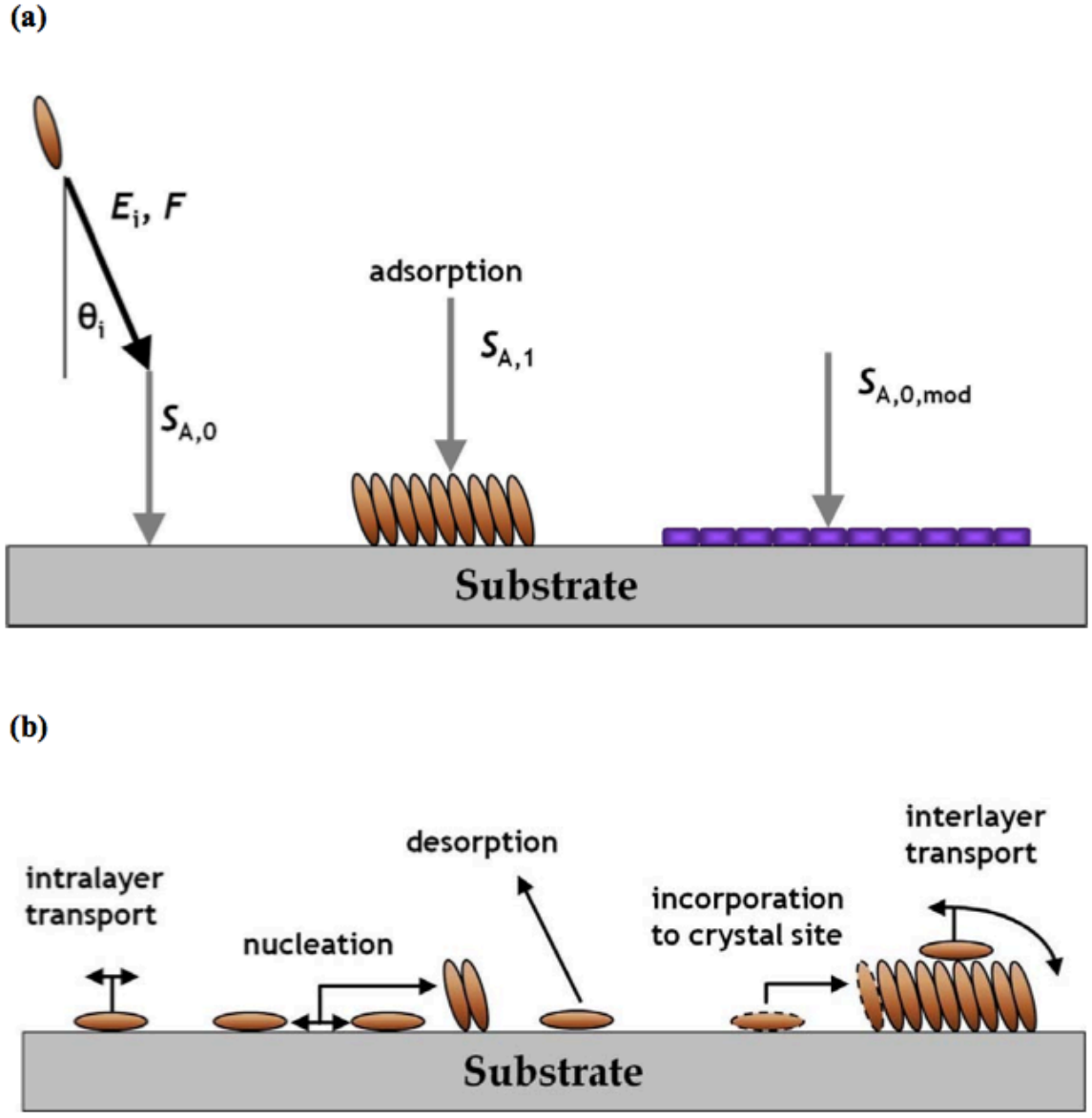

Figure 1.6: (a) Schematic representation of the process of adsoprtion of an incident molecule from the gas phase onto a solid surface. The probability of adsorption may change depending on the nature of the surface. (b) Schematic representation of the kinetic process that may happen on a solid surface during organic film growth.

Once adsorbed onto the surface, the molecules may undergo several kinetic processes, as showin in Figure 1.6(b), each with its own activation barrier. Firstly, molecules will diffuse around on the surface (intralayer transport). When a sufficient number of these molecules meet, they will nucleate islands. If the island is larger than a stable size, it will continue to grow larger. Islands less than a stable size will decrease in size and decay. Once the average island-island separation is smaller than the diffusion length of the adsorbed molecule, molecules are more likely to incorporate into existing islands than nucleate new ones. Admolecule diffusion around island edges may have different characteristics than diffusion of isolated admolecules. As the islands continue to grow, they will eventually coalesce with other islands, and after coalescence the next monolayer will begin to grow. These kinetic processes will dictate thin film morphology as new islands nucleate on existing islands rather than the substrate. The process of interlayer transport will determine how the film will roughen over time. A mechanism of interlayer transport is for an admolecule to diffuse to a step edge of an island and hop over to the layer below. This requires the admolecule to overcome an additional energetic barrier known as the Ehrlich-Schwoebel (ES) barrier **[31-35]**.

These kinetic processes illustrated in Figure 1.6 can be connected to the film growth modes shown in Figure 1.5. An organic thin film system may illustrates perfect LbL growth when there exists infinite interlayer transport. If interlayer transport is prevented, when the ES barrier is too high, then 3D growth is observed. If the probability of interlayer transport decreases with increasing film coverage, the result is layer-plus-island growth. In this work, several studies are described which quantify how the submonolayer island density of organic thin films changed as a function of thin film growth rate and the chemical na-

ture of the substrate. Such measurements allow the determination of the kinetic parameters of molecular motion on the surface. The submonolayer thin film island density (N_{max}) for 2D islands, complete condensation and homogenous nucleation before island coalescence has occurred can be described using Venables nucleation theory **[27,28,36]**:

$$N_{max} = \eta(\theta, i^*)(GR/D)^{i^*/(i^*+2)} \exp[E_{i^*}/(i^* + 2)k_B T_s] \tag{1.2}$$

where GR is the film growth rate, D is the tracer diffusivity of the molecule, i^* is the critical cluster size, E_{i^*} is the binding energy of the critical cluster, T_s is the substrate temperature and k_B is the Boltzmann constant. The critical cluster is defined as the largest unstable cluster, such that clusters of $i^* + 1$ molecules are more likely to grow than decay. The dimensionless prefactor $\eta(\theta, i^*)$ is nearly a constant which is only weakly dependent on i^* and film coverage, θ **[28]**. The complete condensation assumption implies irreversible adsorption, or negligible desorption. This is valid for experiments carried out at low substrate temperatures. Homogenous nucleation implies that island density is not driven by surface defects. Equation 1.2 shows that the critical cluster size may be obtained by measuring how the maximum island density, N_{max}, varies with GR **[27-39,36]**. It is important to note that the above relationship was derived from rate equations describing monomer and cluster densities on a surface **[36]**. One can refer to literature **[28]** regarding predicted island density relationships for other film growth regimes.

1.4 Molecular beam techniques

This section will discuss the two types of molecular beams used to deposit organic semiconductors of interest: effusive molecular beams and supersonic molecular beams. Supersonic molecular beams are a powerful probe of molecule-surface interactions, and allow for control of the kinetic energy of organic molecules over a range of energies on the order of or greater than the strength of intermolecular and molecule-surface interactions. In this work, several studies are presented of the adsorption dynamics of organic semiconductors both as a function of kinetic energy and of surface composition. This section will also briefly discuss different types of non-reactive absorption and scattering events than may occur. The following sections have been adapted from references **[37,38]**.

1.4.1 Characterization of molecular beams

A molecular beam is a stream of electrically neutral molecules produced by expanding a gas through an orifice into a region of low pressure and collimating the flow by several apertures along the beam line. Based on the type of source, molecular beams can be broadly classified as effusive or supersonic. These can be differentiated by the Knudsen number, Kn, defined as the ratio of the molecular mean free path (λ) of the gas to a characteristic length scale of the source, in this case the diameter of the orifice, d:

$$Kn = \frac{\lambda}{d} \tag{1.3}$$

This number determines the extent of intermolecular interactions in a gas

expanding through a given orifice. For $Kn \gg 1$, molecules must travel long distances without undergoing collisions with each other. Molecule-wall collisions are much more frequent and transport is molecular. This is typical for an effusive beam. If $Kn \ll 1$, the molecules will undergo several collisions with each other and transport is continuum, as is the case for supersonic expansion.

Effusive beams

An effusive beam has low source pressure, which ensures free molecular flow through the orifice. Due to the small number of interactions between molecules, they are characterized by a Maxwell-Boltzmann velocity distribution, which depends on the source temperature, T_n. The flux-weighted velocity distribution, $I(v)$, is a function of temperature and is given by:

$$I = \frac{2}{\alpha^4} v^3 e^{-v^2/\alpha^2} \tag{1.4}$$

where $\alpha^2 = 2k_B T_n/m$, k_B is the Boltzmann constant, and m is the molecular weight. From this expression, the average translational energy, $\langle E_i \rangle$ can be calculated by integrating the individual molecular kinetic energies over the flux-weighted velocity distribution. This gives the result $\langle E_i \rangle = 2k_B T_n$, which demonstrates the low energy of effusive beams. Given a nozzle temperature, T_n, of 500 C, the average energy, $\langle E_i \rangle$, is 0.133 eV. The flux distribution from an effusive beam, F_i, can be expressed via Boltzmann statistics, or a cosine angular distribution:

$$F_i = \frac{P_n}{\sqrt{2\pi m k_b T_n}} \frac{\pi d_n^2}{4\pi x^2} \cos\theta \tag{1.5}$$

where P_n and d_n are the source pressure and nozzle diameter respectively, and x is the distance from the source to the substrate.

Effusive beams have the advantage of being simple to produce and characterize. This comes at the cost of wide beam energy distributions, limited range of kinetic energies, and difficulty in producing high beam to background intensity. Effusive beams are effective for large-area dosing of surfaces.

Supersonic molecular beams

Supersonic beams are formed via an adiabatic expansion of a gas from a nozzle at high pressure into a vacuum of low pressure. It is this large pressure difference which drives the acceleration of the molecules to supersonic speeds. For supersonic beams, $Kn \ll 1$, so intermolecular collisions occur much more frequently than collisions with the wall. Thus, random, thermal molecular motion is converted into translational motion. Due to the continuum nature of the source, supersonic beams produce nearly monoenergetic beams. A schematic representation comparing effusive and supersonic beams is displayed in Figure 1.7.

The supersonic beam is more focused and intense and has a strongly peaked flux distribution. The energy of the molecules in the supersonic beam can be further enhanced by a seeding technique, where an inert, fast moving, light gas such as hydrogen or helium accelerates slow moving, heavier molecules. The energy of the molecules in a supersonic beam can be tuned to a much wider range. The flux weighted velocity distribution of a supersonic molecular beam is given by:

$$I(v) = N(c, \alpha) v^3 \exp\left(-\frac{(v-c)^2}{\alpha^2}\right) \tag{1.6}$$

where $N(c, \alpha)$ is a normalization constant and c is the most probable velocity,

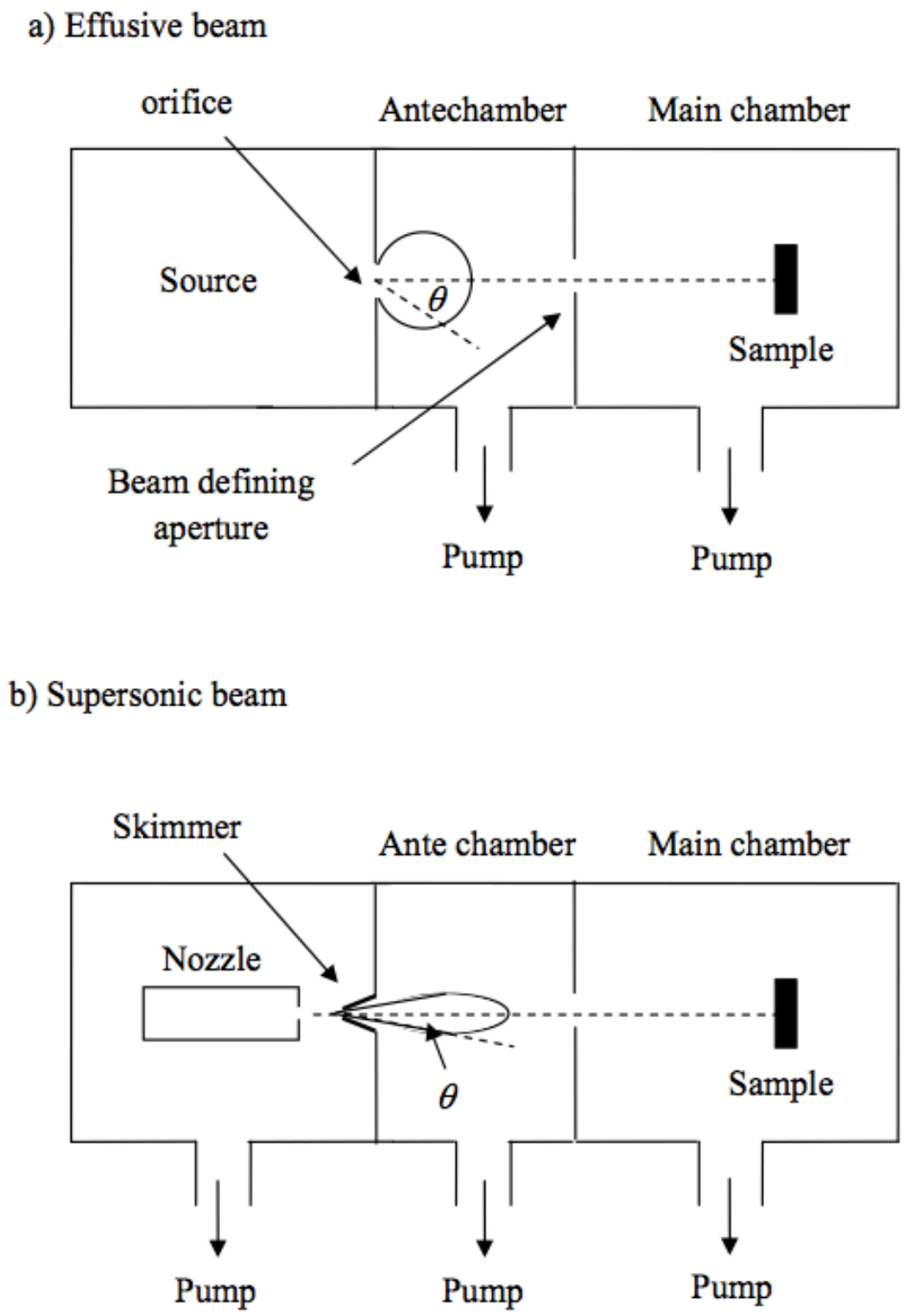

Figure 1.7: Diagram depicting (a)effusive and (b) supersonic molecular beam systems. The closed curves downstream of the orifice and skimmer represent the relative intensity distributions (reproduced from **[39]**).

defined as:

$$c = \sqrt{\frac{2\gamma k_B T_n}{(\gamma - 1)m}} \tag{1.7}$$

where $\gamma = C_p/C_v$ is the ratio of heat capacities, T_n is the nozzle temperature, and α^2 is a measure of spread in the velocities of the gas parallel to the flow direction defined as $2k_B T_{ax}/m$, where T_{ax} is the axial translational temperature, and m is the mass of the gas. Equation 1.6 reduces to the effusive beam Maxwell-Boltzmann distribution when $c = 0$ and $\alpha^2 = 2k_B T_n/m$. The resultant beam has a centerline flux 2-3 times higher than the effusive beam, and the angular distribution is peaked with a $\cos^4\theta$ distribution for a pure gas under ideal conditions.

Molecules begin at thermal energy in the high pressure region upstream of the nozzle. This is referred to as the stagnation state (pressure P_0, temperature T_0). The pressure difference imposed by a vacuum downstream of the nozzle (background pressure, P_b) accelerates these molecules to sonic speeds, given as $s = \sqrt{\gamma k_B T_n/m}$ provided P_0/P_b exceeds a critical value:

$$\frac{P_0}{P_b} \geq \left(\frac{\gamma + 1}{2}\right)^{\frac{\gamma}{(\gamma-1)}} \tag{1.8}$$

which is less than 2.1 for all gases. The Mach number, M, is defined as the ratio of gas velocity to the speed of sound. In order for the expansion to be supersonic, the pressure ratio must be higher than this critical value to ensure $M > 1$. If this is not the case, the gas molecules will exit the nozzle at subsonic velocity and undergo no further acceleration.

In a seeded supersonic molecular beam, all molecules in the mixture are accelerated to the same velocity, rather than the same energy. This allows for the enhancement of kinetic energy of a heavier molecule in a dilute mixture with light molecules. In such a mixture, the maximum possible translational energy

of a reactant is given by:

$$\langle E_i \rangle = \frac{m_i}{\langle m \rangle} \langle C_p \rangle T_n \tag{1.9}$$

where m_i is the mass of the reactant gas, $\langle m \rangle$ is the mole fraction mean mass of the gas mixture, $\langle C_p \rangle$ the mole fraction mean heat capacity of the mixture, and T_n is the nozzle temperature. Typically, the expansion is not ideal and both velocity and temperature will deviate from ideal values. This non-ideality is termed velocity and temperature slip. In both cases, it results in an energy lower than that expected from Equation 1.9.

In practice, the extraction of a supersonic beam requires a skimmer placed a short distance downstream of the nozzle, as shown in Figure 1.7. An illustration of the expansion region right after the nozzle is given in Figure 1.8. Molecules traveling beyond the expansion achieve velocities in excess of the speed of sound. They are not able to adjust to the boundary conditions downstream of the expansion because information in a fluid propagates at the speed of sound.

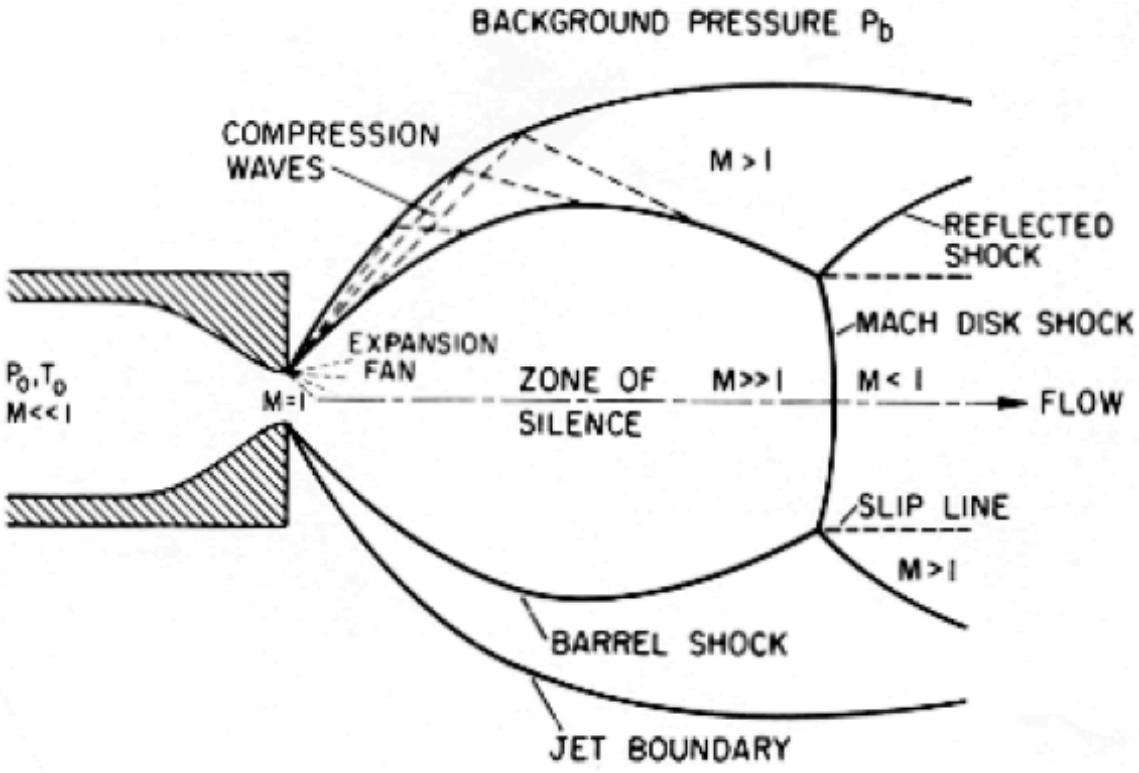

Figure 1.8: Diagram depicting a gas undergoing supersonic expansion. Commonly referred to as a "free jet" expansion, it is produced without andy downstream structures affecting the boundary conditions of the expansion (reproduced from **[37]**).

The skimmer is conical or trumpet shaped with a small aperture at the apex used to extract molecules from the zone of silence. This shape minimizes backscattering of molecules into the free jet stream out of the nozzle. After extraction from the skimmer, the molecules of the beam travel into a separate chamber, usually called the ante-chamber, where further pumping maximizes the beam to background ratio. Additionally, further modulation of the beam can be carrier out in the ante-chamber using a fast rotating blade chopper or slow linear beam flag. Finally, the beam passes through an aperture into the main chamber and impinges on the substrate. The spot of the beam on the substrate is defined by this aperture.

1.4.2 Supersonic molecular beam scattering

This section on supersonic molecular beam scattering has been adapted from references **[38,40]**. Supersonic molecular beams have been used extensively to study the dynamics of adsorption between a gaseous molecule and the surface. These interactions can be broadly classified as reactive or non-reactive scattering. This is dependent on whether a chemical reaction takes place at the surface. The nature of the substrate and the kinetic energy and state of the incident molecule determine the outcome of the scattering event. This section will briefly discuss different types of non-reactive scattering events.

Elastic scattering

During an elastic scattering event, the incident molecule is reflected from the surface with an extremely narrow angular distribution peaked at the specular

angle. No energy transfer takes place during an elastic scattering event. This is characteristic of beams composed of light atoms (e.g. H_2 or He). As this is a simple, physical process, the angular distribution of the scattered beam can be correlated to surface topology. Usually this is a single collision process, resulting in surface residence times below 10^{-12} sec **[41]**.

Inelastic scattering

For the case of inelastic scattering, incident molecules lose translational energy after single or multiple collisions with the substrate. Incident translational energy is either converted to internal energy or dissipated by the generation of surface phonons. Scattered molecules still retain memory of their incident trajectories. Compared to elastic scattering, inelastically scattered molecules will exhibit a wider energy and angular distribution. Surface residence times depend on the number of collisions with the surface. This mechanism is typical when the incident molecule is of similar mass compared to surface atoms.

Adsorption (trapping) and desorption

Due to an attractive interaction between a molecule and the surface, an incident molecule can be trapped from the vapor phase. This attraction may be due to van der Waals interactions (which is the case for physical adsorption, or physisorption). Adsorption is the first step to film growth. If the incident molecule forms a chemical bond with the surface, this interaction is much stronger and is called chemisorption. During the deposition of organic semiconductors described in this work, the molecules are physisorbed onto the surface. No chem-

ical bond is formed.

When an incident hyperthemal molecule falls into the potential energy well, the kinetic energy in the direction normal to the surface increases. If this energy is not transferred to some other degree of freedom, the molecule will bounce off the surface and adsorption will not take place. When adsorption does take place, this excess energy is typically transferred to surface phonons. Classically, a molecule with incident energy E_i will have an energy of $E_i + U_d$ inside the attractive well, where U_d is the well depth. On colliding with the surface, the molecule will lose some fraction f, of this total energy. If the remaining energy, $(1f)(E_i + U_d)$, is less than U_d, then the molecule will be trapped in the well and adsorb on the surface. Otherwise it will be scattered off. Based on this, one would expect the adsorption probability to decrease with increasing kinetic energy. This process is called trapping-mediated adsorption.

Molecules on the surface can undergo desorption. Since these molecules have reached thermal equilibrium with the surface, desorbed molecules will exhibit Maxwell-Boltzmann velocity distributions characterized by the substrate temperature. Additionally their angular distribution is symmetric, peaked about the surface normal. For the molecules studied in this work, desorption does not play a role at the low substrate temperatures used.

1.5 References

1. Bao, Z.; Locklin, J., Eds, *Organic Field Effect Transistors*, Taylor and Francis Group, LLC, **2007**.
2. Ling, M. M.; Bao, Z. N. *Chem. Mater.* **2004**, *16*, 4824-4840.

3. Briseno, A. L.; Mannsfeld, S. C. B.; Reese, C.; Hancock, J. M.; Xiong, Y.; Jenekhe, S. A.; Bao, Z.; Xia, Y. *Nano Lett.* **2007**, *7*, 2847-2853.

4. Li, W.; Song, Q.; Sun, X.; Wang, W.; Ding, X.; Hou, X., Sci. China, **2009**, *53*, 288-300.

5. Ruiz, R.; Papadimitratos, A.; Mayer, A. C.; Malliaras, G. G. *Adv. Mater.* **2005**, *17*, 1795-1798.

6. Dinelli, F.; Murgia, M.; Levy, P.; Cavallini, M.; Biscarini, F.; de Leeuw Dago M. *Phys. Rev. Lett.* **2004**, *92*, 116802-116804.

7. Muck, T.; Wagner, V.; Bass, U.; Leufgen, M.; Geurts, J.; Molenkamp, L. W. *Synthetic Metals* **2004**, *146*, 317-320.

8. Dodabalapur, A.; Torsi, L.; Katz, H. E. *Science* **1995**, *268*, 270-271.

9. Kelley, T. W.; Boardman, L. D.; Dunbar, T. D.; Muyres, D. V.; Pellerite, M. J.; Smith, T. P. *J. Phys. Chem. B* **2003**, *107*, 5877-5881.

10. Yang, H.; Shin, T. J.; Ling, M. M.; Cho, K.; Ryu, C. Y.; Bao, Z. *J. Am. Chem. Soc.* **2005**, *127*, 11542-11543.

11. Virkar, A.; Mannsfield, S.; Oh, J. H.; Toney, M. F.; Tan, Y. H.; Liu, G.; Scott, J. C.; Miller, R.; Bao, Z. *Adv. Funct. Mater.* **2009**, *19*, 1962-1970.

12. Shtein, M.; Mapel, J.; Benziger, J. B.; Forrest, S. R. *Appl. Phys. Lett.* **2002**, *81*, 268-270.

13. Klauk, H.; Halik, M.; Zschieschang, U.; Schmid, G.; Radlik, W.; Weber, W. *J. Appl. Phys.* **2002**, *92*, 5259-5263.

14. Kelly, T. W.; Boardman, L.D.; Dunbar, T. D.; Muyres, D. V.; Pellerite, M. J.; Smith, T. P. *J. Phys. Chem. B* **2003**, *107*, 5877-5881.

15. Duerr, A. C.; Schreiber, F; Muench, M.;Karl, N.;Krause, B.; Kruppa, V.; Dosch, H. *Appl. Phys. Lett.*, textbf2002, *81*, 2276.

16. Chesterfield, R. J.; McKeen, J. C.; Newman, C. R.; Frisbie, C. D.; Ewbank, P. C.; Mann, K. R.; Miller, L. L. *J. Appl. Phys.*, **2004**, *95*, 6396-6405.

17. Chesterfield, R. J.; McKeen, J. C.; Newman, C. R.; Ewbank, P. C.; da Silva Filho, D. A.; Bredas, J-L.; Miller, L. L.; Mann, K. R.; Frisbie, C. D., *J. Phys. Chem. B.*, **2004**, *108*, 19281.

18. Malenfant, P. R. L.; Dimitrakopoulos, C. D.; Gelorme, J. D.; Kosbar, L. L.; Graham, T. O.; Curioni, A.; Andreoni, W. *Appl. Phys Lett.*, **2002**, *80*, 2763.

19. Mattheus, C. C.; Dros, A. B.; Baas, J.; Oostergetel, G. T.; Meetsma, A.; de Boer, J. L.; Palstra, T. M. *Synth. Met.* **2003**, *138*, 475.

20. Ruiz, R.; Mayer, A. C.; Malliaras, G. G.; Nickel, B.; Scholes, G.; Kazimirov, A.; Kim, H.; Headrick, R. L.; Islam, Z. *Appl. Phys. Lett.* **2004**, *85*, 4926-4928.

21. Heinrich, M. A.; Pflaum, J.; Tripathi, A. K.; Frey, W.; Steigerwald, M. L.; Siegrist, T. *J. Phys. Chem. C* **2007**, *111*, 18878.

22. Duerr, A. C.; Koch, N.; Kelsch, M.; Ruehm, A.; Ghijsen, J.; Johnson, R. L.; Pireaux, J. J.; Schwartz, J.; Schreiber, F.; Dosch, H.; Kahn, A. *Phys. Rev. B* **2003**, *68*, 115428/1-115428/12.

23. Petit, M.; Hayakawa, R.; Wakayama, Y.; Chikyow, T. *J. Phys. Chem. C* **2007**, *111*, 12747-12751.

24. Krauss, T. N.; Barrena, E.; Zhang, X. N.; de Oteyza, D. G.; Major, J.; Dehm, V.; Wuerthner, F.; Cavalcanti, L. P.; Dosch, H. *Langmuir* **2008**, *24*, 12742-12744.

25. Tatemichi, S.; Ichikawa, M.; Koyama, T.; Taniguchi, Y. *Appl. Phys. Lett.* **2006**, *89*, 112108/1-112108/3.

26. F. Schreiber, *Prog. Surf. Sci.* **2000**, *65*, 151.

27. Zhang, Z.; Lagally, M. G. *Science* **1997**, *276*, 377-383.

28. Venables, J. A.; Spiller, G. D. T.; Hanbcken, M. *Rep. Prog. Phys.* **1984**, *47*, 399-459.

29. Brune, H. *Surf. Sci. Rep.* **1998**, *31*, 121-229.

30. Ohring, M. *The Materials Science of Thin Films* (Academic Press, London, UK, **1992**).

31. Ehrlich, G.; Hudda, F. G. *J. Chem. Phys.* **1966**, *44*, 1039-1049.

32. Schwoebel, R. L.; Shipsey, E. J. *J. Appl. Phys.* **1966**, *37*, 3682-3686.

33. Fendrich, M.; Krug *J. Phys. Rev. B* **2007**, *76*, 121302/1-121302/3.

34. Hlawacek, G.; Puschnig P.; Frank, P.; Winkler, A.; Ambrosch-Draxl, C.; Teichert, C. *Science* **2008**, *321*, 108-111.

35. Goose, J. E.; First, E. L.; Clancy, P. *Phys. Rev. B* **2010**, *81*, 205310/1-205310/20.

36. Venables, J. A. *Phys. Rev. B* **1987**, *36*, 4153-4162.

37. Scoles, G. *Atomic and Molecular Beam Methods* (Oxford University Press, Oxford, UK, **1998**).

38. Arumainayagam, C. R.; Madix, R. J. *Prog. Surf. Sci.* **1991**, *38*, 1-102.

39. Anderson, J. B. *Molecular Beams and Low Density Gas Dynamics*, edited by P. P. Wegener (Marcel Dekker, New York, USA, **1974**).

40. Barker, J. A.; Auerbach, D. J. *Surf. Sci. Rep.* **1984**, *4*, 1-100.

41. Rettner, C. T.; Ashfold, R. *Dynamics of Gas-Surface Interactions* (The Royal Society of Chemistry, Cambridge, UK, **1991**).

CHAPTER 2

EXPERIMENTAL PROCEDURES

In this section, we describe the ultra-high vacuum (UHV) system used at the G3 station of the Cornell High Energy Synchrotron Source (CHESS) to study the real time growth of thin films of organic semiconductors via *in situ* x-ray scattering. A description is given of both the supersonic molecular beam source and the effusive source. An outline is given of the general procedure of preparing the system for a real time x-ray experiment. Time-of-flight (TOF) experiments used to characterize the supersonic molecular beam are explained. The process of preparing samples, both SiO_2 and SiO_2 modified with self-assembled monolayers (SAMs), is described. Techniques of characterizing deposited thin films such as atomic force microscopy (AFM), contact angle goniometry, and x-ray scattering are discussed.

2.1 Description of G-Line UHV chamber

Experiments described in this work were carried out in a custom designed, multiple stage, stainless steel ultra-high vacuum (UHV) chamber that is depicted schematically in Figures 2.1 and 2.2. The main deposition chamber (volume 18 L) is pumped by a 500 L-s^{-1} turbomolecular pump (Pfeiffer TMU 521P) and achieves base pressures of 2×10^{-9} Torr after a 48 hour bakeout at 140 °C. This bakeout is performed by wrapping heating tape around the exterior of the chamber, and covering it with aluminum foil. A bakeout oven was originally designed for this chamber, but is not used due to difficulties fitting it around the chamber in the cramped space of the G3 hutch at CHESS.

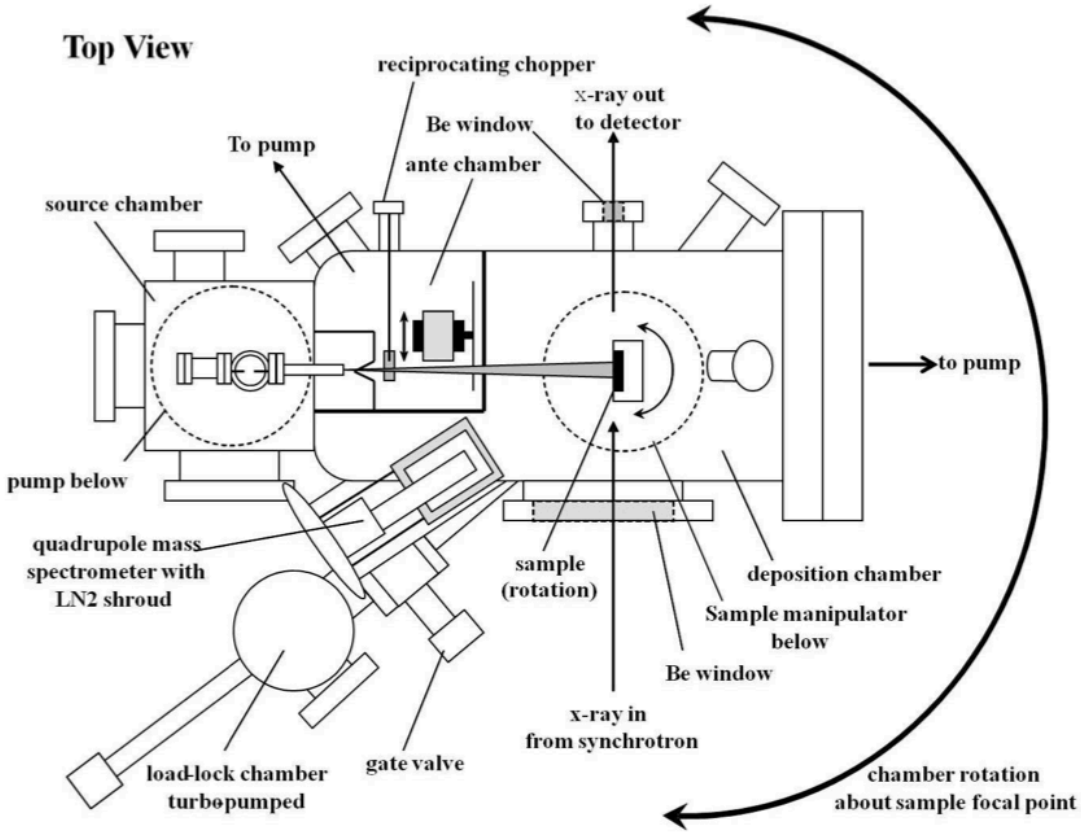

Figure 2.1: Top view schematic of the G-Line UHV chamber.

A sample manipulator (Thermionics 940619NW) is positioned in the center of the main chamber and can accommodate samples up to about 1.2 in. x 1.2 in. in size. Typical substrates are roughly 1.2 in. tall by 0.3 in. wide. A narrow sample is desirable, as the flux of molecules to the surface is not uniform across the width of the sample. Using a narrow sample minimizes this effect. The sample can be heated by applying current to a radiant graphite heater encapsulated in pyrolytic boron, which is capable of heating Si samples to temperatures in excess of 400 °C. Samples can also be cooled by flowing liquid nitrogen through a copper braid (CLNI-1 retrofit indirect cooling). A drawing of the sample manipulator is shown in Figure 2.3. The sample temperature can be measured by

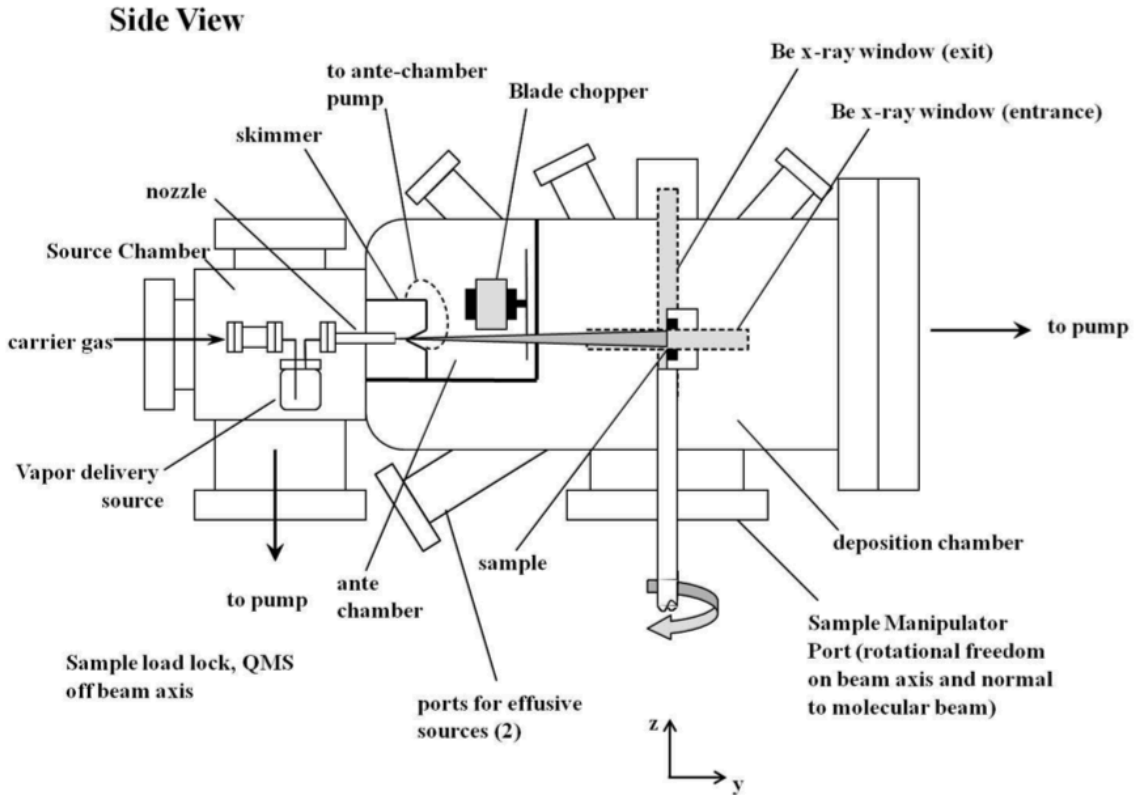

Figure 2.2: Side view schematic of the G-Line UHV chamber.

a reference thermocouple attached to the heater, or the sample thermocouple on the Mo sample platen itself (Thermionics QN104143), both type K. After being mounted on the sample platen, the sample is transferred to the chamber via a load-lock chamber. This load-lock chamber is pumped by a 60 L-s^{-1} turbomolecular pump (Pfeiffer TMU 071 P) and can reach pressures below 5 x 10^{-8} Torr after several hours. Typically, the load-lock is pumped down to 10^{-7} Torr before transferring the sample to the main chamber. This usually requires about 20 minutes of pumping.

On either side of the sample manipulator are two rectangular Be windows. The first window is oriented horizontally, allowing the x-ray beam to enter the

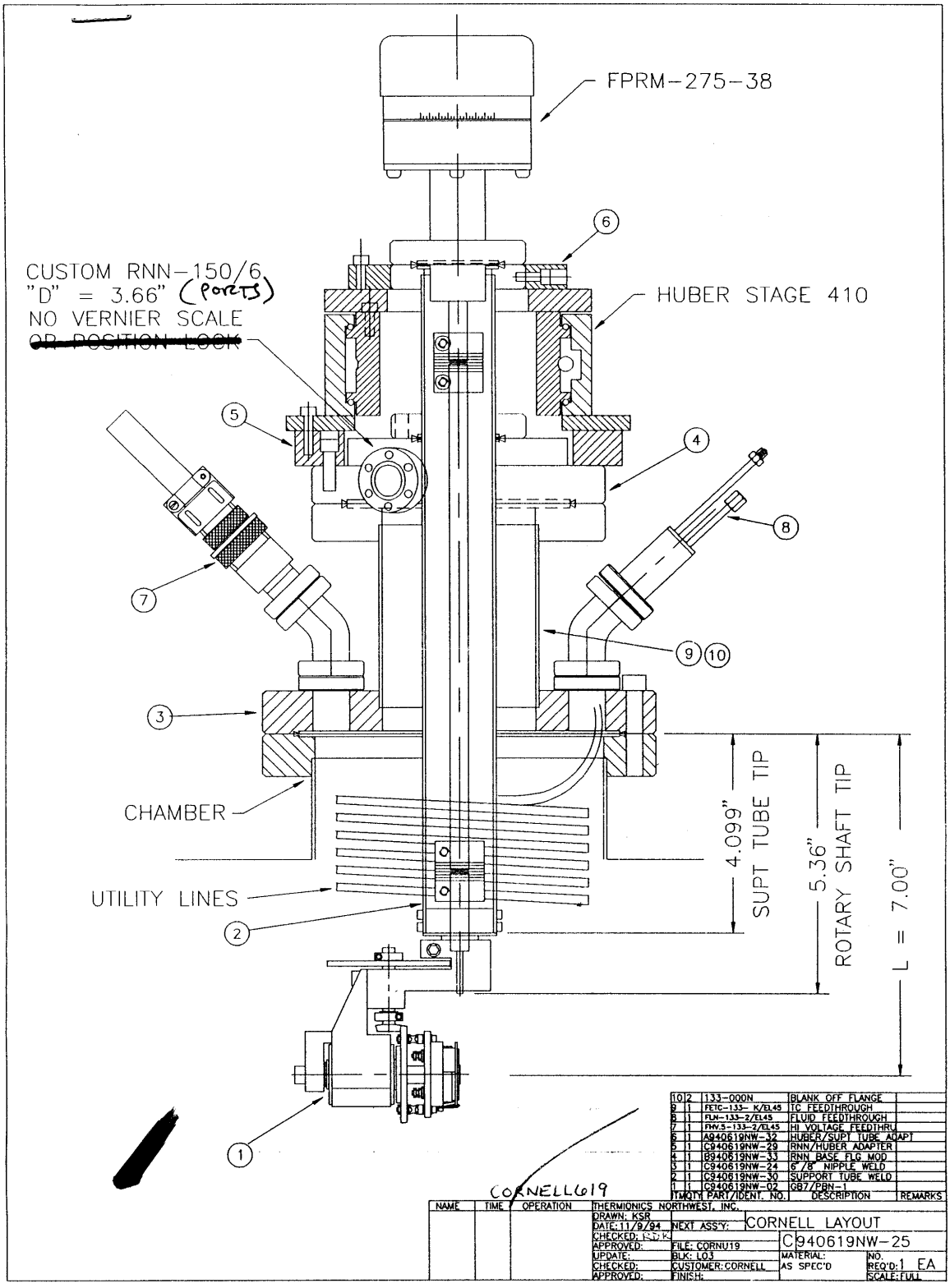

Figure 2.3: Drawing of the sample manipulator, provided by Thermionics.

chamber from a range of angles relative to the surface normal. After scattering from the sample, the x-rays exit the chamber through a second Be window, oriented vertically. After exiting the chamber, the scattered x-rays pass through a set of two slits into a silicon avalanche photodiode detector (APD, Oxford Danfysik, Oxford, UK).

The chamber itself is mounted on a diffractometer table. This allows for precise control of the UHV chamber with respect to the incident synchrotron x-ray beam. The table can be translated along three axes, and rotated around an axis parallel to the sample manipulator. The sample manipulator can also be rotated in the plane defined by the incident x-ray beam, as well as about the surface normal. This allows for a number of x-ray scans to be performed, e.g. specular reflectivity and grazing incidence diffraction. Monitoring the scattered x-ray intensity during film growth at the so-called anti-Bragg position allows for investigation of film growth dynamics. After depositing films, specular reflectivity and grazing incidence diffraction allow for the determination of crystallographic information both normal and parallel to the substrate.

A quadrupole mass spectrometer (QMS, model: Extrel 5221) may be mounted within the deposition chamber. For characterization of supersonic molecular beams using time-of-flight (TOF) methods, the QMS is mounted on a linear translator in the direct beam position, such that the molecular beam is in line with the axis of the QMS. The QMS can also be mounted on other flanges to allow for indirect scattering experiments.

Due to the low vapor pressure of the organic molecules studied in this work, an *in vacuo* container (bubbler, see Figure 2.4) has been designed and employed to generate supersonic molecular beams in the source chamber. The bubbler is

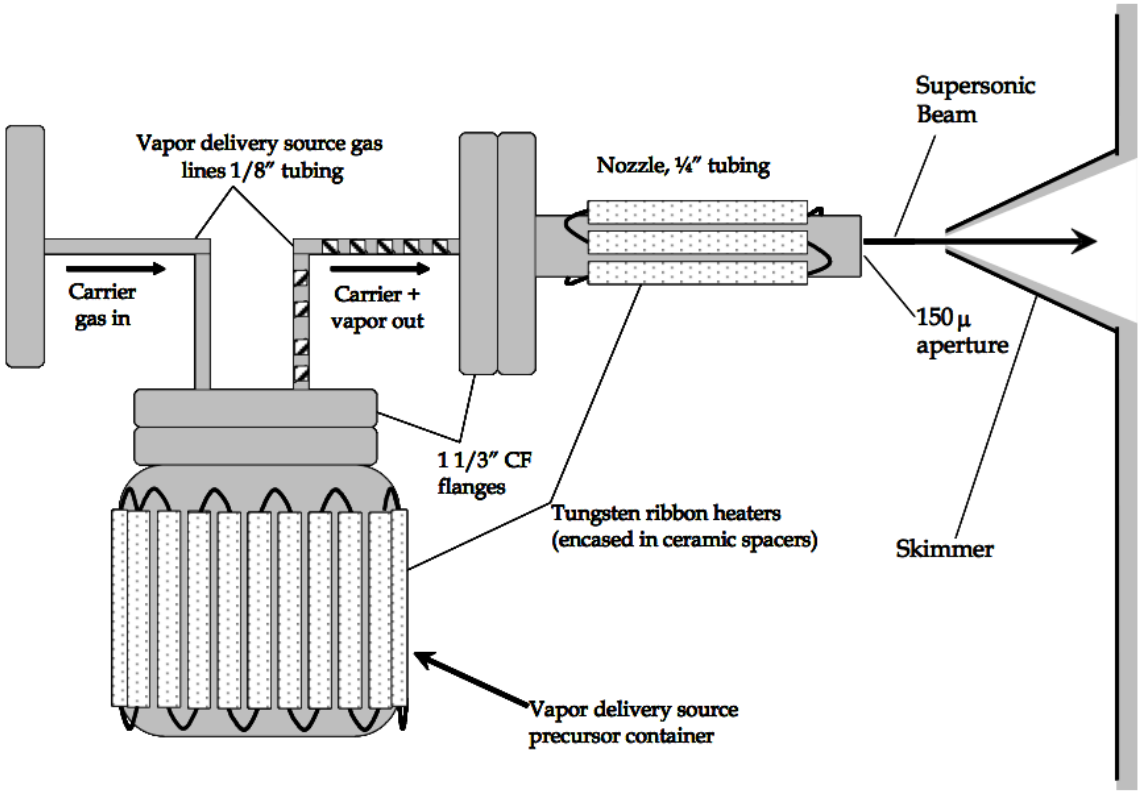

Figure 2.4: Schematic representation of bubbler, nozzle and tube assembly. The skimmer is also shown.

connected directly to the gas delivery line and a heated nozzle via 1/8″ tubing a 1-1/3″ CF flanges. Helium carrier gas is used to generate the supersonic expansion of the organic species studied in this work. He gas is fed to the system using a mass flow controller (MKS 1179) and stagnation pressures are measured using a capacitance manometer upstream of the chamber. This pressure can vary from 28 to 250 Torr depending on the He flow rate and nozzle temperature. The nozzle is a 150 μm aperture in a 125 μm stainless steel plate that is welded to the end of an electropolished 1/4″ stainless steel tube. The nozzle, and the bubbler are heated by tungsten ribbon heaters encased in 1/8″ (ID) ceramic tubing, and affixed using copper wire. The section of tube between the bubbler and the nozzle is heated by wrapping the tube in tungsten ribbon encased in fiber-

glass insulation. This is then held in place with copper wire. This prevents the organic molecules in the vapor phase from condensing on the walls of the tube and causing a clog. Helium is fed into the bubbler and is mixed with the organic vapor species using a baffle within the bubbler, before exiting through a 1/8" tube to enter the nozzle. The entire nozzle/bubbler assembly is mounted on a precision x-y-z manipulator. The temperature of the nozzle (T_N), bubbler (T_B), and the tube section between them (T_T) are monitored by type K thermocouples spot welded to their surfaces. The gas mixture is expanded into a source chamber, which is pumped using a 520 L-s^{-1} corrosion resistant turbomolecular pump (Pfeiffer TMU 520C). The gas then passes through a trumpet-shaped, Ni skimmer (1.5mm in diameter) mounted on a stainless steel plate into the antechamber. The vapor delivery source, nozzle and skimmer assembly are shown schematically in Figure 2.4. Refer to reference **[1]** regarding optimization of supersonic molecular beams when changing the following: diameter of nozzle, nozzle skimmer distance, diameter of the aperture at the apex of the skimmer, location of skimmer and geometry of the skimmer.

After passing through the skimmer and into the antechamber, the beam is differentially pumped before passing through an aperture into the main chamber. The aperture is mounted on a quarter plate which separates the antechamber from the main chamber. The antechamber is pumped by a 70 L-s^{-1} turbomolecular pump (Pfeiffer TMU 071 P) and condensable materials can be further pumped by a liquid nitrogen reservoir within the antechamber. However, given the extremely low vapor pressure of the organic materials studied in this work, this is not typically necessary. A reciprocating beam flag is used in defining molecular beam exposure to the sample to begin and end film growth precisely. A rotating blade chopper is used to produce fast molecular beam

Molecule	T_B (°C)	T_N (°C)	He flow rate (sccm)	P_N (torr)
Pentacene	250	380	10/25/70	48/89/206
DIP	325	420	10/25/70/120	49/92/206/326
PTCDI-C_{13}	350	445	10/25/70/90	48/92/208/255
PTCDI-C_8	325	435	10/25/70/90	51/94/210/260
PTCDI-C_5	320	430	10/25/70/90	50/95/210/259

Table 2.1: Experimental conditions during supersonic molecular beam operation

waveforms (timescale < 1 ms), which can be used in coordination with the QMS and a multi-channel scalar data acquisition card (ORTEC MCS-pci) during time-of-flight experiments. Data acquisition with the MCS card is triggered by a photo-interruptor mounted on the rotating blade chopper. The total distance from the nozzle to the substrate is approximately 20.5 cm with a distance traveled within the ante chamber of 8.9 cm. The blade of the fast chopper is 9.3 cm from the sample surface. Refer to reference **[2]** for additional details of the G-Line deposition chamber, particularly for detailed system drawings.

2.2 Performing real time film growth experiments

2.2.1 Supersonic molecular beam growth

This section will describe the procedure of producing a supersonic molecular beam and using it to deposit organic thin films. Pentacene, PTCDI-C_{13}, PTCDI-C_8 and PTCDI-C_5 were all purchased from Sigma-Aldrich. DIP was purchased from Institut fuer PAH-Forschung (Contact: Dr. W. Schmidt, pah-schmidt@web.de).

Important experimental conditions such at nozzle temperature (T_N), bubbler temperature (T_B), He flowrate and nozzle pressure (P_N) values are summarized in Table 2.1. The 1/8" tube (T_T) between the evaporator and nozzle was typically heated to temperatures 10 to 15 °C below the nozzle.

Flow of the He carrier gas is controlled using an MKS mass flow controller upstream of the bubbler. The bubbler temperature is controlled using a Eurotherm (power supply model 7100A, controller model 2416), while the tube and nozzle were heated using variacs. The aperture plate used in this work defined a beam spot on the sample 4mm tall, and wide enough to span the width of the samples used. Multiple experiments (up to 4) can be carried out on the same sample by translating the substrate perpendicular to the beam. Moving the sample by 5mm between exposures results in films separated by 1mm. This is possible due to the high beam to background flux ratio. The background contribution to deposited films is negligible, as evidenced by atomic force micrographs of surface regions unexposed to the beam. Exposure of the beam to the substrate is controlled by a reciprocating shutter.

The following procedure is used to generate a supersonic molecular beam:

1. First, the pieces of the nozzle/bubbler source assembly should be thoroughly cleaned by sonication in chloroform. The skimmer should also be removed and sonicated.
2. After having cleaned the pieces, the ceramic clad tungsten ribbon should be attached to the bubbler and nozzle, and the skimmer should be reattached.
3. The bubbler should be filled with the desired organic material.

4. The pieces should be assembled together, and fiberglass clad tungsten ribbon should be wrapped around the tube section.
5. Thermocouple junctions should be spot welded. One to the end of the nozzle, one to the side of the bubbler, and one to the tube section between them.
6. Prior to mounting the flange to the source chamber, it is strongly advised to check and double check all the electrical heating and thermocouple connections.
7. Once the flange is mounted, connect the carrier gas line to the flange and pump down and bakeout the chamber.
8. Once at a reliable base pressure, turn on the mass flow controller and run carrier gas at a reasonable flow rate (e.g. 10sccm).
9. Adjust the position of the nozzle via the x and y micrometers (horizontal and vertical motion) on the XYZ stage to align the nozzle with the skimmer. Observe the pressure in the main chamber. Adjust the x and y position to maximize this pressure.
10. Turn on the variac to begin heating the nozzle. Once the nozzle temperature has risen above 80 °C, begin to heat the tube.
11. Once both the nozzle and tube temperatures have risen above 200 °C, begin heating the bubbler. At all times, it is important to maintain T_N greater than T_T, and T_T greater than T_B.
12. Once the bubbler reaches the desired temperature, films can be grown by opening the shutter
13. After depositing films, the nozzle and bubbler assembly should be cooled down gradually, again always keeping T_N above T_T above T_B.

2.2.2 Thermal effusive source film growth

An effusion cell (or thermal evaporator) was first installed into the G-Line deposition chamber on 15 September 2010. The addition of a second deposition source allows for growth of organic heterostructures *in situ* and in real time, as well as studies of the effects of incident kinetic energy (thermal vs. hyperthermal). For a detailed description of the design and installation of the effusion cell, consult reference **[3]**. The effusion cell is mounted on port 14 of the G-Line deposition chamber at a polar angle of 45° from the substrate surface normal.

In an effusive source, the flux has a cosine distribution. Due to this, in order to deposit a well-defined film of the same dimension as the supersonic beam spot, a shadow mask with a rectangular aperture was fabricated for the effusive source. This mask is mounted on a motorized linear translator installed on port 19. The position of the shadow mask can then be controlled through the SPEC software. During supersonic beam deposition, the mask is retracted out of the way of the beam. During deposition with the effusive source, the mask is moved to a position of about 61mm, producing a 4mm rectangular beam spot on the sample, overlapping with the 4mm supersonic beam spot. The beam to background ratio for the effusive source is excellent, with the shadow mask blocking material from reaching the surface.

The following procedure is used to deposit films with the effusion cell:

1. Clean the PBN crucible by sonicating in solvent. Acetone and/or isopropanol are sufficient to clean pentacene and DIP. Chloroform is required to clean PTCDI-C_n. Take care while handling the crucible, as it is fragile.
2. Fill the crucible with the desired organic material.

3. Mount the effusion cell on flange number 14.
4. Pump down and bake out the chamber to reach the desired background pressure.
5. Connect the power cables from the special high current sockets of the power control unit panel back to the effusion cell. Attach the thermocouple cable.
6. Turn on the power control unit.
7. Set the desired temperature on the 3504 Eurotherm regulator.
8. Turn the potentiometer knob to increase output voltage. Typically an output voltage of 2.0 V is more than sufficient to reach a target temperature of 100 °C.
9. After reaching the desired temperature, wait a few minutes prior to deposition so as to achieve uniform heating around the crucible.
10. Move the shadow mask into the correct position.
11. Open the shutter either manually or remotely.
12. Close shutter after desired growth time.
13. After depositing films, set the target temperature back to zero, turn the potentiometer knob down to 0 V output and turn off the power control unit.

The shutter can be controlled remotely by sending a 5V signal to the Actor/Sensor D-SUB9 connector on the back of the power control unit. To open the shutter, +5V should be applied to pin 6 and 0V to pin 9. When the shutter is open, the voltage across pin 1 and pin 9 should read 5V. When the shutter is closed, the voltage across pin 2 and pin 9 should read 5V.

2.2.3 X-ray beam alignment

In order to perform x-ray experiments, it is important to first align the x-ray beam, define the beam size with upstream slits, align the x-ray beam spot with the supersonic beam spot and with the effusive beam spot. The following will discuss in a step-by-step manner the process of aligning the x-ray beam in preparation for doing *in situ* x-ray scattering experiments.

1. The first step is to define a narrow x-ray beam by adjusting the upstream slits. Typical values for horizontal (h) and vertical (v) slits are: csh = s1v = s1h =s2v = s2h =0.5 mm, s3v = open, s3h = 1.0 mm, s4v = 1.0 mm and s4h = 2.0 mm. See Figure 2.5.
2. Create a supersonic molecular beam as described in section 2.2.1 (*vide supra*)
3. Cut and clip a piece of x-ray burn paper of similar size to a substrate onto the sample holder. Place a piece of aluminum foil behind the burn paper to ensure it is clipped securely to the sample platen.
4. Using the transfer arm, transfer the sample platen with burn paper from the load-lock to the main chamber. The burn paper outgases, so the main pressure will climb to the 10^{-6} Torr region.
5. Deposit a molecular beam spot on the burn paper. The spot should be well defined and rectangular.
6. Open the x-ray shutters and shine the beam on the burn paper. This will change the color of the burn paper and indicate the position of the x-ray beam. In principle, the x-ray should pass through the center of the rectangular supersonic beam spot. If this is not the case, adjust the z position

of the diffractometer table accordingly. Move the motors *zne*, *znw* and *zs* together in a relative manner.

7. Now that the supersonic molecular beam spot and the x-ray beam spot are aligned, deposit a thermal spot and verify that the effusive beam spot perfectly overlaps the supersonic spot. Adjust the position of the mask by moving the motor *tmask* until this is the case.

After carrying out these steps, all three components should be properly aligned: the supersonic molecular beam, the thermal effusive beam, and the synchrotron x-ray beam. At this point, a sample can be loaded and x-ray experiments can be carried out. The following will outline the procedure of monitoring thin film growth via real time x-ray scattering.

1. Load a sample, and transfer it from the load-lock to the main chamber.
2. Carry out preliminary x-ray scans to move the sample into the center of rotation of the x-rays. First, make sure the APD is blocked by a piece of lead, and shine the unattenuated x-ray beam on the sample, using the I3 ion chamber to measure the beam.
3. Do a scan with the *chamy* motor and move the sample such that the x-ray beam is split in half. Follow this with a rocking scan in *zeta* and move the sample to the center of rotation. Iterate these scans until the positions of *chamy* and *zeta* do not change.
4. Now that the sample is in the center of rotation, remove the lead from in front of the APD detector, adjust the attenuator appropriately, and move *mu* and *zeta* to the correct positions for specular reflection at the anti-Bragg position. The exact angles will depend on the molecule of interest and the x-ray energy.

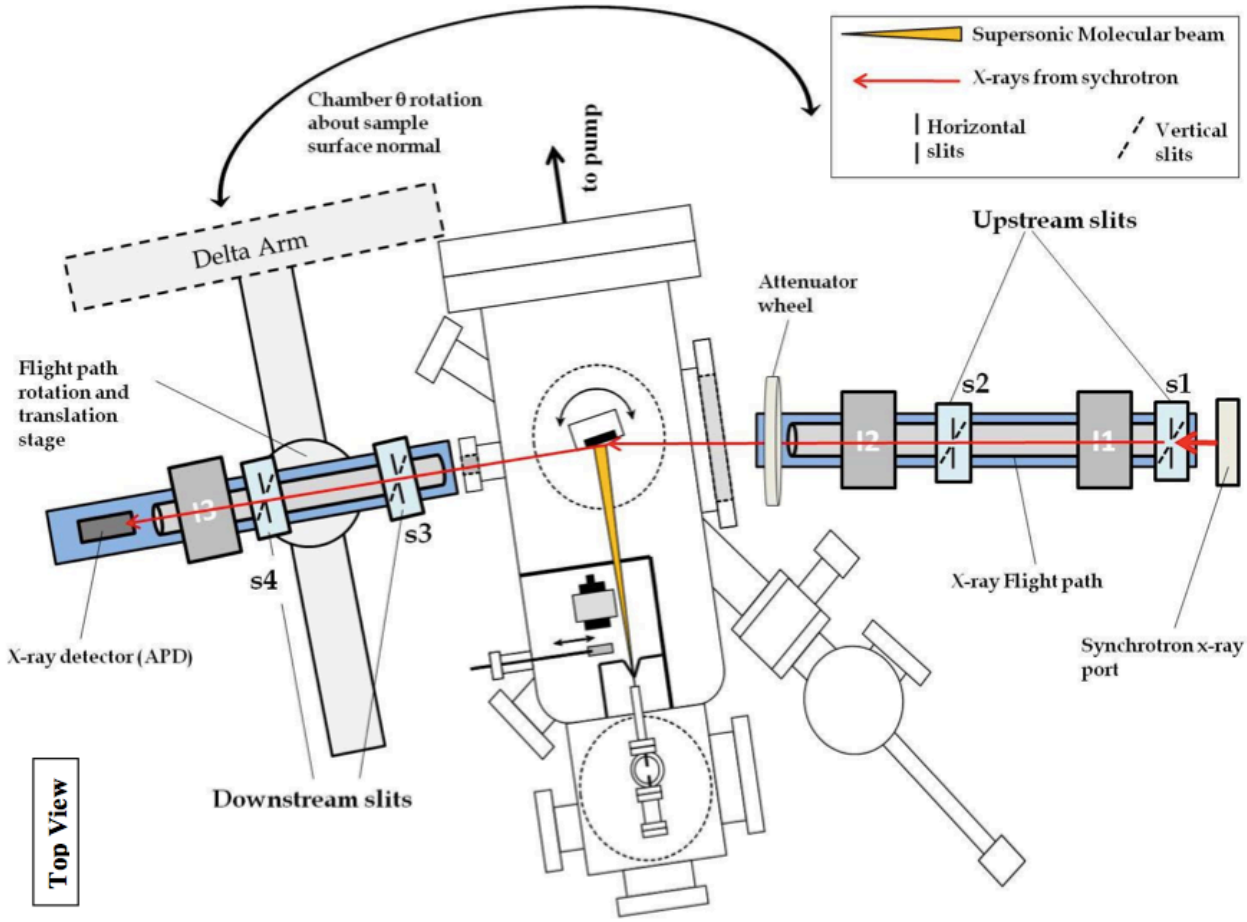

Figure 2.5: Diagram depicting the UHV chamber on the diffractometer table in the G3 hutch. The locations of the upstream and downstream slits are indicated.

5. Perform finer rocking scans in *zeta* and move the substrate to the peak intensity of the rocking curve. Perform a narrow scan in *del* to maximize reflected intensity.

6. Once the sample is in the center of rotation and both mu and zeta angles are set appropriately, perform a *tseries* scan, open the shutter of the desired source, and collect data. If all these steps have been performed correctly, anti-Bragg oscillations should be observed.

Figure 2.6 shows a picture of the G-Line chamber set up in the G3 hutch, ready to perform x-ray experiments to monitor organic thin film growth.

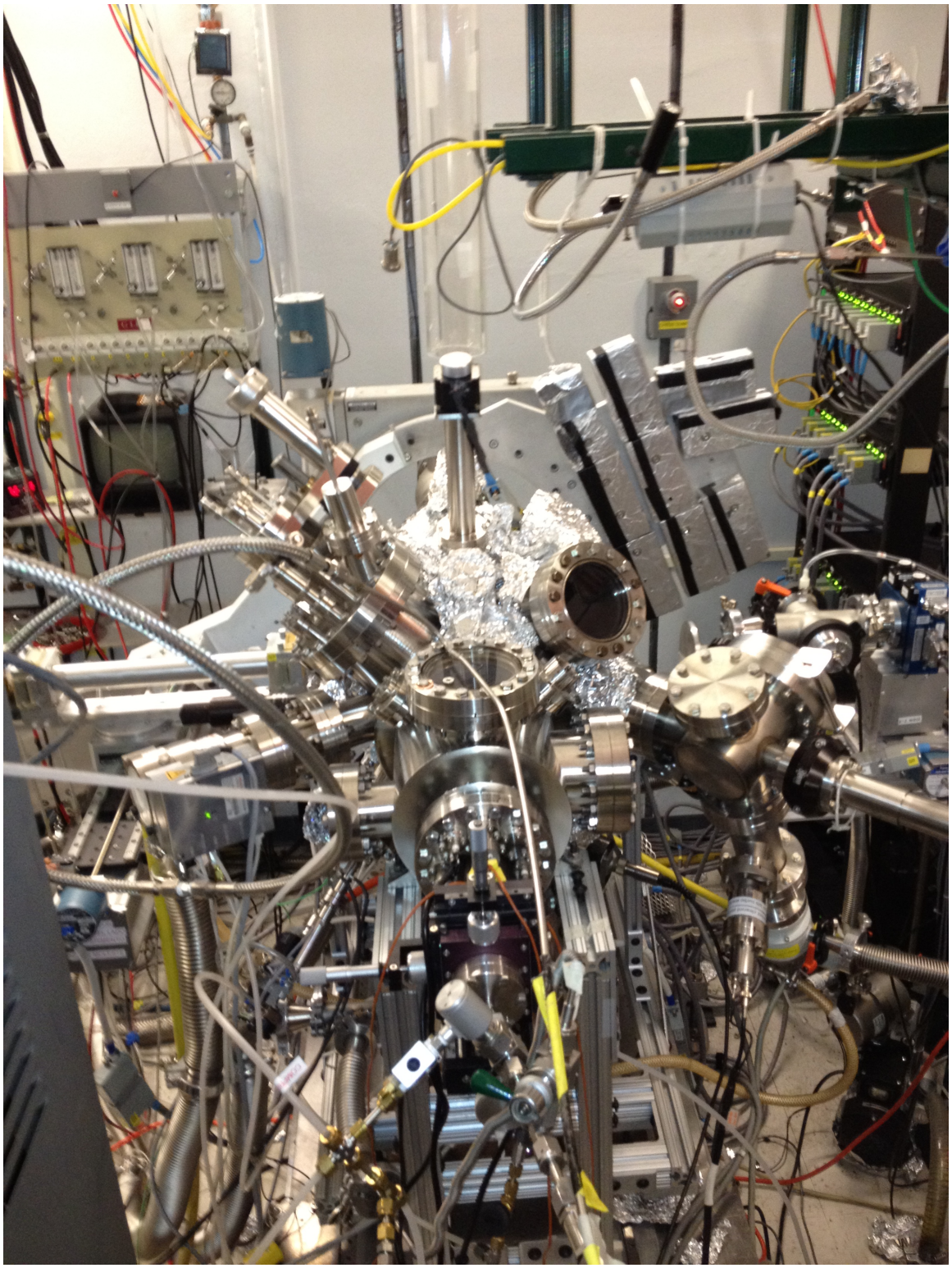

Figure 2.6: Photograph depicting the UHV chamber set up in the G3 hutch, ready to perform experiments.

2.2.4 Time of flight (TOF) experiments

In order to measure the kinetic energy of the supersonic molecular beams described in this work, time-of-flight (TOF) mass spectrometry was used. The energy can be determined by measuring the time required for the molecules to travel a given distance. From distance and time, a velocity can be calculated, and then from velocity and mass, kinetic energy. The procedure described here is summarized from reference **[3]**, and this reference should be consulted for additional details.

To take such measurements, a quadrupole mass spectrometer (Extrel 5221) was mounted on a linear translation stage attached to a 4-way, 6″ cross flange. The cross flange was mounted to the 12″ flange. This puts the QMS on the same axis as the molecular beam. The distance between the rotating blade chopper located in the ante-chamber and the QMS ionizer can be varied easily and precisely by adjusting the position of the linear translation stage. The sample manipulator was rotated to face the horizontal Be window, such that it would not block the molecular beam. The QMS settings used were: emission current = 3 mA, electron energy = 70 eV, multiplier (DeTech, 402A-H) voltage: 2.0 kV.

The data from the QMS was acquired using a multi-channel scalar card (ORTEC MCS-pci) with a sampling dwell time of 1 μs and a pass length of 17000. The MCS card was triggered by a photo-interruptor mounted on the chopper assembly housing which detects the passing of the blade. When the interruptor is 'chopped' (when the blade passes through the interruptor) a TTL pulse is sent from the chopper controller to the MCS to start or stop accepting counts. The chopper controller was custom designed by Dr. John Carter. He is to be consulted if any difficulties arise with the controller. This controller also controls

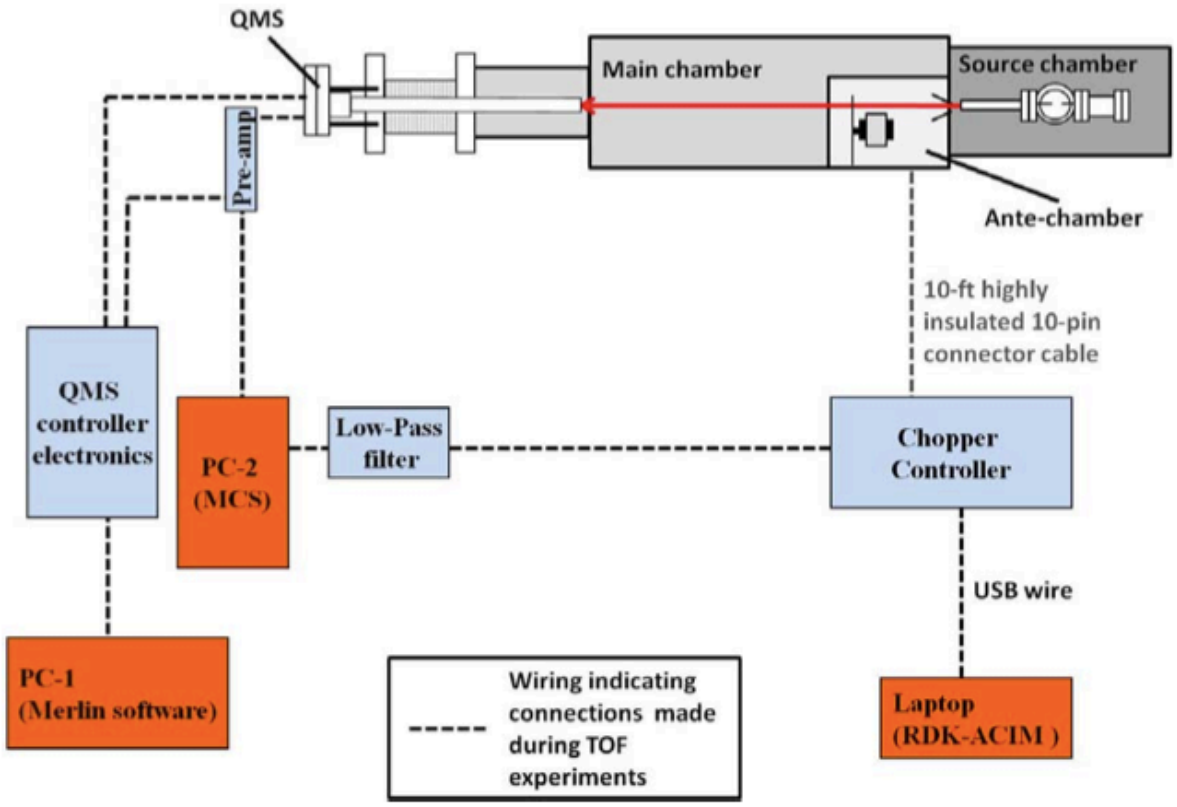

Figure 2.7: Diagram indicating the connections between pieces of equipment required to perform TOF experiments.

the motor. Figure 2.7 shows a diagram depicting how each component of this system is connected.

Experimental conditions during the TOF experiments were the same as those outlined in Table 2.1. In this work, TOF experiments were carried out for PTCDI-C_5 and PTCDI-C_8, as the other molecules studied had been examined in prior work. See **[2]** for pentacene and **[3]** for DIP and PTCDI-C_{13}. At each He flow rate, TOF spectra were taken at five different distances between the chopper blade and the QMS ionizer, as this distance can be easily varied by ad-

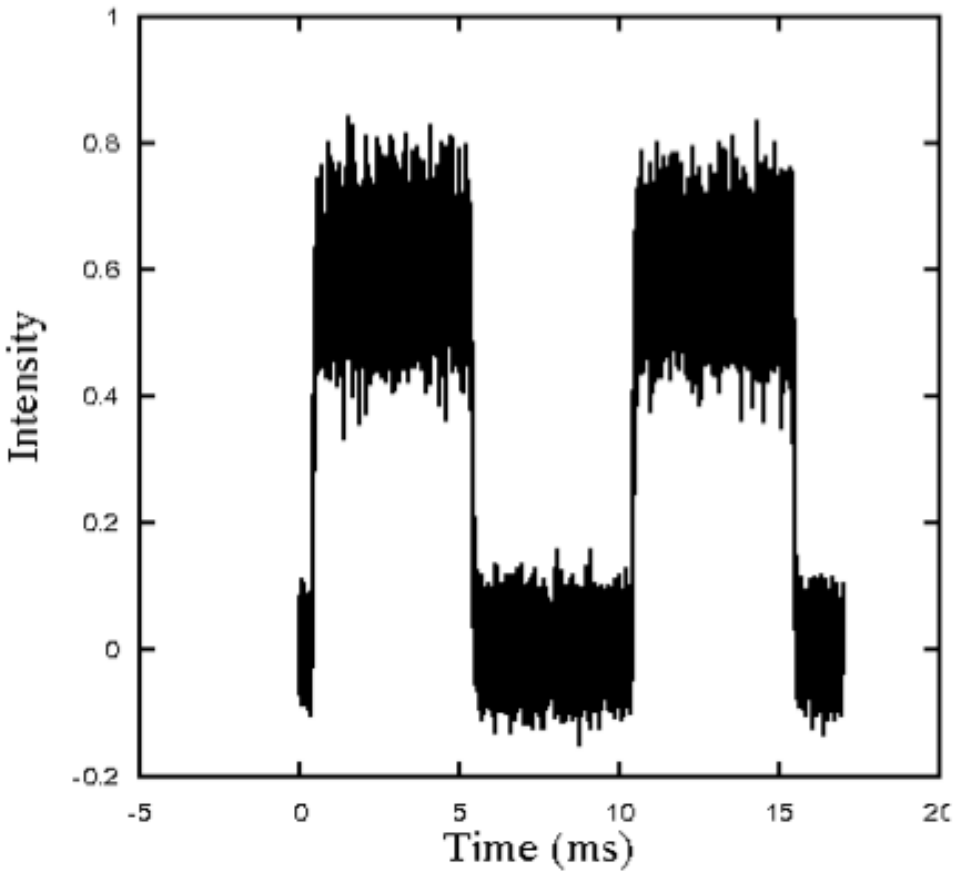

Figure 2.8: TOF spectrum of a PTCDI-C_5 supersonic molecular beam at a He flow rate of 10 sccm.

justing the linear translation stage. Knowing the precise distance between the blade and ionizer is less important than knowing the relative distance between each experiment (which can be easily and accurately measured). A sample TOF spectrum is presented in Figure 2.8 for PTCDI-C_5 at 10sccm He flow. The repeating square wave form is expected, as this experiment used a 25/25 chopper blade. And in Figure 2.9, the leading edges of TOF spectra for PTCDI-C_5 at 10 sccm He flow are shown at three different QMS positions. From these spectra, a linear relationship between time of flight and QMS position can be obtained. The slope of this line can be used to calculate velocity, and therefore kinetic energy.

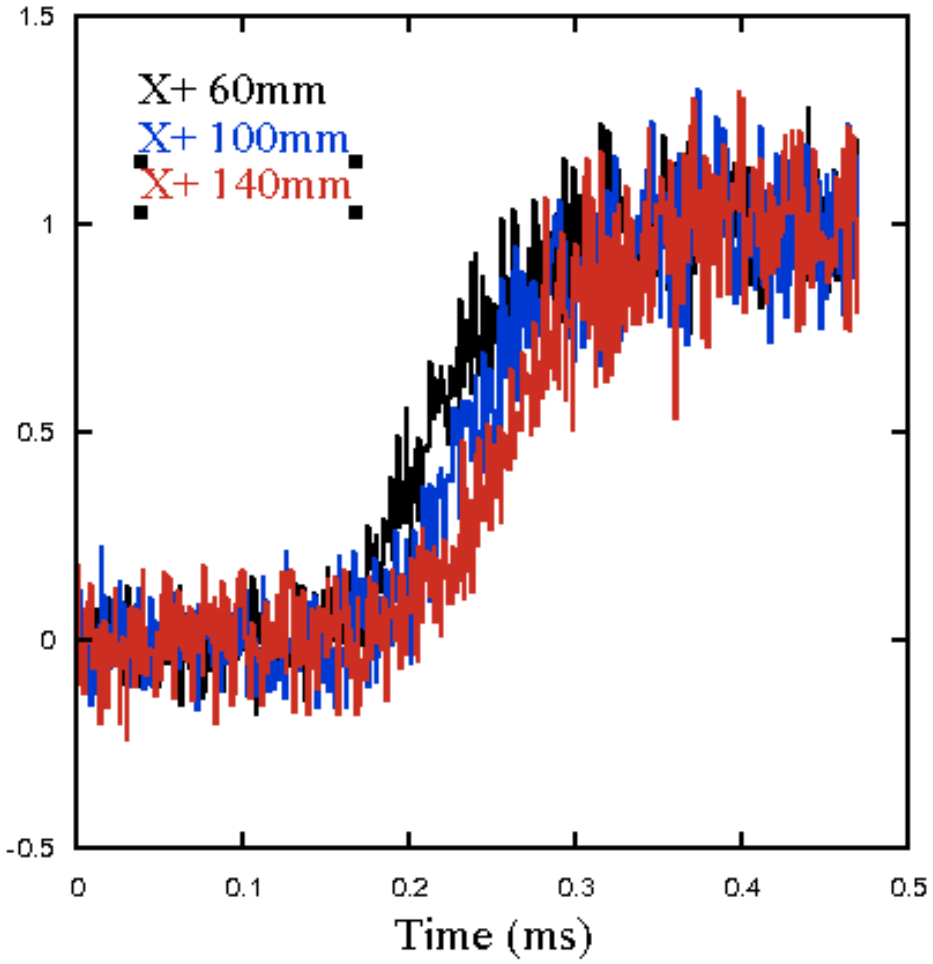

Figure 2.9: Rising edge of three TOF spectra of a PTCDI-C_5 supersonic molecular beam at a He flow rate of 10 sccm and three different QMS positions. These data imply a kinetic energy of 4.2 eV.

Unfortunately, after taking only a set of TOF data for PTCDI-C_5 at a He flow rate of 10 sccm, the QMS ceased functioning. It is possible to theoretically calculate the kinetic energy of a supersonic molecular beam. Scoles **[10]** gives an expression for the average energy as:

$$\langle E_i \rangle = \frac{m_i}{\langle m \rangle} \langle C_p \rangle T_n \tag{2.1}$$

However, this is an ideal expression that provides only an upper bound on the possible average kinetic energy. The difference between this value and the mea-

sured kinetic energy is termed velocity slip. This is a non-continuum, translational relaxation effect between the two gas species. A detailed analysis based on kinetic theory can be applied to produce an empirical expression for the velocity slip parameter, VSP.

$$VSP = \frac{(\mu_{ij}\bar{m})^{1/2}}{|m_j - m_i|} n_0 d\sigma_{ij}^2 \Omega_{ij}^{(11)^*} \tag{2.2}$$

where μ_{ij} is the reduced mass, $\bar{m}$ is the mole fraction average mass, d is the nozzle diameter, n_0 is the density, and $\sigma_{ij}\Omega_{ij}^{(11)^*}$ is the collision integral for the carrier-dilute molecule combination. Modeling of molecular interactions has led to an empirical relationship that can be used to calculate the collision integral:

$$\sigma_{ij}^2 \Omega_{ij}^{(11)^*} = 0.96 \left(\frac{C_6}{kT_N} \right)^{1/3} \tag{2.3}$$

in which C_6 is the r^{-6} parameter in the Lennard-Jones potential energy function for the carrier-dilute molecule pair. It can be calculated using tabulated values for individual C_6 values using $C_6 = (C_{6i} \times C_{6j})^{1/2}$.

Making accurate use of these relations requires the knowledge of a number of physical properties of the carrier gas and the organic molecule of choice. While helium, the carrier gas used here, has been well studied, the organic molecules have not. Values for the heat capacity and vapor pressure as a function of temperature for PTCDI-C_5 and PTCDI-C_8 are simply not known.

A simpler way to estimate the kinetic energy of supersonic molecular beams of PTCDI-C_5 and PTDCI-C_8 is to use data from PTCDI-C_{13} experiments. This can be done by assuming the velocity of each molecule is the same for the same stagnation pressure. This implies that each beam has the same seeding ratio, and each molecule has the same heat capacity, C_P. This is reasonable, as the bubbler temperature was controlled to give approximately the same flux for

He Flow (sscm)	PTCDI-C_{13}	PTCDI-C_8	PTCDI-C_5
10	**6.3**	*5.1*	**4.2**
25	**8.8**	*7.2*	*6.2*
70	**12.8**	*10.4*	*9.0*
90	**14.3**	*11.6*	*10.0*

Table 2.2: Supersonic molecular beam energies (eV)

each molecule, which implies similar vapor pressures and seeding ratios. And as the molecular structures are so similar, one would not expect wildly different heat capacities. Table 2.2 shows a summary, where known energies are listed in bold, and estimated energies in italic.

Comparing the estimated value of kinetic energy for PTCDI-C_5 at a carrier flow rate of 10 sccm (4.43 eV) to a successful time-of-flight measurement of PTCDI-C_5 (4.2 eV), we are confident that this estimation provides reasonable values for incident kinetic energy of PTCDI-C_5 and PTCDI-C_8.

2.3 Sample preparation

This section will discuss the procedures involved with sample preparation. The first step is the formation of thermal oxide (SiO_2). This thermal oxide is then cleaned thoroughly before deposition of organic semiconductors, or before growth of self-assembled monolayers.

2.3.1 Thermal oxide formation

Substrates are Si (100) wafers (Wacker-Siltronic, *p*-type, 4″ diameter, 500-550 μm thick, 38-63 Ω-cm) subject to an RCA-1 clean, a 15 second HF dip and an RCA-2 clean immediately before growth of SiO_2. The approximately 300 nm thick oxide films were grown via wet thermal oxidation at 1100 °C, with a growth time of ~55 min. This was carried out in the thermal oxide furnace at the Cornell Nanfabrication Facility (CNF). After oxide growth, the 4″ wafers were cut into small samples of ~2.5 cm × 0.7 cm and subjected to further cleaning before deposition of organic semiconductors, or before growth of self-assembled monolayers.

2.3.2 Thermal oxide clean

Immediately prior to organic thin film deposition, or SAM formation, the cut SiO_2 wafer pieces were subjected to a rigorous cleaning procedure to remove any macroscopic particles or organic contamination. First, the wafer pieces were sonicated in chloroform (J. T. Baker 99.8% HPLC grade) for 15 minutes. Following this, they were sonicated in deionized (DI) water for 15 minutes. The samples were then washed with DI water and dried with nitrogen. Finally, they were subjected to an ultraviolet light-ozone clean (UV/O_3) for 15 minutes to remove any remaining organic residue. Immediately after this, the samples are transferred to the G-Line system to organic film growth, or subjected to SAM formation.

2.3.3 Formation of self-assembled monolayers (SAMs)

The following SAMs (all from Gelest Inc.): octadecyltrichlorosilane (ODTS), octyltrichlorosilane (OTS), 1-napthylmethyltrichlorosilane (NMTS) and 6-phenylhexyltrichlorosilane (PHTS), were all grown on SiO_2 wafers in solution form. See section 1.2 regarding the chemical structure of these SAMs. Deposition was performed as per the method outlined in reference **[4]**, in a glove box (Unilab, M. Braun Inc.) with a nitrogen atmosphere, [O2] < 2 ppm and [H2O] < 1 ppm. All glassware was rinsed with acetone (Mallinckrodt Chemicals CMOS grade), isopropanol (J. T. Baker - HPLC grade) and DI water, followed by baking at 150 °C overnight before use. All solutions were 10 mM concentration of the SAM precursor in anhydrous toluene (Sigma Aldrich Corp., >99%). The SiO_2 substrates were dipped in the SAM solution for 2 days and left in the glove box undisturbed. After 48 hours, the samples were removed from the solution and rinsed sequentially in anhydrous toluene, anhydrous acetone (Sigma Aldrich Corp., >99%) and chloroform (Sigma Aldrich Corp., HPLC grade, >99%) and finally drying with nitrogen. The samples were then stored in cleaned fluoroware containers and transferred to the G-Line system for organic thin film growth.

Hexamethyldisilizane (HMDS) and Perflurooctyltrichlorosilane (FOTS) were deposited via a vapor phase process. HMDS was deposited from the vapor phase using a YES LP-III vapor priming oven. The substrates were held at 150 C and underwent several successive evacuation and purge cycles to completely dehydrate the surface before exposure to HMDS vapor. FOTS was deposited using an MVD-100 system. In this tool, the deposition chamber was exposed to an oxygen plasma pre-clean step prior to exposure to FOTS vapor and SAM growth. After SAM deposition, the samples were removed from the tool and

stored in clean fluoroware containers to be transferred to the G-Line system for organic thin film growth.

2.4 X-ray scattering from thin films

X-ray scattering at the anti-Bragg position was employed to monitor the *in situ* real-time growth of organic semiconductors on SiO_2 and SiO_2 modified with SAMs, and the formation of organic heterostrctures. Specular x-ray reflectivity (XRR) was used to characterized the crystal structure of organic thin films, giving information about the crystal perpendicular to the substrate surface. Grazing incidence diffraction (GID) was used to characterize the crystal structure of organic thin films, giving information about the crystal parallel to the substrate surface. In the following sections, basic concepts of x-ray scattering will be discussed to enable the reader to better understand the results presented in this work. This is meant to be a brief overview. For further details, consult the texts and publications referenced in the following sections.

2.4.1 Optical constants

This section is adapted from references **[5,6,7]**. X-rays are electromagnetic waves characterized by wavelengths on the order of 1 Å. For electromagnetic waves, reflection and refraction at interfaces between media are characterized by the index of refraction, n, for both media. In a vacuum, $n = 1$. The refractive index can be split into dispersive and dissipative parts, written as

$$n = 1 - \delta + i\beta \tag{2.4}$$

The dispersive portion, δ, is proportional to the electron density, ρ_{el}, of the medium, while the dissipative part, β, is related to the linear absorption coefficient, μ:

$$\delta = \frac{\lambda^2}{2\pi} r_0 \rho_{el} \qquad \beta = \frac{\lambda}{4\pi}\mu \tag{2.5}$$

where λ is the x-ray wavelength and r_0 is the Thompson scattering length (or the classical electron radius). The linear absorption coefficient describes the extent to which x-rays are attenuated in the material. Typical values of δ range between 10^{-5} and 10^{-6}, whereas β is much smaller, typically between 10^{-6} and 10^{-9}. From classical optics, Snell's law relates the angle of incidence, α_i, to the refractive index, n, and the refracted angle, α_n:

$$\cos\alpha_i = n\cos\alpha_n \tag{2.6}$$

For x-rays, $n < 1$. This implies that below a certain incident angle called the critical angle, α_c, total external reflection occurs. In this case, all incoming radiation is reflected and x-rays do not penetrate far into the medium. Based on equations 2.4 and 2.6, we can derive an expression for α_c. Starting with equation 2.6 and inserting α_c for the incident angle and zero for the refracted angle:

$$\cos\alpha_c = 1 - \delta + i\beta \tag{2.7}$$

We can assume β is small enough to be negligible, and replace the cosine term with a Taylor series expansion, keeping only the first two terms:

$$\cos\alpha_c \approx 1 - \frac{\alpha_c^2}{2} = 1 - \delta \tag{2.8}$$

$$\alpha_c = \sqrt{2\delta} = \lambda\sqrt{\frac{r_0\rho_{el}}{\pi}} \tag{2.9}$$

Thus, we can see the critical angle is dependent on the x-ray wavelength and the electron density of the medium. For example, bulk SiO_2 has an electron density

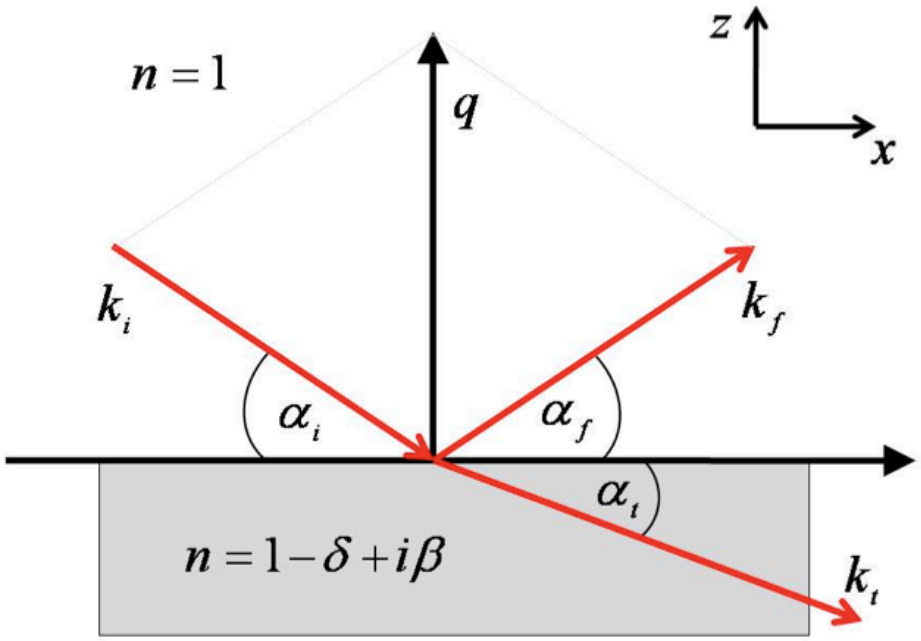

Figure 2.10: An electromagnetic plane wave is incident on a surface with wave vector $\mathbf{k}_i$ at a grazing angle, α_i. Part of the wave is reflected with a wave vector $\mathbf{k}_f$ at an angle α_f, and part is refracted at an angle α_t. Snell's law of refraction and the Fresnel equations can be derived by requiring continuity at the interface. The wave vector transfer, $\mathbf{q}$, is the change in momentum between the incident and reflected waves.

of $\rho_{el} = 0.671\text{Å}^{-3}$, so for an x-ray beam of wavelength $\lambda = 1.3\text{Å}$, we can calculate a critical angle of $\alpha_c = 0.182°$.

A schematic representation of x-ray scattering at an interface is shown in Figure 2.10. In this diagram, q is the wavevector transfer, or the scattering vector, defined as

$$q = \mathbf{k}_i - \mathbf{k}_f \tag{2.10}$$

where $\mathbf{k}_i$ and $\mathbf{k}_f$ are the incident and final diffracted wave vectors. For an elastic scattering event, $|\mathbf{k}_i| = |\mathbf{k}_f| = 2\pi/\lambda$.

2.4.2 Specular x-ray reflectivity

Specular x-ray reflectivity (XRR) measurements were conducted to determine the crystal structure and interface structure of organic thin films perpendicular to the surface. In specular XRR, $\alpha_i = \alpha_f$ and $q = q_z$ with $q_x = q_y = 0$, therefore only information regarding the electron density along the surface normal can be extracted from specular XRR data.

Prior to extracting information, the measured intensity, I_m, from the x-ray detector must first be corrected. The footprint, F, of the x-ray beam on the sample surface can be determined by the beam size, T, and the incident angle, θ, using the following relation:

$$F = \frac{T}{\sin\theta} \tag{2.11}$$

At low angles, F will be larger than the sample dimension, S, requiring I_m to be corrected using the following relation, such that only the beam impinging on the sample is contributing to the total corrected intensity, I_{cor}:

$$I_{corr} = I_m \frac{T}{\sin\theta}\frac{1}{S} \tag{2.12}$$

An example of specular XRR of a thin film of PTCDI-C_8 on SiO_2 is shown in Figure 2.11. The scattered intensity exhibits Bragg peaks up to the third order, with well-defined Laue oscillations around the Bragg peaks that are characteristic of a well ordered, lamellar structure. The following can be inferred from the data plotted in Figure 2.11 and illustrated in Figure 2.12:

1. The position of the Bragg peak (in q_z-space) can be used to calculate the height of the unit cell, d_{001}, can be determined. The spacing of the $(00n)$ Bragg peak is related to the unit cell height by $d_{00n} = 2n\pi/q_z$

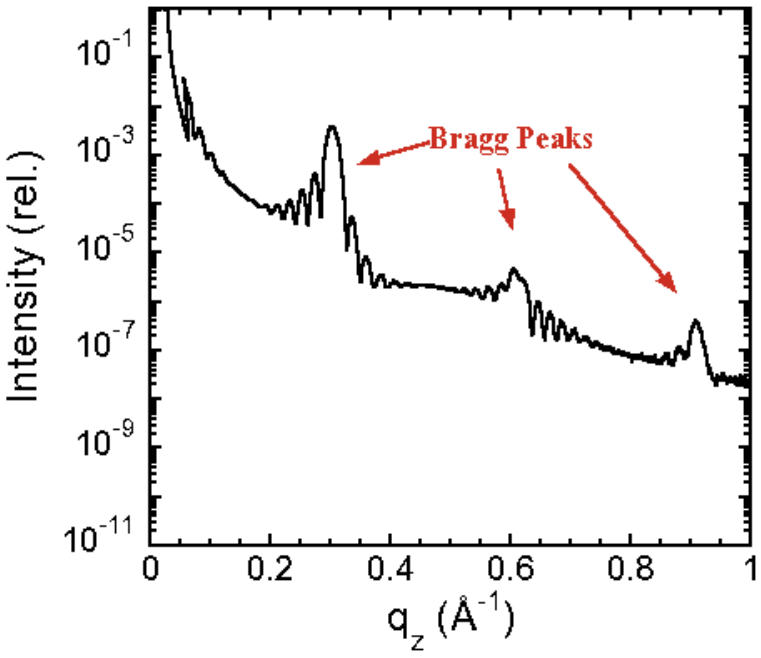

Figure 2.11: Specular x-ray reflectivity from a thin film of PTCDI-C_8 deposited on SiO_2. Bragg peaks up to the third order can be seen

2. The coherent film thickness, D, can be determined from the period of the Laue oscillations, Δq, around the Bragg peaks by the relation $D = \pi/\Delta q$.

The specular XRR can be fit using both the Parratt formalism (which accounts for multiple scattering events) and kinematic theory (which neglects multiple scattering). Parratt formalism has been used to fit specular XRR of SAMs, as described in detail in reference [3]. Specular XRR of organic films is not fit quantitatively in this work, and this data is analyzed using the features described in Figure 2.11 mainly to extract film thickness and d_{001} lattice parameters. Kinematic theory is used to model the real time, *in situ* x-ray data, and is described in more detail in section 2.4.4.

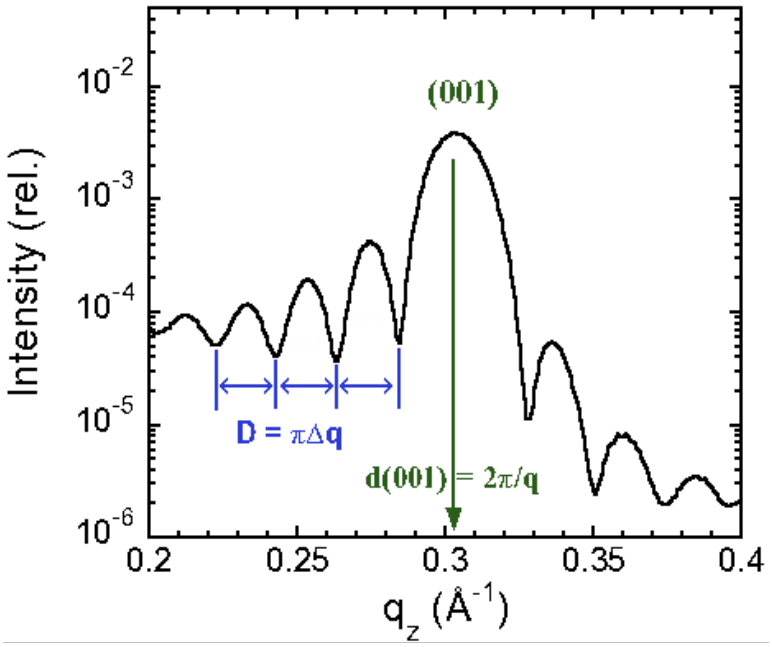

Figure 2.12: The (001) Bragg peak from Figure 2.11. Laue oscillations can be seen.

2.4.3 Grazing incidence diffraction (GID)

The previous section discussed the use of x-ray reflectivity to probe the crystal structure of a film normal to its surface. Grazing incidence diffraction (GID) is a method of probing the in-plane structure of a film. Figure 2.13 depicts the incident and diffracted x-ray beams during a typical GID experiment. Typically, the x-ray beam is incident near or below the critical angle, resulting in total external reflection. This ensures that very little scattering comes from the substrate, resulting in a high surface selectivity. The incident x-ray beam is diffracted by the crystal planes of the thin film. As all of the molecules studied in this work form ordered films with the long axis normal to the substrate surface, diffraction peaks for the (*hkl*) planes can be measured. In the case of GID, the wave vector transfer is split into two components: parallel and perpendicular to the surface.

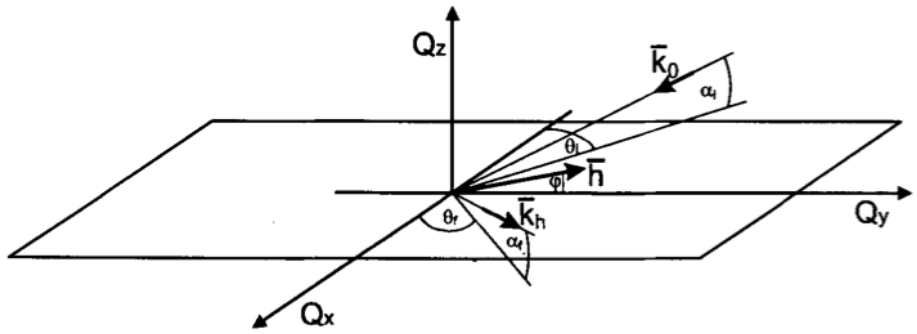

Figure 2.13: Illustration of incident and diffracted beams during a GID experiment. The incident angle, α_i, is held fixed while the detector can scan different values of α_f and θ_f to probe reciprocal space in three dimensions **[11]**.

Grazing incidence scans can be performed *in situ* in the G3 hutch, or *ex situ* in the G2 station at CHESS. When performed in the G3 station while the sample is still in the UHV chamber, the scan should be performed as follows:

1. The sample and x-ray beam should already be aligned, and a film deposited.
2. The *mu* and *zeta* motors should be set to about 0.1 and -0.05 degrees, respectively, and set the attenuator to an appropriate value.
3. Perform a short $\theta - 2\theta$ scan in *zeta* and *mu* to find the critical angle.
4. Move *mu* and *zeta* to the critical angle.
5. Move *del* to a starting point away from specular (around 5 degrees, typically).
6. Set the attenuator to zero, and perform a scan in *del*. You will have to integrate each point for several seconds.

Once the in plane peaks have been identified, by examining the peak width, it is possible to use the Scherrer equation to make an estimate of the in-plane

crystallite size:

$$\tau = \frac{K\lambda}{\beta \cos\theta} \tag{2.13}$$

Where θ is the Bragg angle, λ the x-ray wavelength, and β the FWHM of the Bragg peak. However, it should be noted that this relationship includes a shape factor, K, which is difficult to determine precisely, and thus, this relationship provides only an estimate. In addition, the footprint of the beam on the sample will cause additional broadening of the peak. This is especially important to consider when taking GID data in the G3 hutch.

2.4.4 *In situ* real time x-ray scattering at the anti-Bragg condition

In order to study the growth of thin films of organic semiconductors in real time on various substrates, *in situ* x-ray scattering at the anti-Bragg condition was used. This method is an effective monitor of the nature of growth, *i.e.*, layer-by-layer (LbL) vs. 3D islanded growth [8]. With this method, precise information about the film growth rate, individual layer coverages and film roughness can be obtained. The experiments detailed in this work followed this procedure:

1. X-ray scattering data was measured at CHESS, describing time resolved organic film growth.
2. This x-ray data was fit to a model, which allows for the extraction of film growth rate, evolution of individual monolayers, and film roughness.
3. The fit to the model was validated by *ex situ* AFM measurements.

The x-ray theory described in this section begins with the kinematic (or single scattering) approximation, which neglects multiple scattering events. This is a valid assumption for the case of a thin film where the scattering is far from the critical angle and far from the Bragg peak. This section is a brief description to ensure that the results presented in subsequent chapters can be well understood. For further details, please consult references **[8-10]**.

Kinematic approximation

The kinematic approximation can be simply stated as describing the scattered x-ray intensity as the Fourier transform of the electron density of the sample. The Fourier transform of the electron density function in real space, $\rho_{el}(\mathbf{r})$, gives the scattered amplitude in reciprocal space, which when squared gives the scattered intensity, $I(\mathbf{q})$. Thus,

$$I(\mathbf{q}) = \left| \int \rho_{el}(\mathbf{r}) e^{-i\mathbf{q}\cdot\mathbf{r}} d\mathbf{r} \right|^2 \tag{2.14}$$

In these real time experiments, the scattered x-ray intensity, I, is a function of time, while for specular reflection at the anti-Bragg point, $\mathbf{q} = q_z$ is fixed. The total electron density can be split into components describing the substrate and the growing thin film. The time dependence is contained in the thin film term, which itself can be written as a sum of n layers, each with a fractional coverage θ_n. This can be written as

$$I(t) = \left| r_{subs} e^{-i\phi} + r_{film} \sum_{n=1}^{\infty} \theta_n(t) e^{-iq_z dn} \right|^2 \tag{2.15}$$

where r_{subs} and r_{film} are scattering amplitudes of the substrate and thin film, ϕ is the phase change upon reflection, d is the out of plane spacing (which is, d_{001} described above), and $\theta_n(t)$ is the fractional coverage of layer n as a function of

time. At the anti-Bragg position, which is defined as one half the Bragg angle, $q_z = \pi/d$. This simplifies the above equation, such that the exponential term becomes -1 or 1 if n is even or odd:

$$I(t) = \left| r_{subs} e^{-i\phi} + r_{film} \sum_{n=1}^{\infty} \theta_n(t)(-1)^n \right|^2 \tag{2.16}$$

This will result in oscillations in intensity as the film grows, if growth is layer-by-layer. The parameters r_{subs}, r_{film}, and ϕ depend on the electron density of the starting substrate (e.g. SiO_2), the growing film (e.g. PTCDI-C_5), and any interfacial layer (e.g. SAM), as well as the thickness of any interfacial layer. As can be seen in later chapters, these parameters govern the 'shape' of the anti-Bragg oscillations. In addition, differences in the nature of the surface will also be seen as differences in relative intensities at $t = 0$, at the peak of the first oscillation, and for the 'saturation' intensity as $t \rightarrow \text{inf}$.

Modified Cohen model

Most of the work described here makes use of a modified version **[9]** of a model first described by Cohen et al. **[10]** to determine layer coverages as a function of time. The model is based on writing an expression for the change in coverage of layer n in terms of a few parameters to describe incident flux and downhill transport:

$$\frac{d\theta_n}{dt} = S_{n-1} F[(\theta_{n-1} - \theta_n) - \alpha_{n-1}(\theta_{n-1} - \theta_n)] + S_n F \alpha_n (\theta_n - \theta_{n+1}) \tag{2.17}$$

where the layer $n = 0$ represents the substrate, $n = 1$ the first molecular

layer, etc. S_n is the probability of adsorption for molecules incident on the n^{th} layer, F is the incident molecular flux, and α_n is the probability of downward interlayer transport. That is to say, α_n represents the probability that a molecule that initially forms part of layer $n+1$ will diffuse downwards to become part of layer n.

Equation 2.17 has three terms. The first term describes the rate at which molecules adsorb on the n^{th} layer, which is proportional to S_n (or the film growth rate) and the exposed area of the n^{th}layer, $\theta_{n-1}-\theta_n$. The second term is the fraction of those molecules from the first term that initially land on the n^{th} layer and then drop down to layer $(n-1)$. The last term contains the contribution from molecules that initially adsorb on the $(n+1)^{th}$ layer and subsequently drop down to the n^{th} layer. Figure 2.14 shows a diagram of these three processes.

Clearly, the set of terms α_n are important for calculating layer coverages, θ_n and eventually x-ray intensity. The α_n terms represent the probability of interlayer transport, and are proportional to the 'step edge density', $\Gamma(\theta)$, illustrated in Figure 2.14. A detailed description of this parameter can be found in reference **[9]**. The parameters S_nF and α implicitly represent all of the kinetic processes of molecular transport and attachment.

In this model, we assume that there are two values for the probability of adsorption. S_0 represents the probability of adsorption for a molecule incident on the bare substrate. For molecules incident on subsequent layers of the growing film, the probability of adsorption is the same for all layers ($S_1 = S_2 = S_3 = S_n$). As to the interlayer transport terms, we assume three values. The substrate is considered impermeable, thus $\alpha_0 = 0$, so we consider α_1, α_2, $\alpha_{\geq 3}$. 'Uphill' interlayer transport is not included in this model.

(a)

$$\frac{d\theta_n}{dt} = S_{n-1}F\left[(\theta_{n-1} - \theta_n) - \alpha_{n-1}(\theta_{n-1} - \theta_n)\right] + S_nF\alpha_n(\theta_n - \theta_{n+1})$$

(1) $S_{n-1}F\left[(\theta_{n-1} - \theta_n)\right]$

(2) $S_{n-1}F\left[\alpha_{n-1}(\theta_{n-1} - \theta_n)\right]$

(3) $S_nF\alpha_n(\theta_n - \theta_{n+1})$

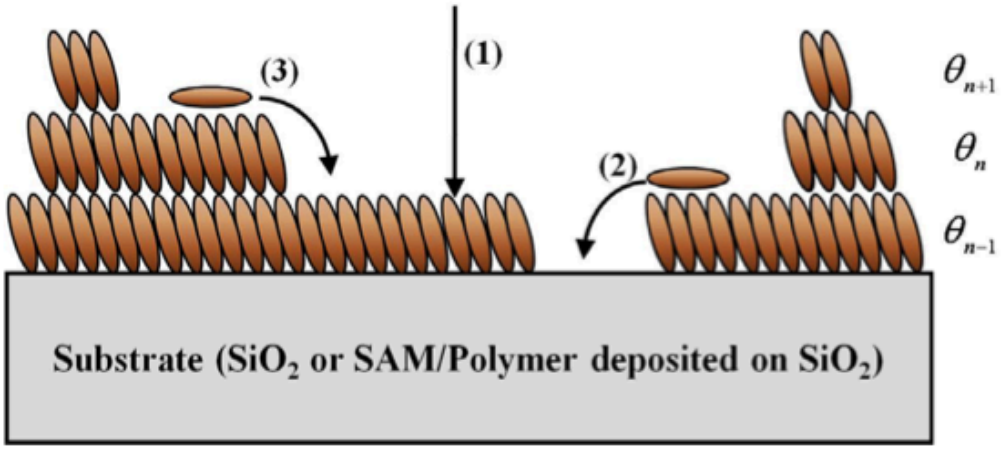

(b)

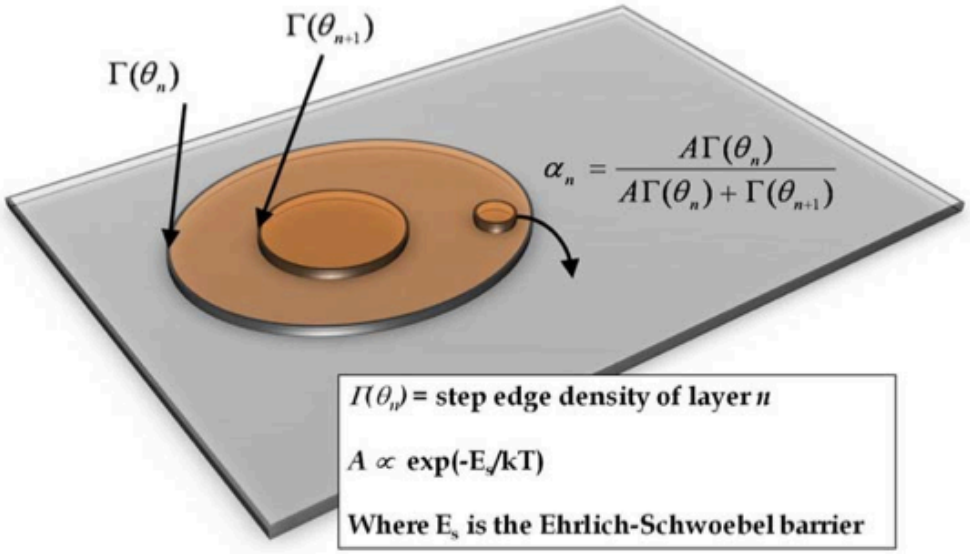

Figure 2.14: (a) Drawing illustrating the terms of the growth model described by equation 2.17. (b) Drawing illustrating the probability of 'downhill' transport as a function of a step edge density, $\Gamma(\theta_n)$, and an Ehrlich-Schwoebel barrier.

It is the set of α_n parameters that account for the processes of interlayer transport, which are extremely important to final film roughness and morphology. These parameters are calculated from the step edge density of layer n, $\Gamma(\theta_n)$, and the Ehrlich-Schwoebel barrier, E_{ES}:

$$\alpha_n(\theta_n, \theta_{n+1}) = \frac{e^{-E'}\Gamma(\theta_n)}{e^{-E'}\Gamma(\theta_n) + \Gamma(\theta_{n+1})} \tag{2.18}$$

where $E' = E_{ES}/k_BT$.

Having calculated the layer coverages, $\theta_n(t)$ using equation 2.17, they can be inserted into equation 2.16 to calculate the scattered x-ray intensity, $I(t)$. In general, the intensity is measured at CHESS, then the data is fit using equations 2.17 and 2.16. From the fit, the desired parameters can be extracted (e.g. growth rate, layer coverages, relative adsorption probabilities). The root-mean-squared (RMS) roughness (r) of the film can be calculated as a function of growth time from the layer coverages:

$$r(t)^2 = \sum_n n^2(\theta_n(t) - \theta_{n+1}(t)) - \left|\sum_n n(\theta_n(t) - \theta_{n+1}(t))\right|^2 \tag{2.19}$$

Examples

It is instructive at this point to consider the extremes of film growth modes, and how these cases might be observed via x-ray scattering at the anti-Bragg condition. In Figure 2.15 we illustrate four different growth modes: the extremes of perfect layer-by-layer growth and 3d island growth, and two intermediate cases. Perfect layer-by-layer growth results when interlayer transport is extremely quick, corresponding to low energetic barriers.

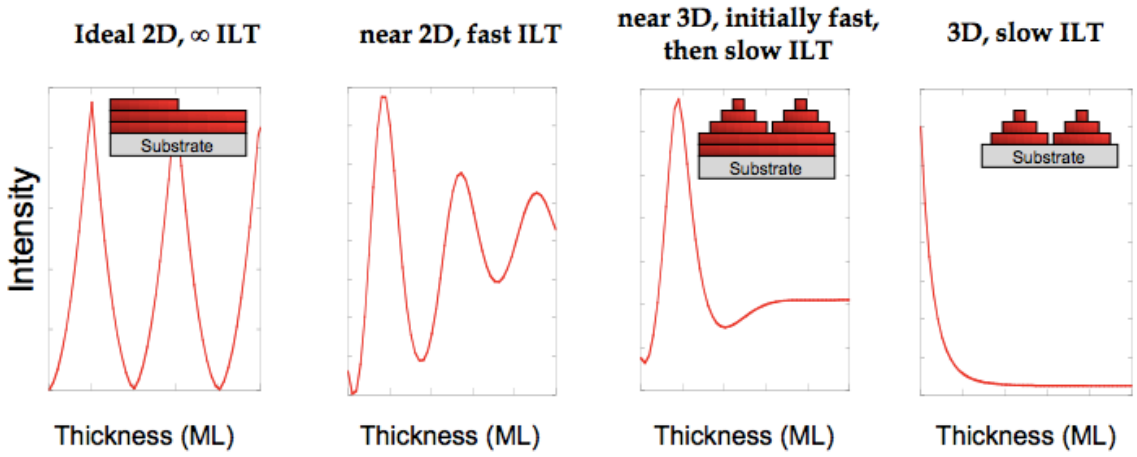

Figure 2.15: Possible thin film growth modes and the resulting x-ray intensity oscillations at the anti-Bragg point. The growth mode is highly dependent on rates of interlayer transport.

If we consider the case of perfect layer-by-layer (LbL) growth, each layer of the film will go to complete coverage before the next layer begins to form. Physically, this corresponds to a system with low Ehrlich-Schwoebel barriers and rapid interlayer transport. The x-ray intensity, $I(t)$ oscillates with a period of 1 ML per oscillation, and the oscillations do not damp, but persist indefinitely. For nearly 2D growth, the oscillations do become damped as the film slowly increases in roughness. For near 3D growth, the oscillations are quickly damped, and after the first 1-2 ML no more oscillations are observed. In the case of perfect 3D island growth, $I(t)$ decays exponentially as the film rapidly becomes very rough.

The roughness evolution as a function of film thickness can also be predicted by our model using known layer coverages, $\theta_n(t)$, and Equation 2.19. For the four hypothetical cases considered here, the roughness as a function of film thickness is plotted in Figure 2.16. For perfect LbL growth, the RMS rough-

ness oscillates between 0 and $\frac{1}{2}$ML, with the maximum roughness occurring at coverages of $n + \frac{1}{2}$ML. The other extreme of perfect 3D growth sees roughness increase as $\sqrt{\theta}$, as expected from Poisson statistics. The intermediate cases begin similarly to LbL growth, but then approaching 3D growth. The cases are plotted in Figure 2.16. By comparing roughness obtained from model fits to x-ray data with *ex situ* AFM, the validity of the model can be tested. For a detailed description validating this model and an examination of pentacene and DIP growth on SiO_2, refer to **[3, 9]**.

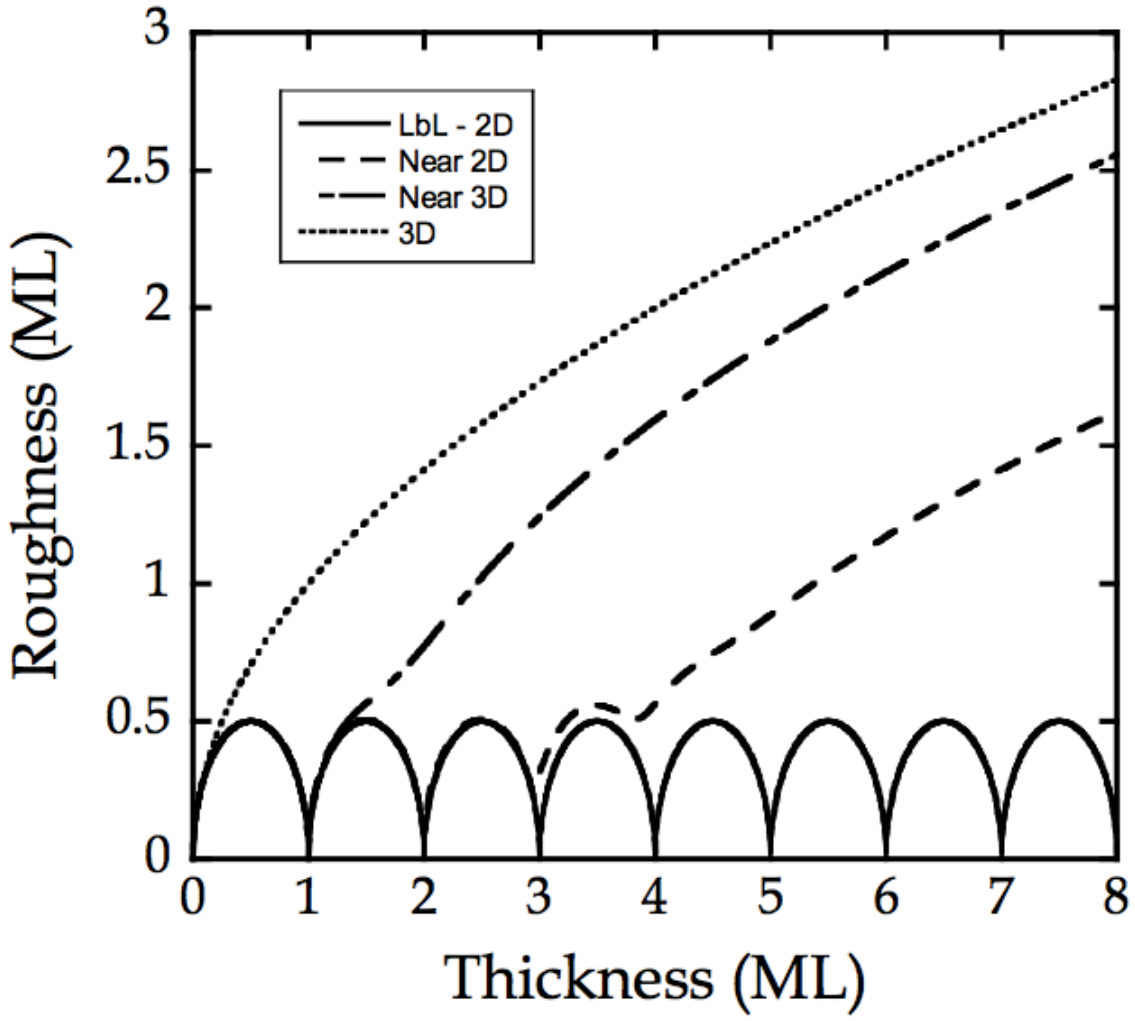

Figure 2.16: Roughness evolution of thin film growth as a function of film thickness for the case of perfect LbL growth (solid line), near 2D growth (dashed line), near 3D growth (small dash/big dash line), and perfect 3D growth (dotted line).

2.5 References

1. Killampalli, A. S. *Cornell University: PhD Thesis* **2006**.
2. Schroder, T. W. *Cornell University: PhD Thesis* **2004**.
3. Desai, T. V. *Cornell University: PhD Thesis* **2011**.
4. Chen, R.; Kim, H.; McIntyre, P. C.; Bent, S. F. *Chem. Mater.* **2005**, *17*, 536-544.
5. Nielsen, J. A.; McMorrow, D. *Elements of Modern X-Ray Physics* John Wiley & Sons Ltd **2001**
6. Tolan, M. *X-ray scattering from soft-matter thin films* Springer, Vol. 148, **1999**
7. Sivia, D. S. *Elementary Scattering Theory for X-ray and Neutron Users* Oxford University Press, **2011**
8. Kowarik, S.; Gerlach, A.; Skoda, M.; Sellner, S.; Schreiber, F. *Eur. Phys. J. Special Topics* **2009**, *168*, 11.
9. Woll, A. R.; Desai, T.V.; Engstrom, J. R. *Phys. Rev. B*, **2011**, *84*, 075479/1-075479/13.
10. Scoles, G. *Atomic and Molecular Beam Methods* (Oxford University Press, Oxford, UK, **1998**).
11. Holy, V.; Pietsch, U.; Baumbach, T. *High Resolution X-Ray Scattering from Thin Films and Multilayers* Springer **1999**

CHAPTER 3

NUCLEATION OF DIINDENOPERYLENE AND PENTACENE AT THERMAL AND HYPERTHERMAL INCIDENT KINETIC ENERGIES

3.1 Overview

We have examined the nucleation of diindenoperylene (DIP) on SiO_2 employing primarily atomic force microscopy and focusing on the effect of incident kinetic energy employing both thermal and supersonic sources. For all incident kinetic energies examined (E_i = 0.09-11.3 eV) the nucleation of DIP is homogenous and the dependence of the maximum island density on the growth rate is described by a power law. A critical nucleus of approximately 2 molecules is implicated by our data. A re-examination of the nucleation of pentacene on SiO_2, gives the same major result that the maximum island density is determined by the growth rate, and it is independent of the incident kinetic energy. These observations are readily understood by factoring in the size of the critical nucleus in each case, and the island density, which indicates that diffusive transport of molecules to the growing islands dominates the dynamics of growth in the submonolayer regime.

3.2 Introduction

Devices based on organic semiconductors have attracted considerable interest as they show great promise in a wide range of applications **[1]**. Compared to the diversity supplied by the field of organic chemistry, there are relatively

few promising candidates concerning the use of small molecules for these purposes. Diindenoperylene (DIP) **[2]** and pentacene **[3]** are two molecules that have shown relatively high charge transport mobilities (on the order of 0.1-1 cm^2-V^{-1}-s^{-1}) in device structures **[4]**, and both represent molecular structures described by fused aromatic building blocks with corresponding delocalized molecular orbitals. For some time it has been recognized that charge transport in organic thin film transistors is confined to the first few monolayers near the gate dielectric **[5]**, consequently considerable attention has been devoted to studying the initial stages of growth of thin films of these small molecules on insulating substrates. A perfect single crystal at the semiconductor—dielectric interface would be ideal, but its formation is difficult to say the least given the amorphous nature of most dielectric substrates, and the lack of covalent attachment that could drive true epitaxial growth. Thus, optimization of the microstructure of polycrystalline thin films in terms of the electrical properties that result is a common goal.

Thin films of small molecule organic semiconductors can be deposited using a variety of approaches, which include both solution-based **[6]** and vapor-phase based methods **[7]**. Concerning inorganic materials, the use of non-equilibrium approaches and/or energetic species (e.g., via the use of plasmas) to alter or manipulate thin film growth has been long recognized **[8]**. Similar approaches have been taken concerning the growth of small molecule organic thin films, particularly by the use of supersonic molecular beams, which afford exquisite control over the kinetic energy of the depositing species **[9, 10]**. Supersonic molecular beams have been employed both in studies of the efficacy of the effects of incident kinetic energy on thin film microstructure and morphology **[11-13]**, and fundamental examinations of the molecular scale mechanisms in organic thin

film growth **[14-24]**. Concerning the former, an early study making use of He atom diffraction showed that pentacene thin films grown on Ag(111) were more highly ordered when the incident molecules possessed a hyperthermal kinetic energy (E_i ~ 5 eV) **[11]**. This effect was, however, confined to a rather small window in substrate temperature (T_s ~ 200 K). Since this work was published a number of other effects have been attributed to incident kinetic energy **[12-13]**. Concerning the latter, in earlier work we have shown that the incident kinetic energy has a strong effect on the probability of adsorption **[14,15,21,23]**, and we have found that this probability depends on the coverage, particularly at high incident kinetic energies **[18,19,21,23]**.

The focus of the work presented here is an explicit examination of the early stages of growth of DIP on SiO_2, in particular how the (maximum) density of islands (N_{max}) vary with the overall rate of growth (*GR*), and how this depends on the incident kinetic energy of the molecules, from thermal to hyperthermal values of E_i. The density of islands formed in the submonolayer regime can strongly affect the size of the crystalline grains that are eventually formed in the thin film, and ultimately their electronic properties. In the case of homogeneous nucleation, the dependence of N_{max} on *GR* can directly give the size of the critical nucleus **[25]**. We will also re-visit an examination of nucleation of pentacene on SiO_2 **[14,26-29]**, including its possible dependence on E_i. We find that for both DIP and pentacene that our results indicate that the kinetic energy of the incident molecules has essentially no effect on nucleation, and the maximum density of islands that are formed can be described as a function of substrate temperature and growth rate.

3.3 Experimental procedures

The experiments that were conducted *in situ* and in real-time were carried out in a custom-designed UHV chamber that has been described in detail elsewhere **[30]** in the G3 station of the Cornell High Energy Synchrotron Source (CHESS). Briefly, the system consists of four separately pumped chambers: a main scattering chamber, a source and antechamber, which act to produce the supersonic beam, and a fast entry load-lock. All chambers are pumped by high-throughput turbomolecular pumps. The base pressure of the chamber was typically $\sim 4 \times 10^{-9}$ Torr and samples were loaded via the load-lock chamber, which was evacuated to $\sim 10^{-7}$ Torr prior to sample transfer into the main chamber.

Supersonic molecular beams of pentacene (99.8% Sigma-Aldrich Corp.) and DIP (99.8% purity) were generated by passing a carrier gas (He, 99.999%) through a temperature-controlled container (the evaporator) containing these species located upstream of the nozzle (150 μm orifice). The doubly differentially pumped beam passed through a trumpet shaped skimmer into an antechamber and through an aperture that produced a well-defined beam spot on the substrate surface. The mean kinetic energy of the molecules in the supersonic molecular beam can be controlled by adjusting the flow rate of the carrier gas. The mean kinetic energy of pentacene and DIP in these beams is measured by time of flight experiments **[30,31]**. During deposition the substrate temperature was kept at T_s = 40°C, and in all cases the supersonic beam was incident along the surface normal.

In addition to the supersonic molecular beam source, in the work report here we also make use of a more conventional thermal effusion source (CreaTec Fis-

cher & Co. GmbH) to generate near thermal energy incident fluxes of pentacene and DIP. This source possesses a 10 cm^3 crucible constructed of pyrolytic BN, and it is fitted with a pneumatically controlled shutter. In our system, the source is mounted directly to the main scattering chamber of UHV system (angle of incidence is 45° off the substrate surface normal, 10 cm from the substrate surface; as the adsorption probability for thermally evaporated molecules is considered unity, the incident angle has no effect on film growth), which also houses the sample. For deposition from the thermal source a translatable shadow mask, possessing a square 15 × 4 mm^2 opening, ~ 5 mm from the substrate surface, was used to define a beam spot on the sample. During these experiments, the thermal effusion source was heated to a temperature (*ca.* 160 °C for DIP, 105 °C for pentacene) to achieve the desired flux, the shadow mask was moved into place, and the shutter was opened and then closed to produce the desired exposure.

Substrates were Si (100) wafers (Wacker-Siltronic, *p*-type, 100 mm dia., 500-550 μm thick, 38-63 Ω-cm) subject to a SC-1 clean, a 15 s HF dip, and a SC-2 clean immediately before the growth of approximately 300-nm-thick SiO_2 films by wet thermal oxidation at 1100°C. Next, these wafers were cleaned and degreased by sonication in anhydrous $CHCl_3$ solution (99%+), sonicated in deionized (DI) water, washed with DI water, dried with N_2, and exposed to UV-ozone for 15 min. These processes provided a clean and reproducible hydrophilic surface.

Sub-monolayer thin films of pentacene and DIP were deposited for a range of different growth rates and incident kinetic energies. As the supersonic molecular beam produces a well-defined spot on the sample, and the shadow mask

likewise defines a spot from the thermal source, by translating the sample perpendicular to the deposition sources, up to four distinct thin films could be deposited on a single sample. To assist producing thin films with the desired coverages, the growth of several monolayer thin films was monitored using real time *in situ* synchrotron X-ray scattering at the anti-Bragg ($00^1/_2$) position, which gives a direct measurement of the growth rate **[16,22]**. All thin film samples were examined *ex situ* by AFM (Digital Instruments DI-3100) to facilitate a determination of both the density of islands and the total film coverage. In the results reported below we use the thin film coverage measured from AFM and the time of exposure of the sample to the vapor source to calculate the thin film growth rates, as we have shown that the growth rate in the submonolayer and multilayer regimes can differ, particularly at high incident kinetic energies **[18,21-23]**.

3.4 Results

3.4.1 DIP on SiO_2

In Figure 3.1 we present a series of AF micrographs for the growth of DIP on SiO_2 as a function of growth rate (*GR*). All experiments were conducted at T_s = 40 °C, and each image represents an area of 1.5 × 1.5 μm^2. The growth rate of DIP has been tuned by varying the temperature of the *in situ* evaporator, in the cases where the supersonic beam was employed as the source, which affects directly the incident molecular flux. For thermal deposition, the temperature of the source was adjusted appropriately, which has the same effect on

the *GR*. In all cases we observed single ML-tall high islands for these coverages ($0.0034 < \theta < 0.110$), and we also found no evidence for desorption of DIP. Thus, growth of DIP in the sub-monolayer regime for these conditions is classified as 2D, complete condensation **[25]**. The relative uniformity of the size and spacing of islands is also consistent with homogeneous nucleation and 2D complete condensation. The micrographs plotted in Figure 3.1 represent growth at thermal incident kinetic energy, $E_i \sim 0.09$ eV [Figs. 3.1(c,g)], and at $E_i = 4.2$ [Fig. 3.1(f)], 6.0 [Fig. 3.1(b,h)], 9.4 [Figs. 3.1(a,e)] and 11.3 eV [Fig. 3.1(d)]. In all cases the islands that are formed are similar in shape: compact, not exhibiting any obvious faceting. To the naked eye the island density appears to be solely a function of the GR, increasing with increasing *GR*, independent of E_i.

In the case of homogenous nucleation the maximum island density (N_{max}) for 2D growth and complete condensation scales with growth rate (*GR*) and is given by the following expression **[25]**:

$$N_{max} = \eta(\theta, i^*)(GR/D)^{i^*/(i^*+2)} \exp[E_{i^*}/(i^* + 2)k_B T_s] \tag{3.1}$$

where D is the tracer diffusivity of the molecule, i^* is the critical cluster size, E_{i^*} is the binding energy of the critical cluster and k_B is the Boltzmann constant. The critical cluster size is defined as the largest unstable cluster, such that a cluster with $i^* + 1$ molecules is more likely to grow than to decay. The dimensionless prefactor $\eta(\theta, i^*)$ is nearly a constantonly weakly dependent on i^* and coverage, θ. At a fixed temperature, N_{max} will vary with *GR* with a power law exponent of $p = i^*/(i^* + 2)$.

To determine the applicability of Equation 3.1 to our results for DIP on SiO_2, in Figure 3.2 we plot the island density as deduced by data such as those presented in Figure 3.1 as a function of the growth rate. These data include three

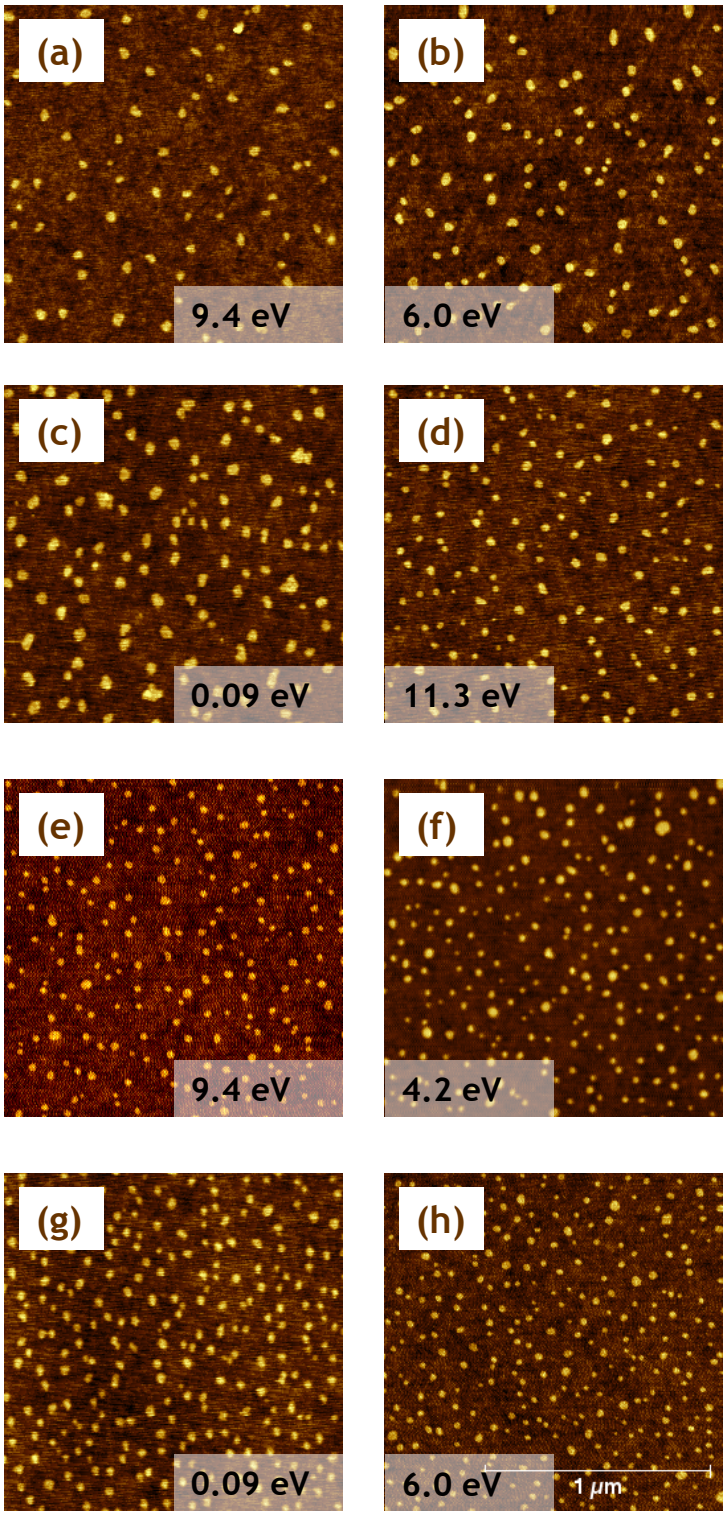

Figure 3.1: A series of 1.5 × 1.5 μm^2 AF micrographs of sub-monolayer DIP films grown on SiO_2. The incident kinetic energy is inset in each image. We note each image displays the same compact island morphology, and island density varies only with growth rate.

sets of conditions (all thermal energy) where the *GR* is within 10%, but the coverage differed by about a factor of 3. Accounting for changes in the *GR*, the change in coverage in these cases corresponded to changes in the island density of only a few %. Thus, the island densities represented in this figure are essentially N_{max}. As may be seen, the data for DIP on SiO_2 are described well by Equation 3.1 for both thermal (0.09 eV) and hyperthermal (4.2-11.3 eV) incident kinetic energies. The data span a range of over 2 orders of magnitude in *GR*, namely from 3.5×10^{-4} to 4.7×10^{-2} ML-s^{-1}. The experimental uncertainty in the measured values of island density can be determined using Poisson statistics. If N islands are counted in an AF micrograph, the uncertainty in this value is $N^{1/2}$. For each data point, the experimental uncertainty is between 3% and 6%. A fit to these data, using the known uncertainties as weights, gives a power law exponent of 0.456 ± 0.028, or a value for the critical nucleus of $i^* = 1.67 \pm 0.19$. As the experimental uncertanties in the data are small, the uncertainty in the calculated value of i^* is primarily a consequence of scatter in the data. Thus, these results indicate that a cluster of 3 DIP molecules (i.e., $i^* \sim 2$) represents a stable nucleus that will grow, and not decay.

3.4.2 Pentacene on SiO_2

We have also examined the submonolayer nucleation and growth of pentacene on SiO_2, both at thermal and hyperthermal incident kinetic energies. In Figure 3.3 we present a series of AF micrographs for the growth of pentacene on SiO_2 as a function of growth rate (*GR*). All experiments were conducted at T_s = 40°C, and each image represents an area of 4×4 μm^2. As in the case of DIP, the growth rate of pentacene has been tuned by varying the temperature of the

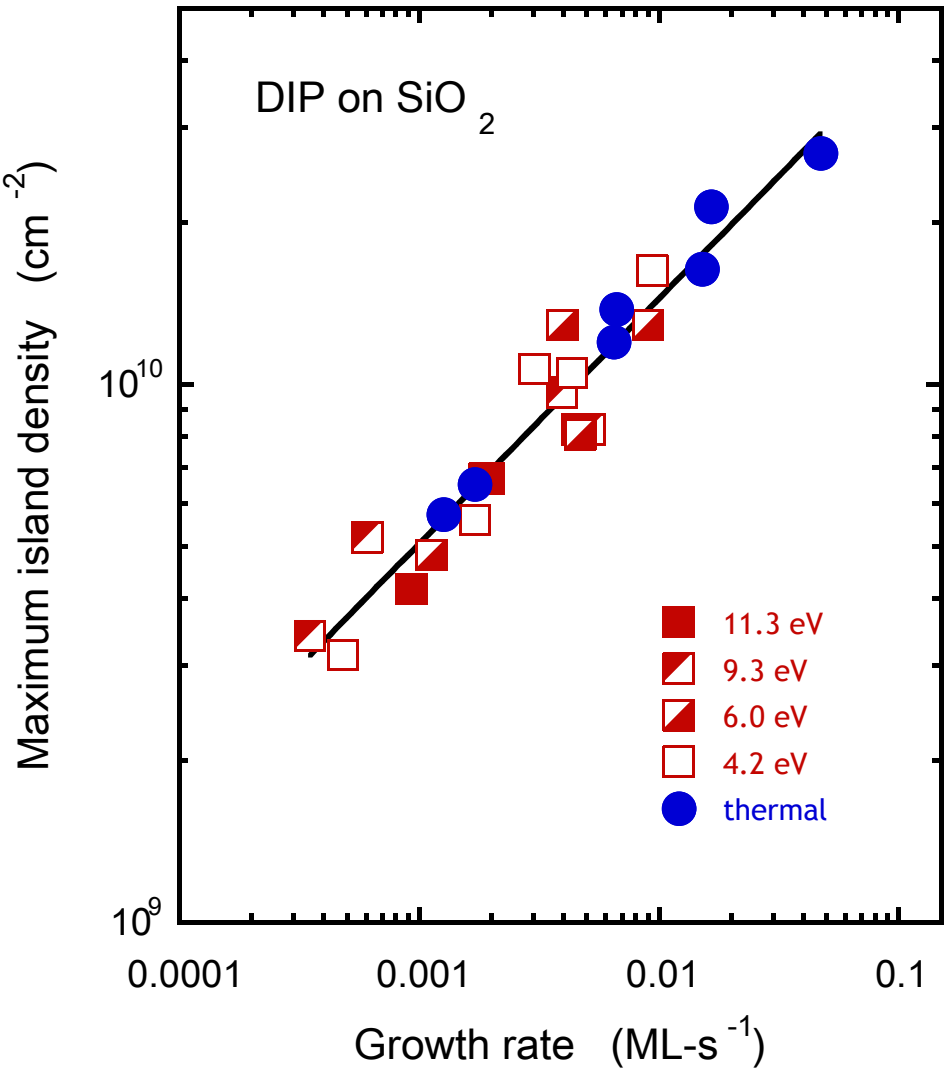

Figure 3.2: A plot of island density (as obtained from data such as those shown in Figure 3.1 as a function of growth rate for each incident kinetic energy studied. A fit of the data to the power law described by Equation 3.1 is shown as a solid line. From the power law fit, a critical cluster size of $i^* = 1.67 \pm 0.19$ is obtained.

in situ evaporator for both thermal and hyperthermal molecular beam sources. In all cases we observed single ML-tall high islands for these coverages ($0.084 < \theta < 0.255$). The relative uniformity of the size and spacing of islands is also consistent with homogeneous nucleation and 2D complete condensation. We take note of the island shapes that are formed with pentacene; the islands are irregular, less compact than those formed from DIP, similar to the shapes that many investigators have observed for pentacene on SiO_2 **[22,26-29,32-34]**. The micrographs plotted in Figure 3.3 represent growth at thermal incident kinetic energy, $E_i \sim 0.09$ eV [Fig. 3(a-c)], and at $E_i = 2.7$ [Fig. 3.3(f)], and 6.7 eV [Fig. 3.3(d,e)]. In Figure 3.3 we have encircled two (a,d), and three (b,e,f) sets of micrographs that represent growth at nearly identical growth rates, but different incident kinetic energies. Clearly, as the growth rate increases, the island density increases. Also, the effect of incident kinetic energy at a fixed growth rate is subtle at best.

In Figure 3.4 we plot the island density as deduced by data such as those presented in Figure 3.3 as a function of the growth rate. As may be seen, the data for pentacene on SiO_2 are described well by Equation 3.1 for both thermal (0.09 eV) and hyperthermal (2.7-6.7 eV) incident kinetic energies. We have observed such power law scaling concerning the nucleation of pentacene on SiO_2 using a supersonic source **[14]**, and by others using thermal effusion cell **[29]**, similar to what we also employ here. Our data for pentacene span a range of over an order of magnitude in GR, namely from 1.4×10^{-3} to 1.8×10^{-2} ML-s^{-1}. A fit to these data, including both thermal and hyperthermal incident kinetic energies, gives a power law exponent of 0.721 ± 0.079, or a value for the critical nucleus of $i^* = 5.18 \pm 2.04$. Perhaps most important, in terms of the absolute island density, excepting one outlier ($E_i = 0.09$ eV, $GR \sim 0.003$ ML-s^{-1}) where the measured is-

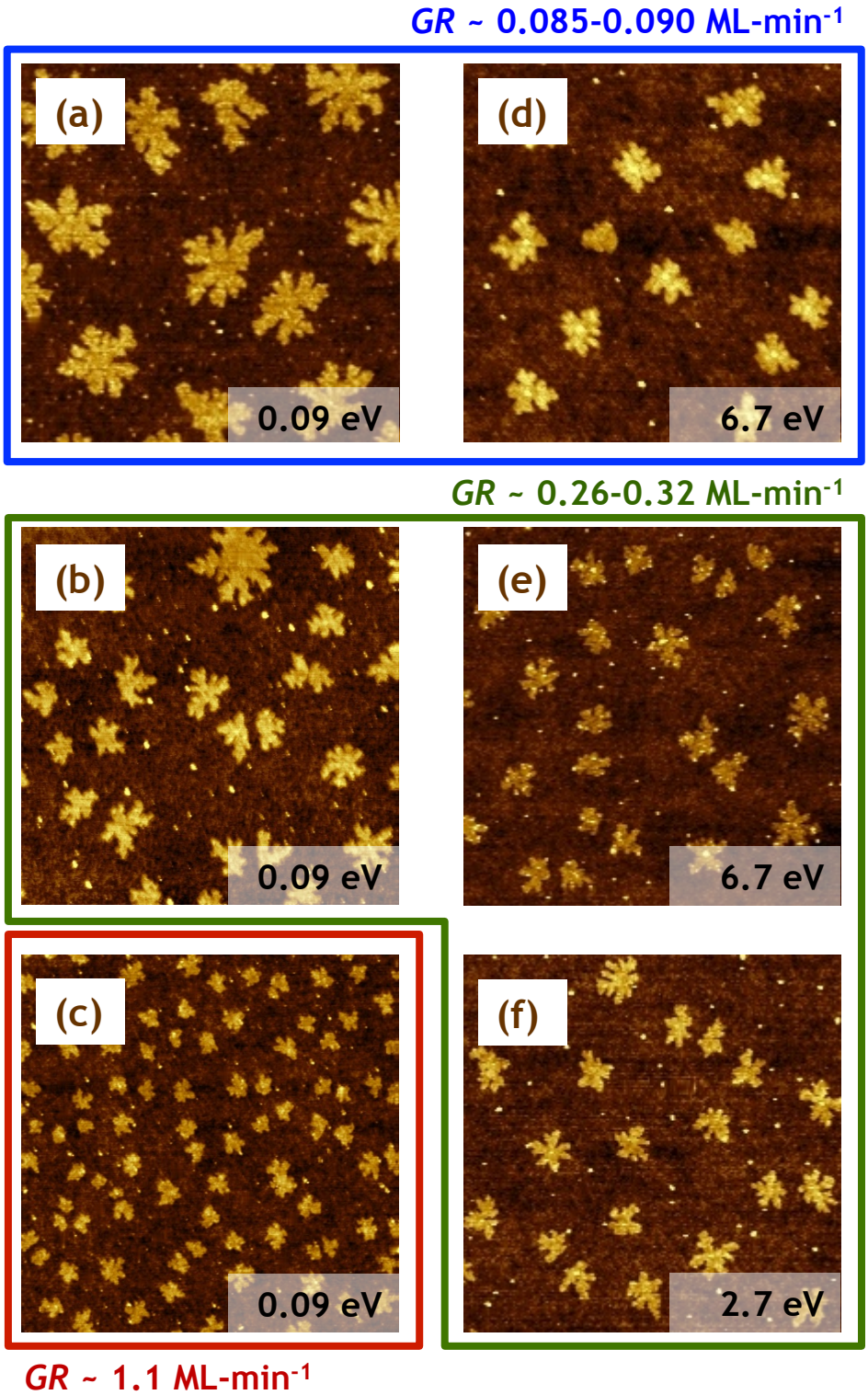

Figure 3.3: A series of 4×4 μm^2 AF micrographs of sub-monolayer pentacene films grown on SiO_2. The incident kinetic energy is inset in each image. Two (a,d), and three (b,e,f) sets of micrographs that represent growth at nearly identical growth rates, but different incident kinetic energies, have been highlighted. Changes in island density with growth rate are easily observed, while changes with incident kinetic energy are subtle at best.

land density exceed the fit by ~ 50%, at comparable rates of growth, the incident kinetic energy has no effect on the island density. In addition, from Figure 3.4 comparing islands that are formed at a comparable growth rate (0.0044-0.0053 ML-s^{-1}), but different values for E_i = (b) 0.09, (f) 2.7, and (e) 6.7 eV, we see that the shapes of the islands are also very similar.

3.5 Discussion

We have examined the nucleation of DIP on SiO_2, focusing on the variation of the island density with the rate of growth, and its possible dependence on the incident kinetic energy. As may be seen from the results presented in Figure 3.2), for DIP we find no evidence for the dependence of the island density on incident kinetic energy. To determine if this observation is specific to DIP, we also re-examined the nucleation of pentacene on SiO_2. As demonstrated by the data displayed in Figure 3.4, for this system we also found no compelling evidence for the dependence of the island density on incident kinetic energy. At this point it is useful to review the arguments that one could put forward involving the effect of incident kinetic energy on thin film growth, from the initial stages of nucleation to the formation a thin films consisting of several monolayers.

As indicated in section 3.2, the use of non-equilibrium approaches and/or energetic species to alter or manipulate thin film growth has been long recognized **[8]**. Plasma-based processes are ubiquitous in semiconductor manufacturing, but are in general unsuitable to the growth of small molecule organic thin films. Aerodynamic acceleration of organic small molecules via the use of supersonic molecular beams is potentially one method to introduce energetic

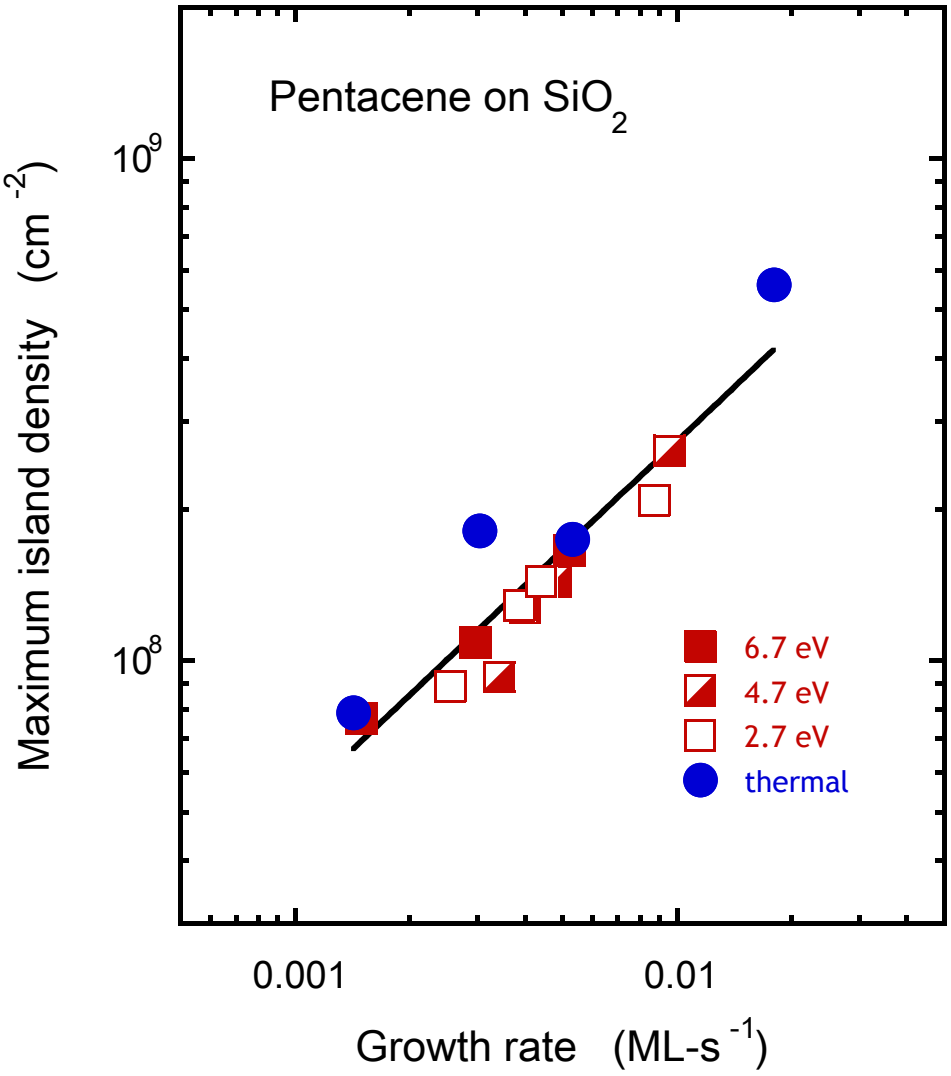

Figure 3.4: A plot of island density (as obtained from data such as those shown in Figure 3.3 as a function of growth rate for each incident kinetic energy studied. A fit of the data to the power law described by Equation 3.1 is shown as a solid line. From the power law fit, a critical cluster size of of $i^* = 5.18 \pm 2.04$ is obtained.

species in thin film growth. Concerning molecular scale events, computer simulation can provide some insight into which events may be most affected by the kinetic energy of the impinging molecules. Although there are a number of studies that have employed computer simulation to model the growth of small molecule organic thin films **[35]**, there are very few that have considered directly the effect of incident kinetic energy **[19,21,36,37]**. These studies have shown that the probability of adsorption, which obviously affects the growth rate, depends strongly on the incident kinetic energy **[14,18,21]**. With respect to processes not normally observed at thermal energies, at sufficiently high incident kinetic energies events such as insertion into a pre-existing layer can occur, although such events occur more readily at a step edge, and when the molecules axis is aligned with the surface normal. However, this same work has not shown a significant effect of the incident kinetic energy on the mobility of the adsorbed molecules, i.e., via what is often termed "transient mobility."

For the incident kinetic energy to have an effect on nucleation, the incident molecules must impact a molecular cluster whose size is comparable to the critical cluster size, and within a time frame for which they retain some "memory" of their incident trajectory. As we have shown, the critical nucleus sizes for both DIP and pentacene are on the order of a handful of molecules. It is instructive to consider the fraction of the surface that is covered by these critical nuclei before they grow into relatively large islands that we observe here at later stages of growth. For the sake of argument, we will assume that these small clusters may exist in a lying down form, before reorganizing at higher coverages to form islands consisting of the standing up form **[38]**. For DIP, 2 molecules in the unit cell **[39]** will project an area of $\sim 1.680 \times 0.855$ nm^2 or 1.44×10^{-14} cm^2. Using the highest rate of growth examined here (cf. Figure 3.2), we found $N_{max} \sim 2.69$

$\times 10^{10}$ cm^2. Combining these two values, we calculate that $\sim 0.039\%$ of the surface would be covered by these critical nuclei. It should be clear that essentially all of these islands will grow in the initial stages via capture of adsorbed DIP molecules diffusing on the surface and not by direct capture of DIP impacting on an existing island. Indeed, even after the islands consist of ~ 20 molecules, they will still only occupy at most $\sim 0.4\%$ of the surface, and will continue to grow by capturing diffusing adsorbed molecules.

The same arguments apply to the case of pentacene. If we use a cluster size of 6 molecules for pentacene, 3 unit cells could project an area as large as $\sim 3.54 \times 10^{-14}$ cm^2. Using the largest island density found here, 5.62×10^8 cm^2 (cf. Figure 3.4), and combining these two values, we calculate that 0.0020% of the surface would be covered by these critical nuclei. Thus, again, it should be clear that essentially all of these pentacene islands will grow in the initial stages via capture of adsorbed molecules diffusing on the surface, and not by direct capture of those impacting on an existing island. As islands continue to grow, both in the case of DIP and pentacene, they will be increasingly subjected to direct impact by the impinging molecules. Based on observations from molecular dynamics simulations, impinging molecules possessing kinetic energies on the order of 5-10 eV, can displace a molecule from a step-edge, or insert into the island itself, for example, but break-up of an island consisting of 10s of molecules into many smaller islands is not a plausible outcome. For incident kinetic energy to have an effect on nucleation, the critical island densities would have to be much, much larger than we have examined here (e.g., a factor of > 100), either by increasing the rate of growth by multiple orders of magnitude, or by decreasing the substrate temperature significantly.

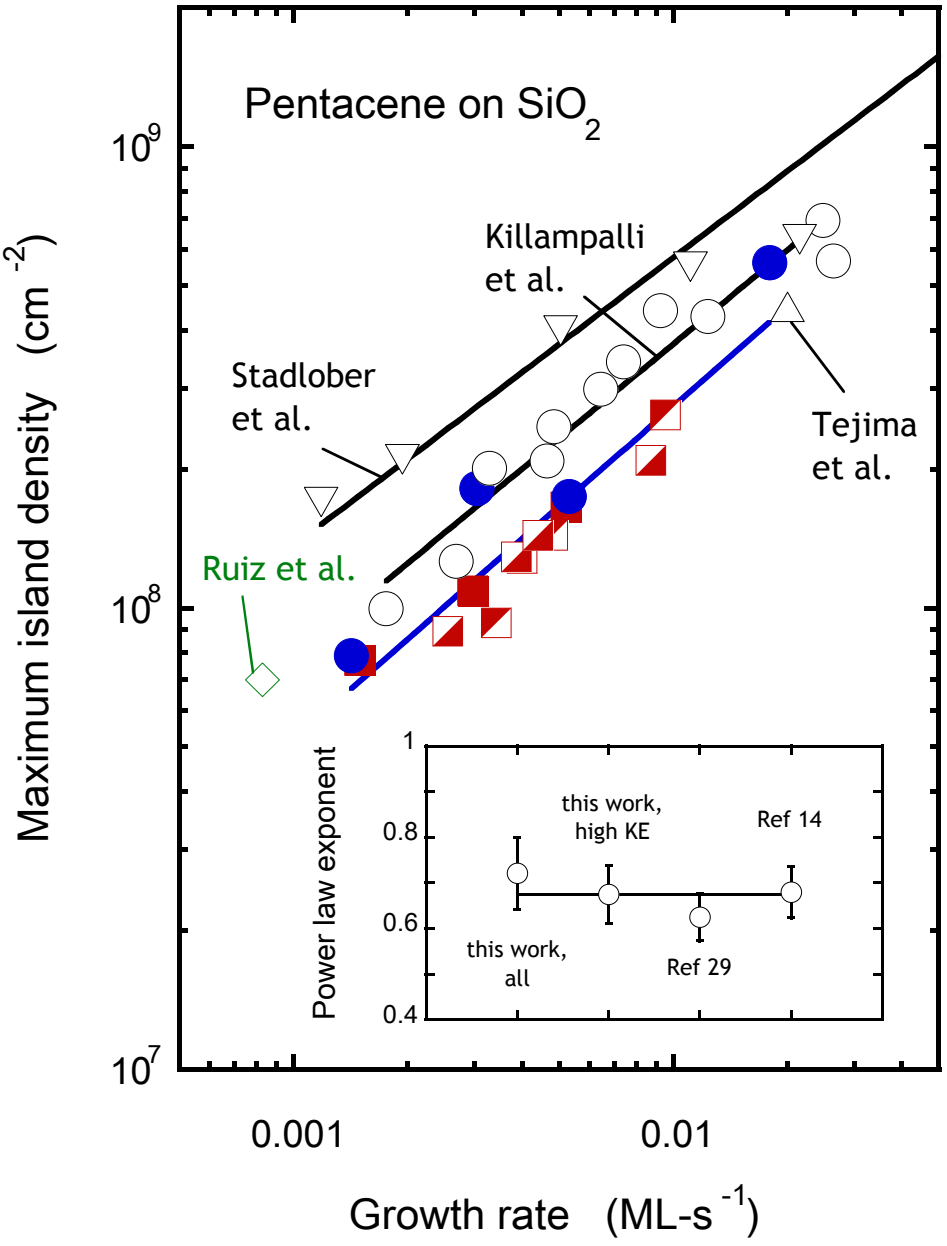

Figure 3.5: A plot comparing our data from Figure 3.4 and similar experimental data from Ruiz et al. **[27]**, Tejima et al. **[28]**, and Stadlober et al. **[29]**. Each data set can be fit to a power law using the same exponent (within statistical uncertainty.) The power law exponents for each data set are shown in the inset.

In Figure 3.5 we consider a comparison of several experimental examinations of the nucleation of pentacene on SiO2 at or near room temperature. Our results displayed in Figure 3.4 are presented, as are results from our previous work (using a different experimental system) **[14]**, and data from Ruiz et al. **[27]**, Tejima et al. **[28]**, and Stadlober et al. **[29]**. First, although most of these studies are conducted nominally at "room temperature", variations in experimental system design and configuration could result in substrate temperature differences of as much as 15 °C. Thus, offsets between data sets could merely reflect different substrate temperatures (e.g., our results here are for T_s = 40 °C, while Stadlober et al. cite T_s = 25 °C). Most importantly, in cases where the growth rate was varied **[14,29]**, we see that the variation of N_{max} with GR is very similar in all cases. All three data sets (this work, Killampalli et al. **[14]**, and Stadlober et al. **[29]**) fit well to a power law with essentially the same exponent within experimental uncertainties, where $p = 0.62 - 0.72$, as shown in the inset in Figure 3.5. We note that the work of Stadlober et al. **[29]** is perhaps the most extensive concerning an examination of the nucleation of pentacene using thermal energy sources. Their work is one of the few that used both an analysis of the island size distribution (ISD) and the power law analysis used here. Indeed, while analysis of the ISD can give an estimate for i^*, these authors chose to rely on the much more sensitive power law analysis to quote values for the size of the critical nucleus. As has been pointed out in a recent review **[40]**, while a single experiment can be sufficient to extract the critical nucleus size using an ISD (and the similar capture zone size distribution), this does not mean such methods are the most sensitive and accurate in estimates for i^*.

3.6 Conclusions

We have examined the growth of DIP on SiO_2 using *ex situ* AFM, focusing on the initial stages of growth at room temperature. We have employed both a conventional thermal effusive source, and a supersonic molecular beam to deliver DIP to the surface at incident kinetic energies E_i = 0.09-11.3 eV. We have found that the nucleation of DIP on SiO_2 occurs via homogeneous nucleation, consistent with 2D complete condensation. The islands that are formed in the coverage range examined ($\theta < 0.11$ ML) are compact, and exhibit no obvious faceting. Our results show absolutely no effect of the incident kinetic energy on the island density at a fixed growth rate. The maximum island density exhibits a power law dependence on the rate of growth, and the value of the exponent, $p = 0.456 \pm 0.028$, indicates a critical nucleus size of $i^* = 1.67 \pm 0.19$. These results indicate that a cluster of 3 DIP molecules (i.e., $i^* \sim 2$) represents a stable nucleus that will grow, and not decay.

We have also re-examined the growth of pentacene on SiO_2, focusing here on a direct comparison of the effect of incident kinetic energy on the island density and its dependence on the growth rate. As with DIP, and in agreement with previous work, both by our group **[14]** and by others **[27-29]**, the nucleation of pentacene on SiO_2 occurs via homogeneous nucleation, consistent with 2D complete condensation. The preponderance of evidence shows no effect of the incident kinetic energy on either the island density or the shape at a fixed growth rate. Scaling of the island density with the growth rate indicates a critical nucleus size of $i^* = 5 \pm 2$, consistent with previous work. By considering plausible molecular scale events that might occur when a molecule possessing high incident kinetic energy strikes an island consisting of 10s of molecules **[19,21,36,37]**,

and factoring in the density of these islands and the growth rate, it is easy to understand why we observe no effect of incident kinetic energy on the island density for either DIP or pentacene.

3.7 References

1. Forrest, S. R. *Nature*, **2004**, *428*, 911-918.
2. Kowarik, S.; Gerlach A.; Schreiber, F. *J. Phys. Condens. Matter*, **2008**, *18*, 184005.
3. Dimitrakopoulos, C. D.; Malenfant, P. R. L. *Adv. Mater.*, **2002**, *14*, 99.
4. Lucas, B.; Trigaud, T.; Videlot-Ackermann, C. *Polymer International*, **2012**, *61*, 374-389.
5. Dodabalapur, A.; Torsi, L.; Katz, H. E. *Science*, **1995**, *268*, 270-271.
6. Katz, H. E. *Chem. Mater.*, **2004**, *16*, 4748-4756.
7. Ling, M. M.; Bao, Z. N. *Chem. Mater.*, **2004**, *16*, 4824-4840.
8. Smith, D. L. *Thin-Film Deposition: Principles and Practice* McGraw Hill Professional, **1995**.
9. Xia, L-Q.; Jones, M. E.; Maity, N.; Engstrom, J. R. *J. Vac. Sci. Technol. A*, **1995**, *13*, 2651-2664.
10. Roadman, S. E.; Maity, N.; Carter, J. N.; Engstrom, J. R. *J. Vac. Sci. Technol. A*, **1998**, *16*, 3423-3433.
11. Casalis, L.; Danisman, M. F.; Nickel, B.; Bracco, G.; Toccoli, T. ; Iannotta, S.; Scoles, G. *Phys. Rev. Lett.*, **2003**, *90*, 20.
12. Danisman, M. F.; Casalis, L.; Scoles, G. *Phys. Rev. B*, **2005**, *72*, 085404.

13. Wu, Y.; Toccoli, T.; Koch, N.; Iacob, E.; Pallaoro, A.; Rudolf, P.; Iannotta, S. *Phys Rev. Lett.*, **2007**, *98*,076601.

14. Killampalli, A. S.; Schroeder, T. W.; Engstrom, J. R. *Appl. Phys. Lett.*, **2005**, *87*, 033110.

15. Killampalli, A. S.; Engstrom, J. R. *Appl. Phys. Lett.*, **2006**, *88*, 143125.

16. Hong, S.; Amassian, A.; Woll, A. R.; Bhargava, S.; Ferguson, J. D.; Malliaras, G. G.; Brock, J. D.; Engstrom, J. R. *Appl. Phys. Lett.*, **2008**, *92*, 25.

17. Amassian, A.; Pozdin, V.; Desai, T. V.; Hong, S.; Woll, A. R.; Ferguson, J. D.; Brock, J. D.; Malliarias, G. G.; Engstrom, J. R. *J. Mater. Chem.*, **2009**, *19*, 5580-5592.

18. Amassian, A.; Desai, T. V.; Kowarik, S.; Hong, S.; Woll, A. R.; Malliaras, G. G.; Schreiber, F.; Engstrom, J. R. *J. Chem. Phys.*, **2009**, *130*, 124701.

19. Goose, J. E.; Killampalli, A. S.; Clancy, P.; Engstrom, J. R. *J. Phys. Chem.*, **2009**, *113*, 6068-6073.

20. Desai, T. V.; Woll, A. R.; Schreiber, F.; Engstrom, J. R. *J. Phys. Chem. C*, **2010**, *114*, 20120-20129.

21. Desai, T. V.; Hong, S.; Woll, A. R.; Hughes, K. J.; Kaushik, A. P.; Clancy, P.; Engstrom, J.R. *J. Chem. Phys.*, **2011**, *134*, 224702.

22. Woll, A. R.; Desai T. V.; Engstrom, J. R. *Phys. Rev. B*, **2011**, *84*, 075479.

23. Desai, T. V.; Kish, E. R.; Woll, A. R.; Engstrom, J. R. *J. Phys. Chem. C*, **2011**, *115*, 18221-18234.

24. Desai, T. V.; Woll, A. R.; Engstrom, J. R. *J. Phys. Chem. C*, **2012**, *116*, 12541-12552.

25. Venables, J. A.; Spiller, G. D. T.; Hanbucken, M. *Rep. Prog. Phys.*, **1984**, *47*, 399-459.

26. Ruiz, R.; Nickel, B.; Koch; N; Feldman, L. C.; Haglund, R. F.; Kahn, A.; Scoles, G. *Phys. Rev. B*, **2003**, *67*, 125406.

27. Ruiz, R.; Nickel, B.; Koch; N; Feldman, L. C.; Haglund, R. F.; Kahn, A.; Family, F.; Scoles, G. *Phys. Rev. Lett.*, **2003**, *91*, 136102.

28. Tejima, M.; Kita, K.; Kyuno, K.; Toriumi, A. *Appl. Phys. Lett.*, 2004, *85*, 3746-3748.

29. Stadlober, B.; Haas, U.; Maresch, H.; Haase, A. *Phys. Rev. B*, **2006**, *74*, 165302.

30. Schroeder, T. W. *Cornell University: PhD Thesis* **2004**.

31. Desai, T. V. *Cornell University: PhD Thesis* **2011**.

32. Meyer zu Heringdorf, F.-J.; Reuter, M. C.; Tromp, R. M. *Appl. Phys. A*, **2004**, *78*, 787.

33. Pratontep, S.; Brinkmann, M.; Nuesch, F.; Zuppiroli, L.; *Phys. Rev. B*, *2004*, *69*, 165201.

34. Pratontep, S.; Nuesch, F.; Zuppiroli, L.; Brinkmann, M. *Phys. Rev. B*, **2005**, *72*, 085211.

35. Clancy, P. *Chem. Mater.*, **2011**, *23*, 522.

36. Goose, J. E.; Clancy, P. *J. Phys. Chem. C*, *2007*, *111*, 15653.

37. Kaushik, A. P.; Clancy, P. *Surface Sci.*, *2011*, *605*, 1185.

38. Choudhary, D.; Clancy, P.; Shetty, R.; Escobedo, F. *Adv. Funct. Mater.*, **2006**, *16*, 1768.

39. Heinrich, M. A.; Pflaum, J.; Tripathi, A. K.; Frey, W.; Steigerwald, M. L.; Siegrist, T. J. *Phys. Chem. C*, **2007**, *111*, 18878.

40. Hlawacek G.; Teichert, C. *J. Phys: Condens. Matter*, **2013**, *25*, 143202.

CHAPTER 4

SUPERSONIC MOLECULAR BEAM STUDIES OF PERYLENE DERIVATIVES ON SELF-ASSEMBLED MONOLAYERS: TRAPPING, ADSORPTION AND ROUGHNESS EVOLUTION

4.1 Overview

We have examined the growth, and dynamics of the adsorption of N,N-dipentylperylene-3,4,9,10-tetracarboxylic diimide (PTCDI-C_5) and N,N-dioctcylperylene-3,4,9,10-tetracarboxylic diimide (PTCDI-C_8) on SiO_2 surfaces modified by self-assembled monolayers (SAMs) using *in situ* synchrotron x-ray scattering and *ex situ* atomic force microscopy. From real-time x-ray scattering, we find that both PTCDI-C_5 and PTCDI-C_8 exhibit prolonged layer-by-layer growth for approximately the first ten monolayers of deposition on all three SAMs examined. Concerning adsorption on the pristine SAM-terminated surfaces, in all cases, we observe a smooth decrease in the probability of adsorption with increasing incident kinetic energy, indicative of trapping-mediated adsorption. Once these surfaces are covered by PTCDI-C_5 or PTCDI-C_8, the probability of adsorption no longer depends on the identity of the SAM, but still exhibits a significant decrease with increasing incident kinetic energy. The adsorption probability of each PTCDI molecule on itself is similar to that observed on two SAMs that possess aromatic end groups, but it differs significantly from that observed on a relatively short, methyl-terminated SAM. These differences could reflect mechanisms, such as direct molecular insertion of incident molecules into either the existing thin film or the longer chain SAMs, or possibly the effects of greater internal degrees of freedom of the near surface layers in these cases.

4.2 Introduction

Complex conjugated molecules which can form highly ordered thin films at relatively low temperatures have received much attention in recent years for applications in organic thin film electronics and photonics **[1-3]**. Important for the development of organic photovoltaic devices is the integration of both *p*-type and *n*-type molecules in the same device microstructure. Previous studies have shown that deposition of organic semiconductors on surfaces modified with self-assembled monolayers (SAMs) can result in films with improved electrical properties **[4-8]**. However, the basic mechanisms of crystal growth are not completely understood, particularly the interactions between molecules and surfaces terminated with SAMs, and how these interactions affect film growth.

A class of molecules attracting significant interest are derivatives of perylene, such as N,N-ditridecylperylene-3,4,9,10-tetracarboxylic diimide (PTCDI-C_{13}), N,N-dioctcylperylene-3,4,9,10-tetracarboxylic diimide (PTCDI-C_8), and N,N-dipentylperylene-3,4,9,10-tetracarboxylic diimide (PTCDI-C_5). These are *n*-type organic semiconductors and have been used to fabricate devices such as OTFTs and photovoltaics **[9-15]**. These molecules have been shown to form well ordered thin films with relatively high electron mobilities.

Here we report on the effects of self-assembled monolayers on the thin film growth of PTCDI-C_5 and PTCDI-C_8, concentrating on the dynamics of adsorption using a combination of both *in situ* and *ex situ* surface sensitive techniques. The structures of these two molecules are shown in Figure 4.1. The focus is to develop a better understanding of the interactions between molecules of PTCDI-C_5 and PTCDI-C_8 and surfaces terminated with SAMs

and their effect on film growth. Concerning the SAMs, we consider three layers that differ in terms of their thickness and chemical nature, namely 1-napthylmethyltrichlorosilane (NMTS), 6-phenylhexyltrichlorosilane (PHTS), and hexamethyldisilazane (HMDS).

We deposit thin films of PTCDI-C_5 and PTCDI-C_8 in ultrahigh vacuum (UHV) with a collimated supersonic molecular beam source **[16-18]** and as with our previous studies **[19-21]**, we use *in situ* real time synchrotron x-ray scattering to monitor the dynamics of adsorption and growth from the submonolayer to the multilayer regime. We show that both PTCDI-C_5 and PTCDI-C_8 exhibit prolonged layer-by-layer growth on all surfaces examined here.

4.3 Experimental Procedures

The experiments that were conducted *in situ* and in real-time were carried out in a custom-designed UHV chamber that has been described in detail elsewhere **[17]** in the G3 station of the Cornell High Energy Synchrotron Source (CHESS). Briefly, the system consists of four separately pumped chambers: a main scattering chamber, a source and antechamber, which act to produce the supersonic beam, and a fast entry load-lock. All chambers are pumped by high-throughput turbomolecular pumps. The base pressure of the chamber was typically $\sim 4 \times 10^{-9}$ Torr and samples were loaded via the load-lock chamber, which was evacuated to $\sim 10^{-7}$ Torr prior to sample transfer into the main chamber.

Supersonic molecular beams of PTCDI-C_5 and PTCDI-C_8 (99.8% Sigma-Aldrich Corp.) were generated by passing a carrier gas (He, 99.999%) through a temperature-controlled container (the evaporator) containing these species lo-

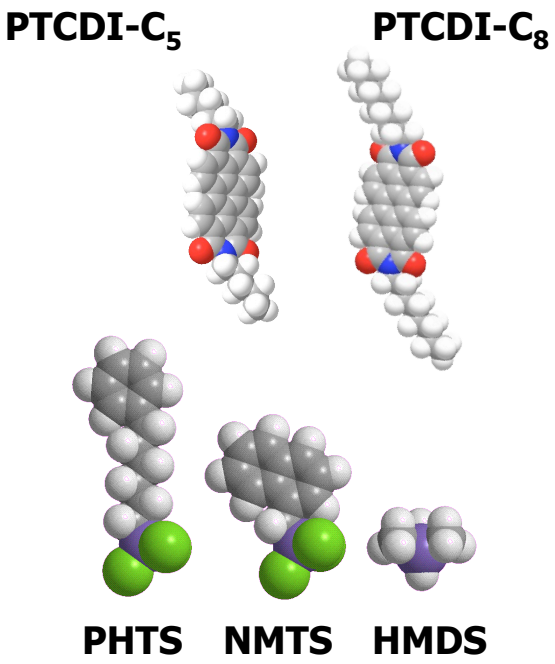

Figure 4.1: Space filling models of the molecules studied here. PTCDI-C_5 and PTCDI-C_8, and three self-assembled monolayers: HMDS, NMTS and PHTS. Hydrogen atoms in white, carbon in gray, silicon in purple, chlorine in green, oxygen in red and nitrogen in blue.

cated upstream of the nozzle (150 μm orifice). The doubly differentially pumped beam passed through a trumpet shaped skimmer into an antechamber and through an aperture that produced a well-defined beam spot on the substrate surface. The mean kinetic energy of the molecules in the supersonic molecular beam can be controlled by adjusting the flow rate of the carrier gas. The mean kinetic energy of PTCDI-C_5 and PTCDI-C_8 in these beams is estimated from physical properties and time-of-flight measurements of similar molecules **[17, 22, 23]**. By assuming the same velocity of each molecule for a given nozzle pressure, since the kinetic energy of PTCDI-C_{13} as a function of nozzle pressure is known, kinetic energies for PTCDI-C_5 and PTCDI-C_8 can be estimated based on this known velocity and molecular weight (cf. Section 2.2.4). Comparing the estimated value of kinetic energy (4.43 eV) to a successful time-of-flight measurement of PTCDI-C_5 (4.2 eV), we are confident that this estimation provides reasonable values for incident kinetic energy of PTCDI-C_5 and PTCDI-C_8.

Substrates were Si (100) wafers (Wacker-Siltronic, *p*-type, 100 mm dia., 500-550 μm thick, 38-63 Ω-cm) subject to a SC-1 clean, a 15 s HF dip, and a SC-2 clean immediately before the growth of approximately 300-nm-thick SiO_2 films by wet thermal oxidation at 1100°C. Next, these wafers were cleaned and degreased by sonication in anhydrous $CHCl_3$ solution (99%+), sonicated in deionized (DI) water, washed with DI water, dried with N_2, and exposed to UV-ozone for 15 min. These processes provided a clean and reproducible hydrophilic surface for the deposition of self-assembled monolayers. Using established procedures **[21, 24]** HMDS was deposited from the vapor phase using a YES LP-III Vapor Prime Oven while NMTS and PHTS (both Gelest Inc., Morrisville, PA) were deposited from the solution phase in a N_2-purged glove box.

	HMDS	**NMTS**	**PHTS**
Contact Angle (H_2O/formamide)	70°/60°	81°/61°	83°/69°
Surface Energy (mJ/m^{-2})	32.7	32.5	33.4
Thickness XRR (Å)		8.13 ± 0.01	10.98 ± 0.05
Molecular Length (Å)		7.11	11.68
Electron Density (Å^{-3})		0.39 ± 0.02	0.33 ± 0.01
Density of SAM (nm^{-2})	2.3 ± 0.5	4.22 ± 0.05	4.05 ± 0.09

Table 4.1: Properties of Self-Assembled Monolayers.

The SiO_2 substrates modified with NMTS, PHTS and HMDS, were characterized in a previous work by this group via contact angle and XRR **[21]**. To verify that the same process produced uniform SAM layers, contact angles were measured with two solvents (water and formamide) and compared to prior measurements on surfaces terminated with NMTS, PHTS and HMDS. Details concerning the properties of the SAMs are given in Table 4.1, reproduced from **[21]**.

Time-resolved and *in situ* measurements of the scattered x-ray synchrotron intensity were made using a silicon avalanche photodiode detector (APD, Oxford Danfysik, Oxford, UK). During PTCDI-C_n thin film growth the intensity was monitored at the anti-Bragg position ($q_z = q_{Bragg}/2$), which is an effective monitor of the nature of growth, i.e., layer-by-layer (LbL) vs. 3D islanded growth **[25]**. Following deposition and x-ray analysis, the samples were removed for *ex situ* analysis using atomic force microscopy (AFM), conducted in tapping mode using a DI 3100 Dimension microscope.

The x-ray data at the anti-Bragg position was fitted using a modified version **[19,26]** of the mean-field rate equation model of growth first proposed by Cohen and co-workers **[27]**. Briefly, the equations for the coverage of individual layers

(θ_n) are given by:

$$\frac{d\theta_n}{dt} = S_{n-1}F[(\theta_{n-1} - \theta_n) - \alpha_{n-1}(\theta_{n-1} - \theta_n)] + S_nF\alpha_n(\theta_n - \theta_{n+1}) \tag{4.1}$$

where $n = 0$ represents the substrate, $n = 1$ the first molecular layer, etc., S_n is the probability of adsorption for molecules incident on the n^{th} layer, F is the incident molecular flux (ML-s^{-1}), and θ_n is the fraction of molecules that after initially impacting and landing on top of the n^{th} layer, then drop down and become part of the n^{th} layer via some mechanism (e.g. overcoming the Ehrlich-Schwoebel barrier at a step edge). In this model we also assume that there are two values for the probability of adsorption: one for adsorption on the substrate (S_0), and one for that on previously existing molecular layers, independent of their thickness ($S_1 = S_2 = S_3$).

Once layer coverages have been calculated by integrating Equation 4.1, these can then be used to calculate the scattered x-ray intensity as a function of time **[19,25-27]**. The intensity of the scattered beam (I) depends upon the layer population, $\theta_n(t)$, according to the following relationship:

$$I(t) = \left| r_{subs}e^{-i\phi} + r_{film}\sum_{n=1}^{\infty}\theta_n(t)e^{-iq_zdn} \right|^2 \tag{4.2}$$

where r_{subs} and r_{film} are the scattering amplitudes of the substrate and the film, ϕ is the phase change upon reflection, q_z is the out-of-plane scattering vector and d is the out-of-plane interplanar spacing. At the anti-Bragg position, $q_zd = \pi$, which results in a change in the sign of the thin film terms in the summation. If each layer fills sequentially, such as in perfect LbL growth, an oscillation in the intensity results.

4.4 Results and Discussion

4.4.1 Morphology and X-ray Reflectivity of Multilayers of PTCDI-C_5 and PTCDI-C_8

In Figure 4.2, we display AF micrographs of multilayer thin films of PTCDI-C_5 and PTCDI-C_8, nominally 12 ML thick, deposited on a self-assembled monolayer of HMDS at 4.2 eV (PTCDI-C_5) and 5.1 eV (PTCDI-C_8) incident kinetic energy. As can be seen from the images, both films present smooth areas where single monolayer high steps can be seen. In contrast to previous studies of PTCDI-C_{13}, no large protrusions are observed. Similar morphologies are observed for both PTCDI-C_8 and PTCDI-C_5 deposited on other SAMs at similar conditions of growth. The PTCDI-C_5 exhibits an RMS roughness of ~1.05 nm, while the PTCDI-C_8 film exhibits an RMS of 1.43 nm.

In Figures 4.3 and 4.4, we display corresponding specular x-ray reflectivity data for PTCDI-C_5 on NMTS and PTCDI-C_8 deposited on HMDS. The scattered intensity exhibits Bragg reflections (up to second order for PTCDI-C_5 and third order for PTCDI-C_8) . The data for PTCDI-C_8 show well defined Laue oscillations that are characteristic of a well ordered lamellar structure and their spacing implies a coherent film thickness of about 7.8 ML. The PTCDI-C_5 data show less intense Laue oscillations, their spacing suggest a coherent film thickness of 4.5 ML. Similar specular x-ray reflectivity profiles were observed for PTCDI-C_5 and PTCDI-C_8 films grown on all surfaces examined here. For PTCDI-C_5 we calculate an average d_{001} spacing of 18.1 ± 0.2 Å, and for PTCDI-C_8 a $d_{(001)}$ spacing of 20.7 ± 0.2 Å, both similar to other reported studies **[13,28]**.

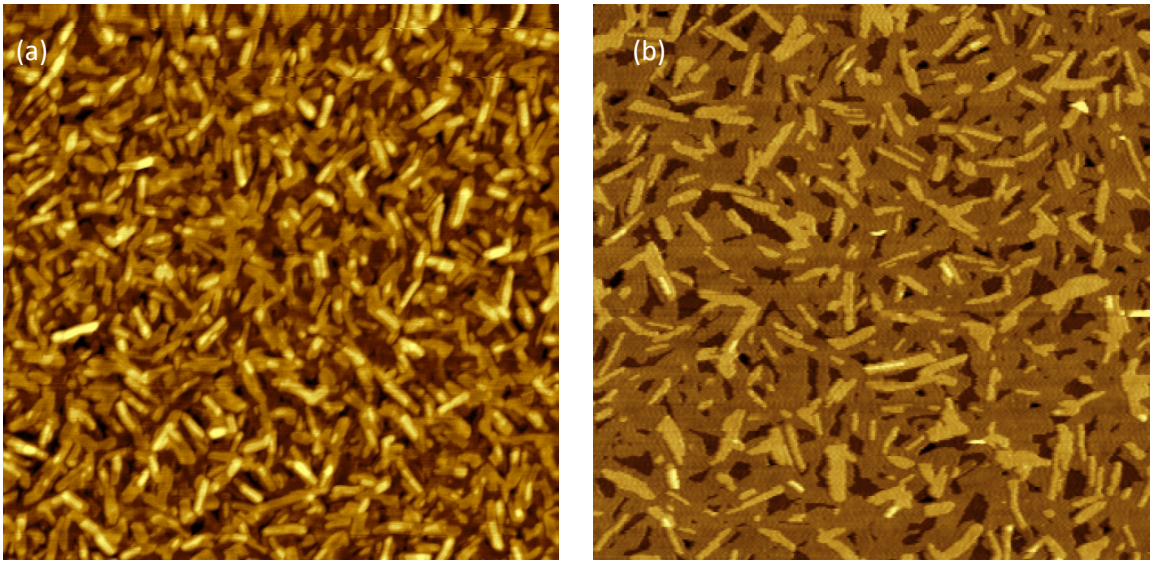

Figure 4.2: 3 × 3 μm AF micrograph of thin films of (a) PTCDI-C_5 (12.2 ML thick) and (b) PTCDI-C_8 (11.8 ML thick) deposited on SiO_2 substrates modified with HMDS.

4.4.2 Adsorption and Growth on SAMs

In Figures 4.5- 4.10, we present a subset of experiments we have conducted concerning the growth of PTCDI-C_5 and PTCDI-C_8 on HMDS, NMTS and PHTS. The data shown represent the lowest and highest kinetic energies examined here using the supersonic molecular beam source. All experiments were carried out with the substrate temperature T_s = 40 °C. Conducting growth experiments at room temperature minimizes any potential degradation of the SAM or desorption of deposited PTCDI-C_5 or PTCDI-C_8 molecules. As explained in greater detail in our previous work **[18-20]**, the intensity oscillations at the anti-Bragg condition, observed on all of the surfaces studied here, are expected for layer-by-layer growth due to the alternating contributions of the odd and even layers to the magnitude of the scattered intensity (cf. Equation 4.1). As may be seen in Figures 4.5- 4.10, the shape of the oscillations varies slightly depending on the

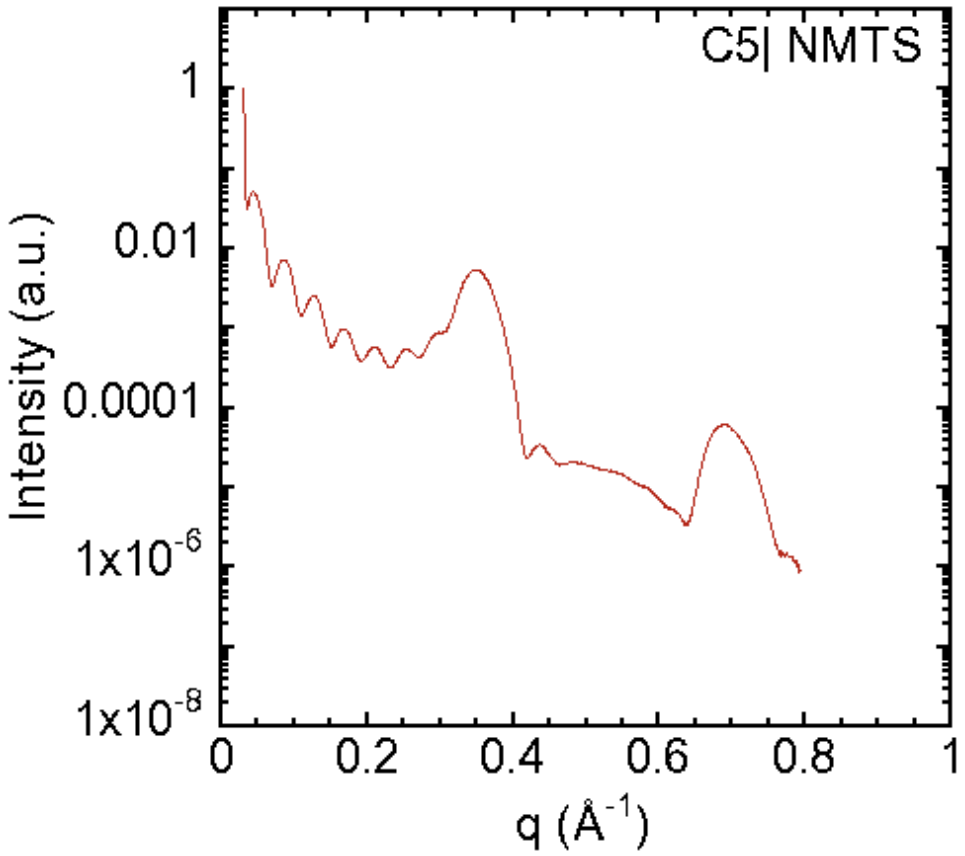

Figure 4.3: Specular x-ray reflectivity (XRR) of a 12 ML PTCDI-C_5 film deposited on NMTS.

nature of the starting surface and the molecule being deposited. Differences in relative intensities at $t = 0$, at the peak of the first oscillation (~1 ML coverage) and the saturation intensity as $t \rightarrow \infty$ can be understood as resulting from differences in the phase (ϕ) and reflection amplitudes (r_{subs} and r_{film}) that appear in Equation 4.2, which are functions of the thickness and electron density of the SAM or interfacial organic layer (IOL) **[19,20,25,26]**.

Figure 4.5 shows the growth of PTCDI-C_5 and Figure 4.6 shows the growth of PTCDI-C_8 on HMDS. In Figure 4.5(a) we present the scattered x-ray intensity acquired in real time at the anti-Bragg condition for the growth of PTCDI-C_5 on

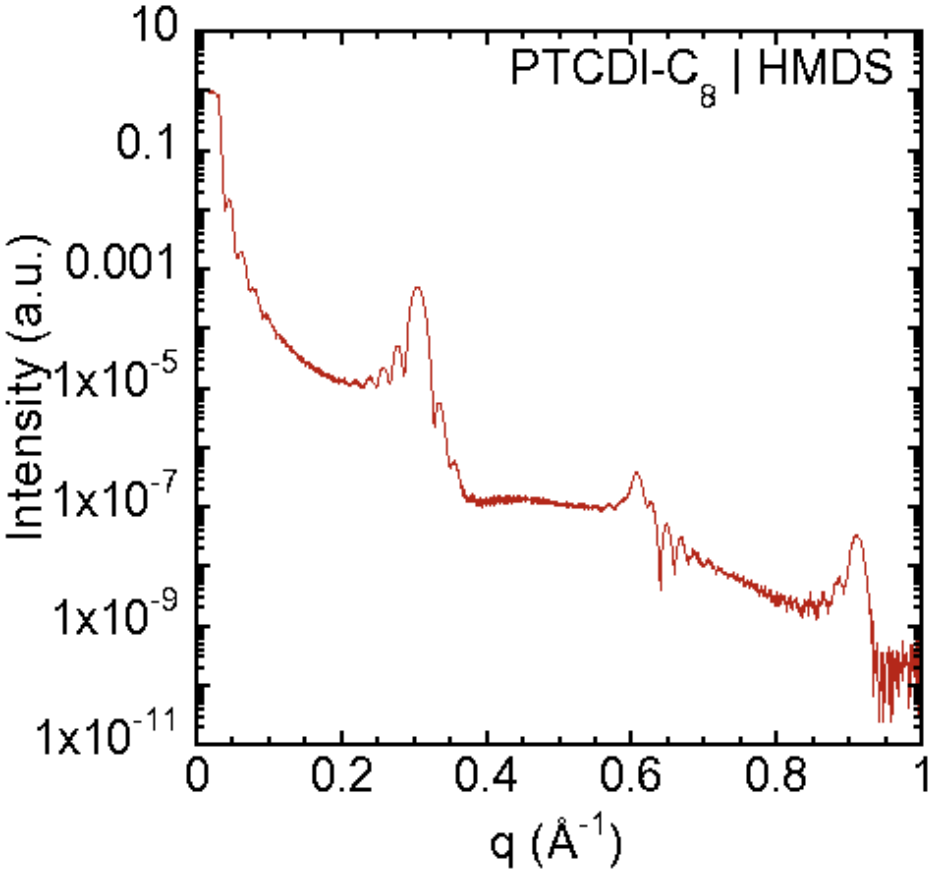

Figure 4.4: Specular x-ray reflectivity (XRR) of the 12 ML PTCDI-C_8 film deposited on HMDS, shown in Figure 4.2

HMDS at E_i = 4.2 eV, and in Figure 4.6(a), the growth of PTCDI-C_8 on HMDS at E_i = 5.1 eV. In a typical case, when roughness increases slowly, one expects the oscillations to repeat every 2 MLs, with a sharp, cusp-like maximum after the completion of each monolayer, separated by smooth, nearly parabolic minima. In some cases, the amplitudes associated with the completion of odd and even layers can vary greatly, and the cusp-like maxima may be obscured. For growth of both PTCDI-C_5 and PTCDI-C_8 on HMDS, we observe strong cusp-like maxima upon the completion of 2, 4, 6 and 8 MLs. Smaller cusp-like maxima can be seen upon completion of 1 and 3 MLs, though they are obscured at 5 and 7 MLs. The observation of intensity oscillations at coverages as high as 8 to 10 MLs is

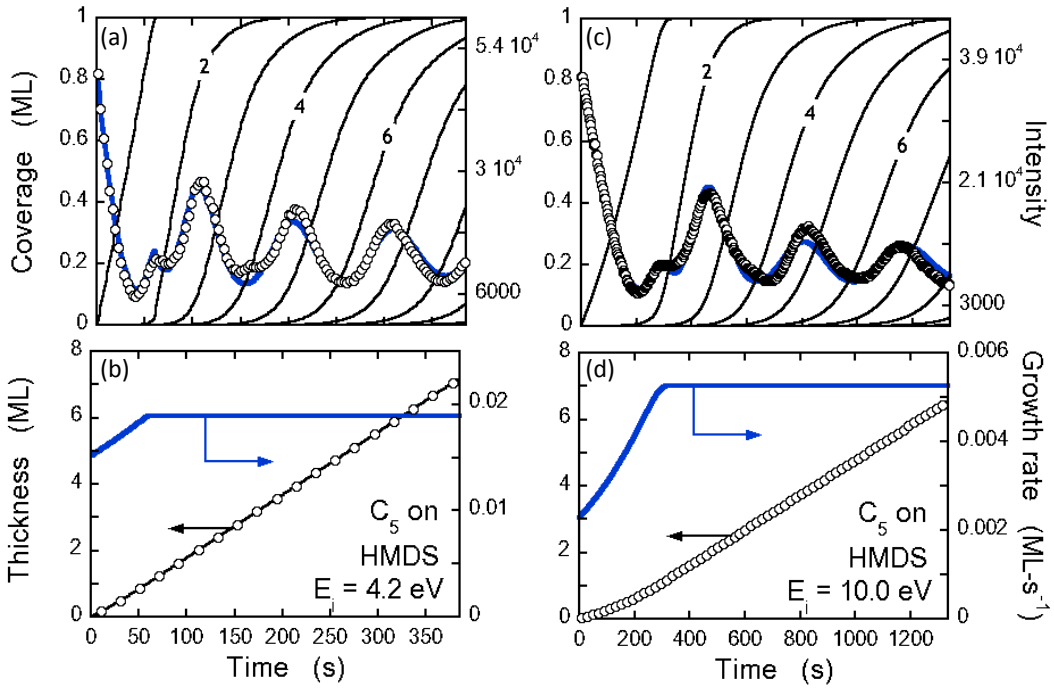

Figure 4.5: (a) X-ray intensity at the anti-Brag condition as a function of exposure to the molecular beam (E_i = 4.2 eV) for thin films of PTCDI-C_5 deposited on SiO_2 modified with HMDS. T_s = 40°C. Thick solid lines (right ordinate) indicate a fit of the data to a model, and thin solid curves (left ordinate) represent predicted coverages (θ_n) of the individual layers. (b) Total coverage (θ_{tot}, left ordinate) and growth rate (right ordinate) predicted by a fit of the data displayed in (a). These figures are repeated in (c) and (d), for PTCDI-C_5 incident at the higher incident kinetic energy (E_i = 10.0 eV) for this same surface.

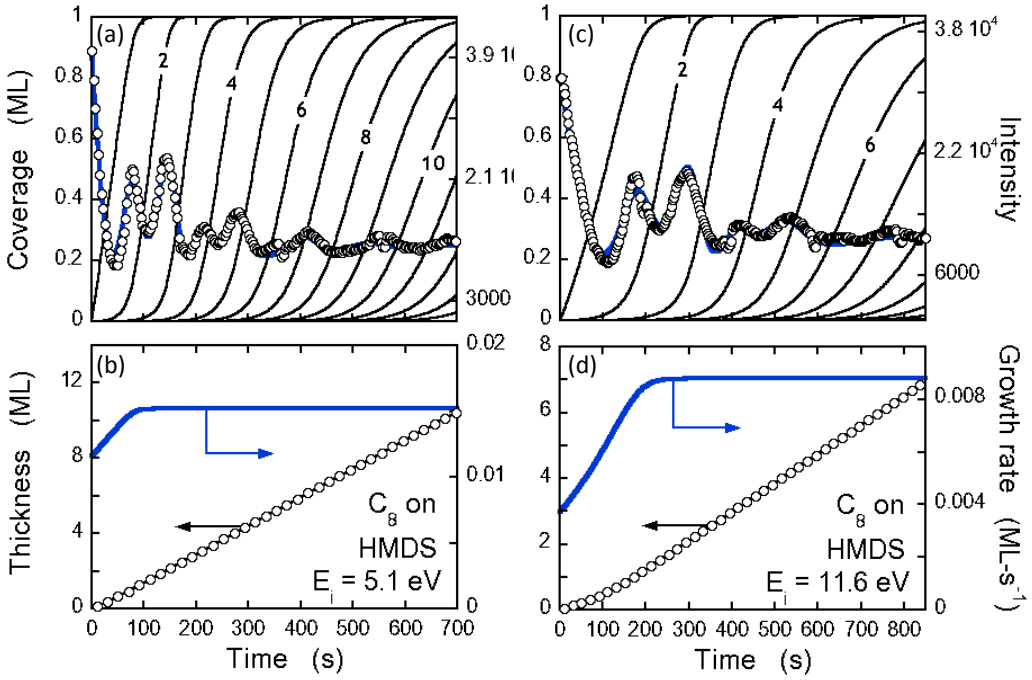

Figure 4.6: (a) X-ray intensity at the anti-Brag condition as a function of exposure to the molecular beam (E_i = 5.1 eV) for thin films of PTCDI-C_8 deposited on SiO_2 modified with HMDS. T_s = 40°C. Thick solid lines (right ordinate) indicate a fit of the data to a model, and thin solid curves (left ordinate) represent predicted coverages (θ_n) of the individual layers. (b) Total coverage (θ_{tot}, left ordinate) and growth rate (right ordinate) predicted by a fit of the data displayed in (a). These figures are repeated in (c) and (d), for PTCDI-C_8 incident at the higher incident kinetic energy (E_i = 11.6 eV) for this same surface.

significant and indicates both PTCDI-C_5 and PTCDI-C_8 grow in a layer-by-layer (LbL) mode for several monolayers.

The kinetics of growth can be modeled more precisely using equations 4.1 and 4.2, and these results are also shown in Figures 4.5(a,b) and 4.6(a,b). In (a) we show the coverage of each layer (solid black curves) predicted by the fit to the intensity oscillations (solid blue line). We find that to fit the data we need to assume that $S_0F \sim 0.01519$ ML-s^{-1} , whereas $S_{n\geq 1}F \sim 0.01896$ ML-s^{-1}. These data imply that the rate of growth has accelerated modestly with increasing PTCDI-C_5 coverage. Similarly, for PTCDI-C_8 growth we find $S_0F \sim 0.01162$ML-s^{-1}, whereas $S_{n\geq 1}F \sim 0.01518$ ML-s^{-1}, also indicating a modest increase in growth rate with increasing PTCDI-C_8 coverage. On the basis of behavior of molecules of similar aromatic structure and molecular weight (e.g. pentacene, diindenoperylene, and PTCDI-C_{13}), desorption can be considered negligible at T_s = 40 °C. In this case, the adsorption probability has increased by about 25% for PTCDI-C_5 and 30% for PTCDI-C_8.

In Figures 4.5(c,d) and 4.6(c,d), we consider the growth of PTCDI-C_5 and PTCDI-C_8 incident on HMDS at E_i = 10.0 eV and E_i = 11.6 eV respectively. In comparison to the growth at lower incident kinetic energy, we see the anti-Bragg oscillations for both PTCDI-C_5 and PTCDI-C_8 are similarly pronounced, indicating that LbL growth extends to similar coverages for these conditions. To fit these data for PTCDI-C_5, we assume that $S_0F \sim 0.002285$ML-s^{-1} , whereas $S_{n\geq 1}F \sim 0.005267$ ML-s^{-1}. These data imply that the rate of growth has accelerated considerably with increasing PTCDI-C_5 coverage. Similarly, for PTCDI-C_8 growth we find $S_0F \sim 0.003725$ ML-s^{-1}, whereas $S_{n\geq 1}F \sim 0.008793$ML-s^{-1}, also indicating a substantial increase in growth rate with increasing PTCDI-C_8 cov-

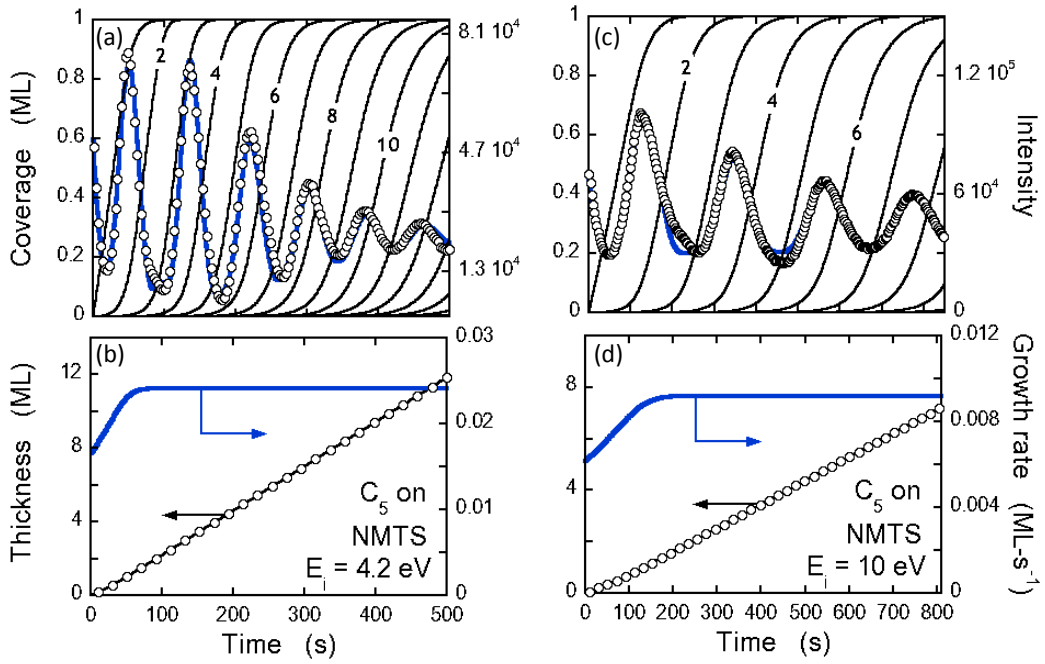

Figure 4.7: X-ray intensities, predicted layer occupancies, total coverages and growth rates for PTCDI-C_5 incident on NMTS—SiO_2 at (a,b) E_i = 4.2 eV and (c,d) 10.0 eV. Details concerning the layout are otherwise identical to those in Figure 4.5.

erage. In this case, the adsorption probability has increased by about 230% for PTCDI-C_5 and 234% for PTCDI-C_8.

In Figure 4.7(a), we present the scattered x-ray intensity acquired in real time at the anti-Bragg condition for the growth of PTCDI-C_5 on NMTS at E_i = 4.2 eV, and in Figure 4.8(a), we present the scattered x-ray intensity acquired in real time at the anti-Bragg condition for the growth of PTCDI-C_8 on NMTS at E_i = 5.1 eV. For the growth of both PTCDI-C_5 and PTCDI-C_8 NMTS, the cusp-

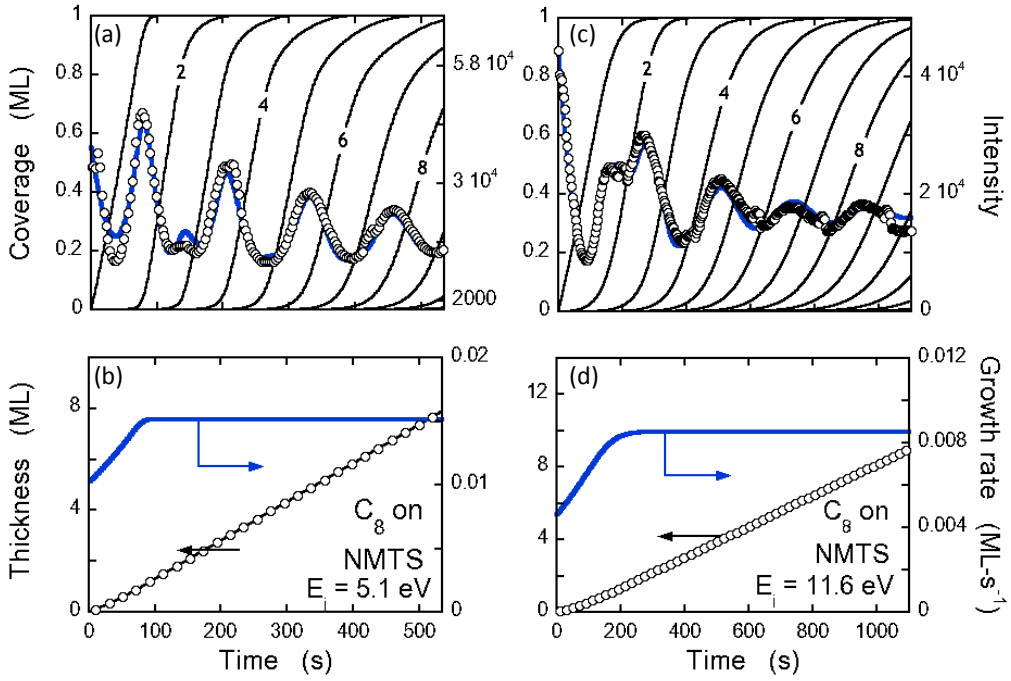

Figure 4.8: X-ray intensities, predicted layer occupancies, total coverages and growth rates for PTCDI-C_8 incident on NMTS—SiO_2 at (a,b) E_i = 5.1 eV and (c,d) 11.6 eV. Details concerning the layout are otherwise identical to those in Figure 4.6.

like maxima as 2, 4, 6 and 8 MLs are completed are clearly visible. For the case of PTCDI-C_8, small maxima can be seen at 1 and 3 MLs, but these are obscured for the case of PTCDI-C_5. Concerning the kinetics of growth, as shown in Figure 4.7(b) and Figure 4.8(b), we find the data can be described by a model where there is modest acceleration in growth. For PTCDI-C_5, we observe an acceleration in the rate of growth of ~53% , while for PTCDI-C_8 we observe an acceleration of ~48%.

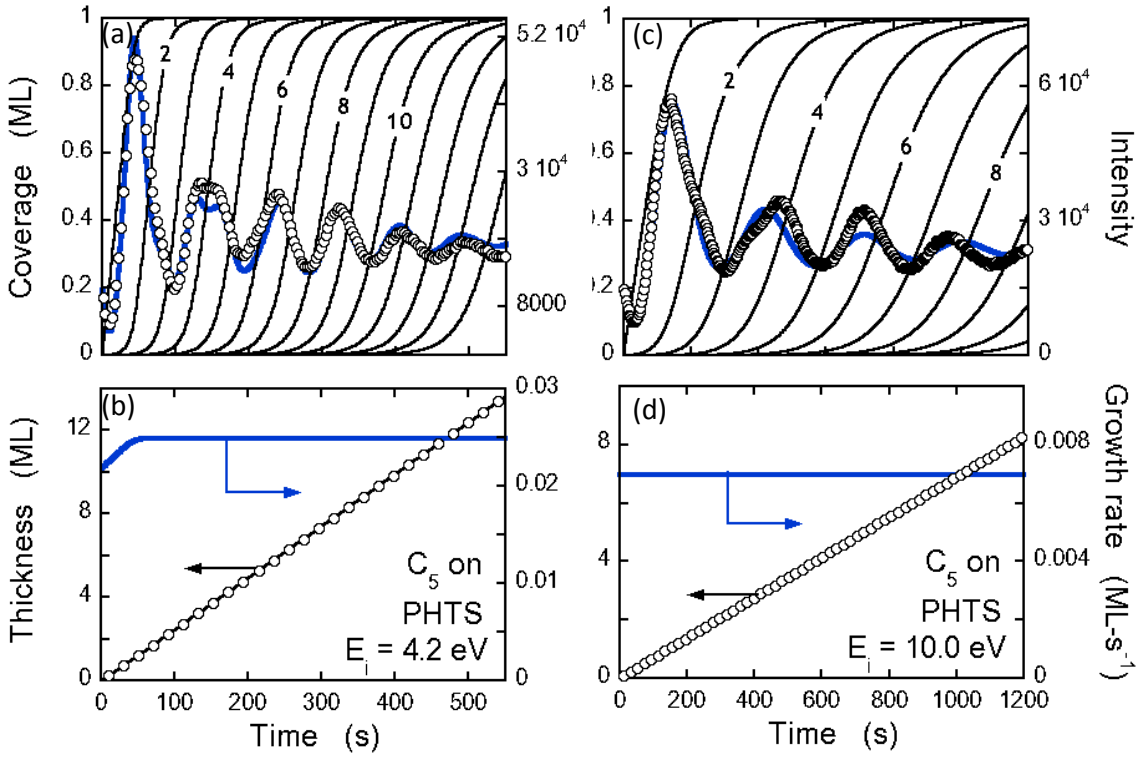

Figure 4.9: X-ray intensities, predicted layer occupancies, total coverages and growth rates for PTCDI-C_8 incident on PHTS—SiO_2 at (a,b) E_i = 4.2 eV and (c,d) 10.0 eV. Details concerning the layout are otherwise identical to those in Figure 4.5.

In Figure 4.7(c,d) and Figure 4.8c,d, we consider the growth of PTCDI-C_5 and PTCDI-C_8 incident on HMDS at E_i = 10.0 eV and E_i = 11.6 eV respectively. In comparison to the growth at lower incident kinetic energy, we see the anti-Bragg oscillations for both PTCDI-C_5 and PTCDI-C_8 are similarly pronounced, indicating that LbL growth extends to similar coverages for these conditions. At the higher incident kinetic energies, for PTCDI-C_5, we observe an acceleration in the rate of growth of ~50% , while for PTCDI-C_8 we observe an acceleration of ~85%. For intermediate kinetic energies, not shown here, we observe similar values of rate acceleration.

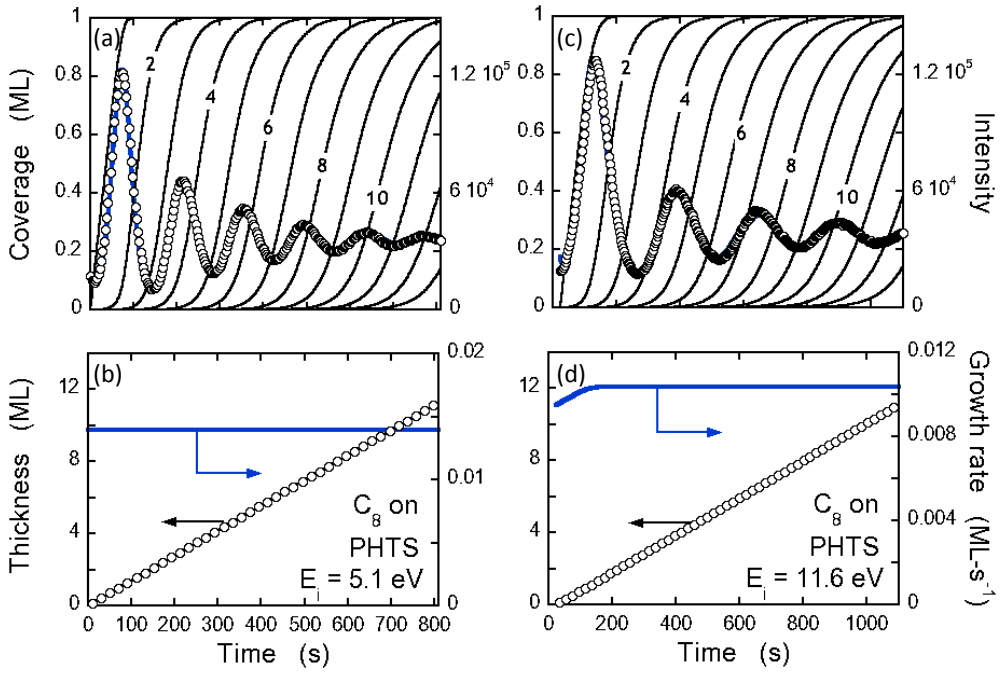

Figure 4.10: X-ray intensities, predicted layer occupancies, total coverages and growth rates for PTCDI-C_8 incident on PHTS—SiO_2 at (a,b) E_i = 5.1 eV and (c,d) 11.6 eV. Details concerning the layout are otherwise identical to those in Figure 4.6.

In Figures 4.9 and 4.10, we display the results for the growth of PTCDI-C_5 and PTCDI-C_8 on PHTS. Similar to growth on the other two surfaces, we see prolonged intensity oscillations, indicating layer by layer growth. At the lowest kinetic energy, we observe a modest acceleration in the growth rate of PTCDI-C_5 of ~3% , while PTCDI-C_8 shows no rate acceleration. At the highest kinetic energies, as shown in Figures 4.9(c,d) and 4.10(c,d), we observe clear oscillations, and a still modest acceleration in the growth rate, with no acceleration for PTCDI-C_5 and 9% for PTCDI-C_8.

To examine the effects of incident kinetic energy on the probability of adsorption (and thus the growth rate), we must account for the change in the incident molecular flux as we varied the kinetic energy. To this end, we have measured the direct intensity of a molecular beam of PTCDI-C_{13} using a quadrupole mass spectrometer, which measure the molecular density in the ionization region, and subsequently corrected for the effect of molecular velocity to calculate a relative molecular flux. Making use of this relative molecular flux, we can then calculate relative probabilities of adsorption. Due to the structural similarity of PTCDI-C_{13}, PTCDI-C_8 and PTCDI-C_5, it is assumed that PTCDI-C_5 and PTCDI-C_8 will exhibit similar changes in flux with kinetic energy. From the discussion and data presented above, it is observed that on SiO_2 modified with HMDS, the adsorption probabilities of PTCDI-C_5 and PTCDI-C_8 differ significantly in the submonolayer and multilayer regimes, manifesting in a marked acceleration in the growth rate, and this effect is more pronounced with increasing incident kinetic energy. For the case of NMTS, while the adsorption probabilities differ between the submonolayer and multilayer regimes, this effect persists over different incident kinetic energies. For PHTS, the differences between the submonolayer and multilayer regimes are more subtle.

In Figures 4.11 and 4.12 we plot relative probabilities of adsorption for PTCDI-C_5, and PTCDI-C_8 on all surfaces examined here for (a) PTCDI-C_n on the growing PTCDI-C_n film, (b) PTCDI-C_n on the starting substrates as a function of incident kinetic energy. We note that the relative probabilities of adsorption for each data set have been normalized to the highest observed growth rate.

Considering adsorption on the starting surfaces, the data exhibit the behavior expected for trapping mediated adsorption: a smooth decrease of the proba-

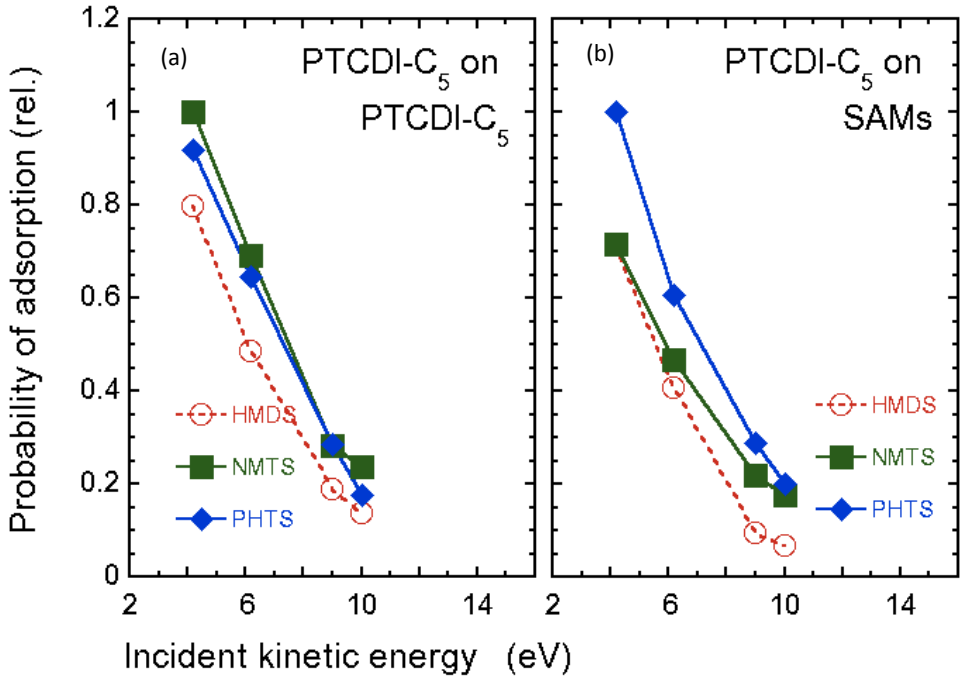

Figure 4.11: Relative probabilities of adsorption versus the incident kinetic energy for PTCDI-C_5 incident on (a) the PTCDI-C_5 covered substrates and (b) the three starting substrates. The probabilities have been normalized to the highest flux-corrected growth rate.

bility of adsorption with increasing kinetic energy. This behavior has also been observed for the adsorption of pentacene **[16,29,30]** and DIP **[19,20]** on clean SiO_2 and SiO_2 modified with HMDS and other SAMs. Observing Figures 4.11(b) and 4.12(b), we see that there is little memory of the starting substrate at each specific energy, and that all the values lie within a band of about ±10%, roughly the experimental uncertainty for these values. Concerning multilayer growth, Figures 4.11(a) and 4.12(a) show that the adsorption of PTCDI-C_n on PTCDI-C_n also exhibits trapping mediated adsorption, and there is a significant decrease in the probability of adsorption as incident kinetic energy increases. This behavior is similar to what has been reported for growth of pentacene **[29]** and PTCDI-C_{13} **[21]**.

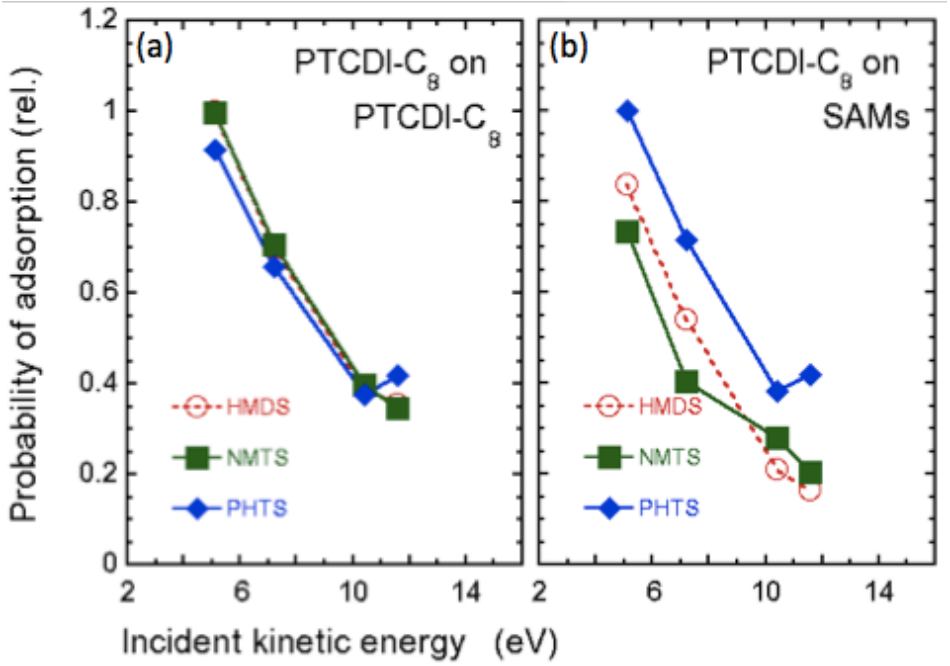

Figure 4.12: Relative probabilities of adsorption versus the incident kinetic energy for PTCDI-C_8 incident on (a) the PTCDI-C_8 covered substrates and (b) the three starting substrates. The probabilities have been normalized to the highest flux-corrected growth rate.

In Figure 4.13, we plot the ratio of the trapping probability in the monolayer regime to that in the multilayer regime. In this representation, there is little to no change in the ratio for the adsorption of PTCDI-C_5 and PTCDI-C_8 on PHTS (ratio ~1). For growth of both molecules on NMTS, there is also little to no change, but for growth on HMDS, the ratio decreases sharply, indicating that the trapping probability of PTCDI-C_n on itself is significantly greater than on HMDS, and this difference increases with incident energy. This is similar to results obtained for growth of PTCDI-C_{13}, where trapping on HMDS was different from trapping on NMTS and PHTS.

One possible reason for the difference in trapping behavior is the strength of molecule-surface interactions. We would anticipate strong binding between

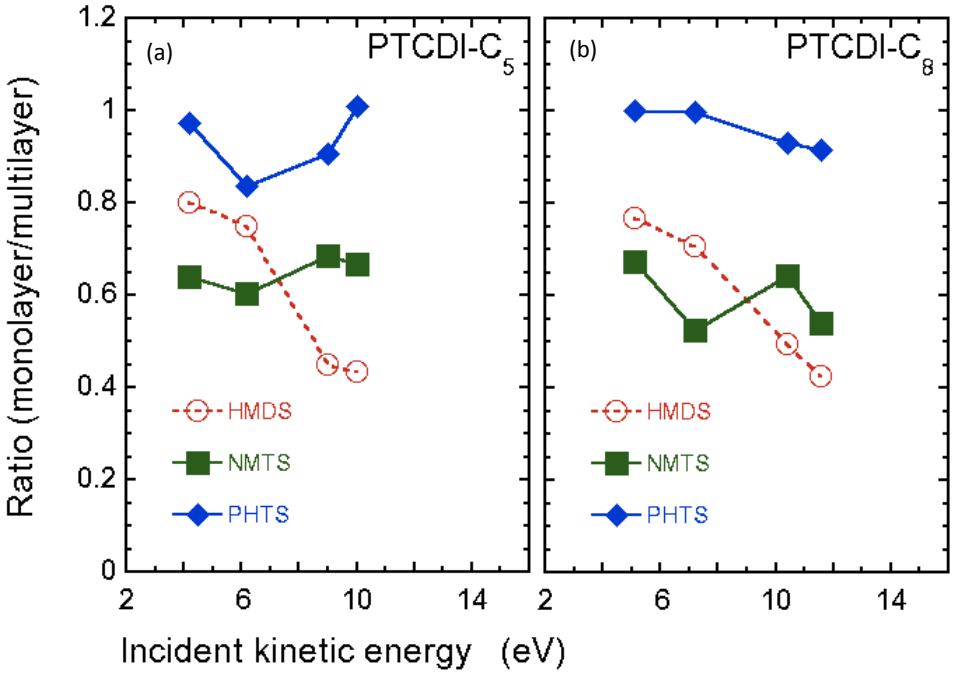

Figure 4.13: Ratio of the probabilities of adsorption (initial monolayer/multilayer) versus the incident kinetic energy for (a) PTCDI-C_5 and (b) PTCDI-C_8 on the three substrates considered here.

PTCDI-C_n and the two SAMs presenting aromatic terminal groups. However, it is not clear if differences in the attractive surface potential (likely $\ll$ 1 eV) could explain differences in adsorption at incident kinetic energies on the order of 10 eV. More likely, the dominant factors are the internal degrees of freedom of the SAM layers, and the structure and density of the SAM layers. As observed previously for DIP on alkyl SAMs on SiO_2, trapping was most efficient on the longest alkyl backbone SAMs, and least efficient on HMDS **[20]**. This observation suggests that energy transfer, and therefore trapping, should be least efficient on HMDS, as we report here for PTCDI-C_5 and PTCDI-C_8 and have previously observed for PTCDI-C_{13} **[21]**.

An additional factor could be direct molecular insertion, where incident

molecules insert themselves into the existing SAM layer. For PTCDI-C_n molecules incident on HMDS, this is not possible due to the thickness of the layer (< 5Å). However for NMTS and PHTS, and for PTCDI-C_n on itself, insertion may play a significant role. In previous studies, the probability of adsorption of pentacene **[29]**, and the adsorption of DIP on three alkyl backbone SAMs **[20]** have been compared to molecular dynamics simulations. In both cases, molecular insertion into the SAM layer or growing thin film layer was found to be significant.

In addition to examining changes in adsorption for a single molecule on different SAMs, we can observe the adsorption behavior of three similar molecules on the same surface. As an example, in Figure 4.14, we plot the ratio of probability of adsorption of PTCDI-C_n on itself to probability of adsorption on HMDS, for PTCDI-C_5, PTCDI-C_8 and PTCDI-C_{13}. Each molecule shows a decrease in this ratio as kinetic energy increases. Though it is difficult to make direct comparisons across different sets of experiments, as we are unable to measure the absolute adsorption probabilities.

4.4.3 Evolution of Surface Roughness

We now consider the thin film morphology and the evolution of surface roughness for PTCDI-C_5 and PTCDI-C_8 grown on the three SAMs examined here, as determined by *ex situ* AFM and the fits to the real time x-ray scattering data (cf. Figures 4.5- 4.10). As these fits produce layer occupancies, they can be used to calculate the RMS roughness (or interface width). To compare directly to data from *ex situ* AFM, we convert the AFM roughness from nanometers to mono-

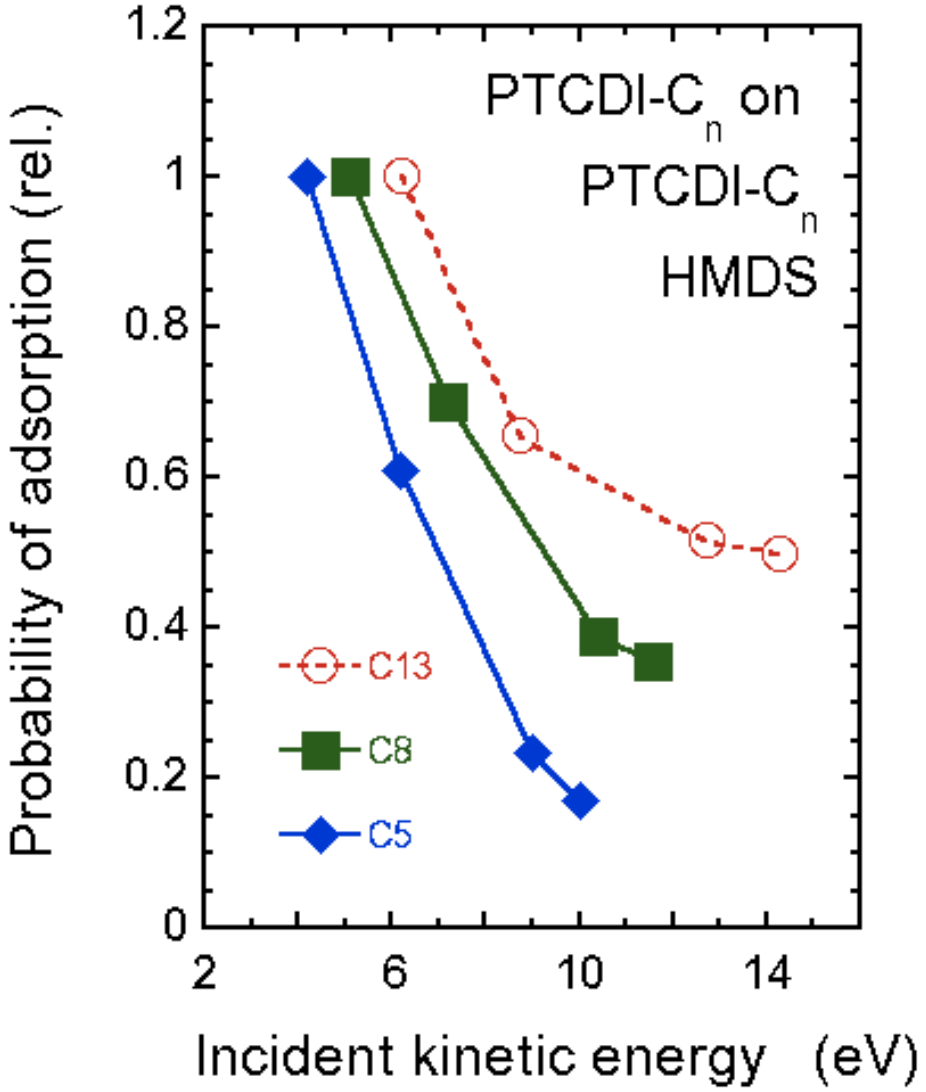

Figure 4.14: Relative probabilities of adsorption versus the incident kinetic energy for PTCDI-C_5, PTCDI-C_8 and PTCDI-C_{13} incident on the PTCDI-C_n covered HMDS substrates.

layers. We note that both methods are susceptible to errors: the roughness from the x-ray data, though representing real time data, depends on the accuracy of the model and goodness of the fit, while the AFM data may be subject to post deposition changes in the thin film. In Figures 4.15 and 4.16, we consider results from growth on all three SAMs examined here for PTCDI-C_5 and PTCDI-C_8, at the lowest kinetic energies (E_i = 4.2 eV for PTCDI-C_5 and E_i = 5.1 eV for PTCDI-C_8). These data show that the growth in roughness is quite slow over all three surfaces for both PTCDI-C_5 and PTCDI-C_8. In comparing the three surfaces, there is no clear trend or significant difference in the evolution of surface roughness. This is consistent with the observation that after the initial adsorption and formation of the first monolayer, there is no memory of the underlying SAM surface.

In addition to comparing a single molecule across different SAMs, it is possible to examine the roughness evolution of three different, but structurally similar molecules on the same surface. In Figure 4.17, we plot the evolution of surface roughness for the growth of PTCDI-C_5, PTCDI-C_8 and PTCDI-C_{13} (grown at 6.3 eV) **[21]** on SiO_2 modified with HMDS. It is interesting to note that at higher film thicknesses PTCDI-C_5 exhibits a relatively smoother film than PTCDI-C_8, which in turn is smoother than PTCDI-C_{13}. However, at the early stages of growth (<4ML) all three films display similar levels of surface roughness, which matches well the previous observation that after adsorption, there is no memory of the original substrate, and differences in roughness and morphology are the result of differences in growth kinetics, such as differences in the energetic barriers to interlayer transport.

This observation, combined with the data shown in Figure 4.18, where we

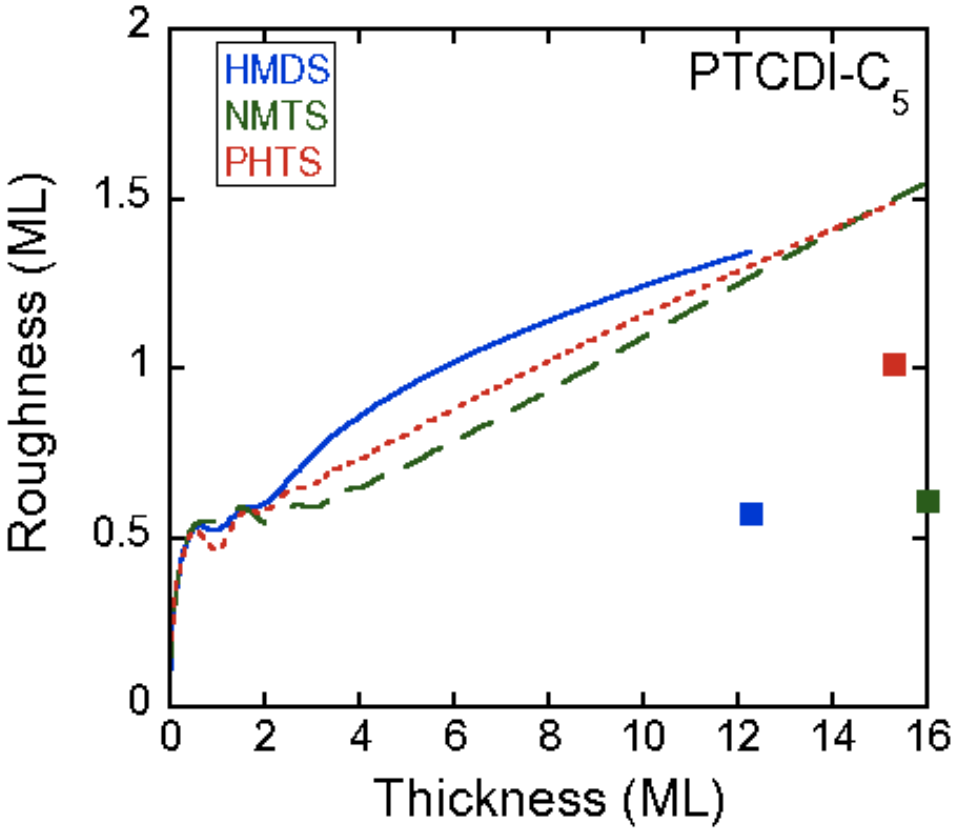

Figure 4.15: Thin film roughness of PTCDI-C_5 as a function of $PTCDI_{C5}$ thickness as predicted by the fit to the x-ray data and comparing HMDS, NMTS and PHTS. Solid squares represent *ex situ* AFM measurements of roughness.

plot normalized scattered x-ray intensity vs. film thickness for the growth of PTCDI-C_5, PTCDI-C_8 and PTCDI-C_{13} **[21]** on HMDS, implies that PTCDI-C_5 grows in a layer-by-layer fashion for longer than PTCDI-C_8 and PTCDI-C_{13}, resulting in a smoother thin film. As was observed for growth of these three molecules on pentacene films (cf. Chapter 5) it seems that the shorter the alkyl side chains attached to the central perylene group, the longer LbL growth is maintained, and the smoother the final thin film. A similar trend has also been reported for n-alkanes **[31]**.

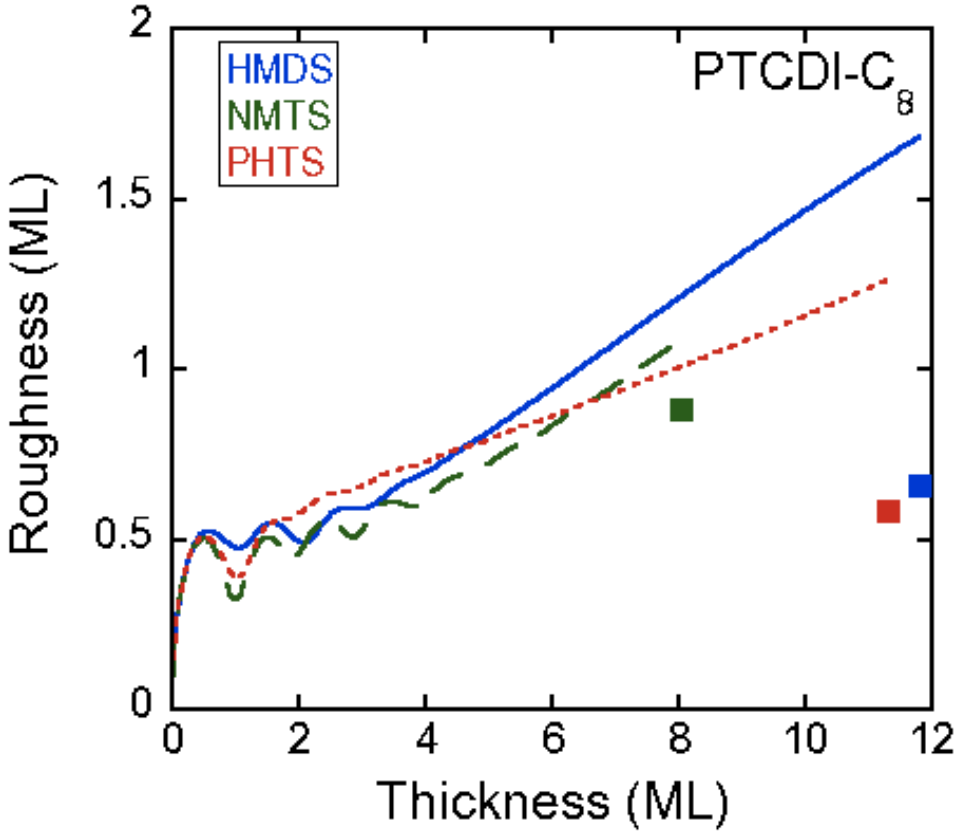

Figure 4.16: Thin film roughness of PTCDI-C_8 as a function of PTCDI-C_8 thickness as predicted by the fit to the x-ray data and comparing HMDS, NMTS and PHTS. Solid squares represent *ex situ* AFM measurements of roughness.

When examining the results for these adsorption studies, it should be noted that several sources of error may make it difficult to observe strong trends. Firstly, the values of incident kinetic energy, and changes of flux with energy were not measured for PTCDI-C_5 and PTCDI-C_8, but extrapolated from previous measurements of PTCDI-C_{13}. Additionally, the version of the modified Cohen model described in section 4.4.3 and used to fit the real time x-ray data presented here has produced fits of limited accuracy. Why this is the case is difficult to say for certain, but two factors may be at work. For one, previous applications of this model (particularly to pentacene and DIP), have dealt with

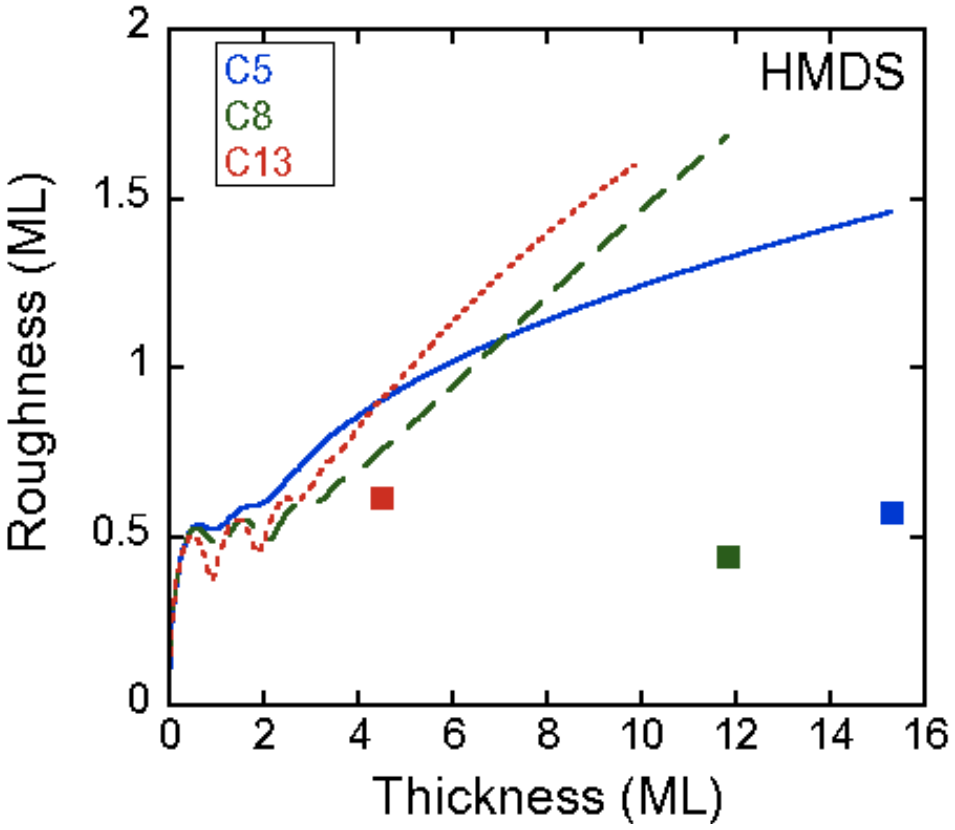

Figure 4.17: Thin film roughness of PTCDI-C_5, PTCDI-C_8 and PTCDI-C_{13} as a function of PTCDI-C_n thickness as predicted by the fit to the x-ray data for growth on HMDS. Solid squares represent *ex situ* AFM measurements of roughness.

layer-by-layer growth for only a few (2 to 4) monolayers. Here, we are attempting to fit much more prolonged oscillations.

4.5 Conclusions

Here we have described a series of experiments probing the adsorption and growth of PTCDI-C_5 and PTCDI-C_8 on SiO_2 surfaces modified with self-assembled monolayers. Real time, *in situ* x-ray scattering data was modeled

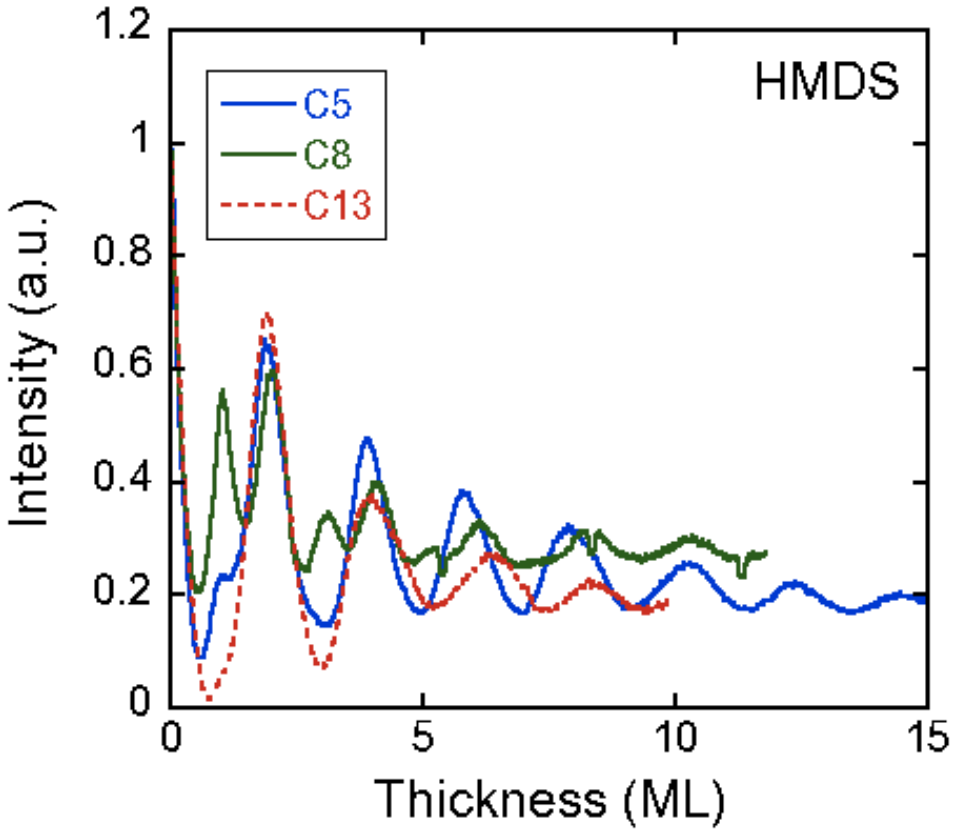

Figure 4.18: Normalized, scattered x-ray intensity at the anti-Bragg position as a function of film thickness for growth of PTCDI-C_5, PTCDI-C_8 and PTCDI-C_{13} on HMDS.

to describe the dynamics of growth, and showed that both molecules grow in a layer by layer fashion for several monolayers, similar to PTCDI-C_{13}. We notice that PTCDI-C_5 grows slightly more smoothly than PTCDI-C_8. We notice that both molecules form well defined, crystalline thin films. For both molecules, the probability of adsorption decreases with incident kinetic energy, demonstrating trapping mediated adsorption behavior. Once the SAM surfaces are covered by a continuous layer of PTCDI-C_5 or PTCDI-C_8, the probability of adsorption is then independent of the SAM, but still exhibits a significant decrease with increasing incident kinetic energy. The adsorption probability of

PTCDI-C_n on itself is similar to that observed on the two SAMs with aromatic end groups (PHTS and NMTS), but it differs significantly from that observed on a relatively short, methyl-terminated SAM. These differences could reflect mechanisms, such as direct molecular insertion into either the existing thin film or the longer chain SAMs, or possibly the effects of greater internal degrees of freedom of the near surface layers in these cases.

4.6 References

1. Hamers, R. J. *Nature*, **2001**, *412*, 489490.
2. Dimitrakopoulos, C. D.; Malenfant, P. R. L. *Adv. Mater.*, **2002**, *14*, 99117.
3. Lin, Y. Y.; Gundlach, D. J.; Nelson, S. F.; Jackson, T. N. *IEEE Electron Device Lett.*, **1997**, *18*, 606608.
4. Kelley, T. W.; Boardman, L. D.; Dunbar, T. D.; Muyres, D. V.; Pellerite, M. J.; Smith, T. P. *J. Phys. Chem. B*, **2003**, *107*, 58775881.
5. Yang, H.; Shin, T. J.; Ling, M. M.; Cho, K.; Ryu, C. Y.; Bao, Z. *J. Am. Chem. Soc.*, **2005**, *127*, 1154211543.
6. Virkar, A.; Mannsfield, S.; Oh, J. H.; Toney, M. F.; Tan, Y. H.; Liu, G.; Scott, J. C.; Miller, R.; Bao, Z. *Adv. Funct. Mater.*, **2009**, *19*, 19621970.
7. Shtein, M.; Mapel, J.; Benziger, J. B.; Forrest, S. R. *Appl. Phys. Lett.*, **2002**, *81*, 268270.
8. Klauk, H.; Halik, M.; Zschieschang, U.; Schmid, G.; Radlik, W.; Weber, W. *J. Appl. Phys.*, **2002**, *92*, 52595263.
9. Briseno, A. L.; Mannsfeld, S. C. B.; Reese, C.; Hancock, J. M.; Xiong, Y.; Jenekhe, S. A.; Bao, Z.; Xia, Y. *Nano Lett.*, **2007**, *7*, 2847-2853.

10. Rost, C.; Gundlach, D. J.; Karg, S.; Riess, W. *J. Appl. Phys.*, **2004**, *95*, 5782-5787.

11. Hiroshiba, N.; Hayakawa, R.; Petit, M.; Chikyow, T.; Matsuishi, K.; Wakayama, Y. *Thin Solid Films*, **2009**, *518*, 441-443.

12. Pandey, A. K.; Dabos-Seignon, S.; Nunzi, J. *Appl. Phys, Lett.*, **2006**, *89*, 113506/1-113506/2.

13. Petit, M.; Hayakawa, R.; Wakayama, Y.; Chikyow, T. *J. Phys. Chem. C.*, **2007**, *111*, 12747-12751.

14. Wiatrowski, M.; Dobruchowska, E.; Maniukiewicz, W.; Pietsch, U.; Kowlaski, J.; Szamel, Z.; Ulanski, J. *Thin Solid Films*, **2010**, *518*, 2266-2270.

15. Tang, F.; Chan, J.; Wu, F.; Cheng, H.; Hsu, S. L; Chen, J.; Chou, W. *J. Mater. Chem.*, **2012**, *22*, 22409-22417.

16. Killampalli, A. S.; Schroeder, T. W.; Engstrom, J. R. *Appl. Phys. Lett.*, **2005**, *87*, 033110.

17. Schroeder, T. W. *Cornell University: Ph.D. Thesis*, 2004.

18. Hong, S.; Amassian, A.; Woll, A. R.; Bhargava, S.; Ferguson, J. D.; Malliaras, G. G.; Brock, J. D.; Engstrom, J. R. *Appl. Phys. Lett.*, **2008**, *92*, 253304.

19. Amassian, A.; Desai, T. V.; Kowarik, S.; Hong, S.; Woll, A. R.; Malliaras, G. G.; Schreiber, F.; Engstrom, J. R. *J. Chem. Phys.*, **2009**, *130*, 124701.

20. Desai, T.; Hong, S.; Woll, A. R.; Hughes, K. J.; Ananth, P.; Clancy, P.; Engstrom, J. R. *J. Chem. Phys.*, **2011**, *134*, 224702.

21. Desai, T. V.; Kish, E. R.; Woll, A. R.; Engstrom, J. R. *J. Phys. Chem. C.*, **2011**, *115*, 37, 18221-18234.

22. Desai, T. V. *Cornell University: Ph.D. Thesis*, 2011.

23. Scoles, G. *Atomic and Molecular Beam Methods* (Oxford University Press, Oxford, UK, 1998).

24. Chen, R.; Kim, H.; McIntyre, P. C.; Bent, S. F. *Chem. Mater.*, **2005**, *17*, 3, 536-544.

25. Kowarik, S.; Gerlach, A.; Skoda, M.; Sellner, S.; Schreiber, F. *Eur. Phys. J. Special Topics*, **2009**, *168*, 11.

26. Woll, A. R.; Desai, T. V.; Engstrom, J. R. *Phys. Rev. B.*, **2011**, *84*, 075479/1-075479/13.

27. Cohen, P. I.; Petrich, G. S.; Pukite, P. R.; Whaley, G. J.; Arrott, A. S. *Surface Sci.*, **1989**, *216*, 222-248.

28. Krauss, T. N.; Barrena, E.; Zhang, X. N.; de Oteyza, D. G.; Major, J.; Dehm, V.; Wuerthner, F.; Cavalcanti, L. P.; Dosch, H. *Langmuir*, **2008**, *24*, 12742-12744.

29. Goose, J. E.; Killampalli, A. S.; Clancy, P.; Engstrom, J. R. *J. Phys. Chem. C*, **2009**, *113*, 60686073.

30. Killampalli, A. S.; Engstrom, J. R. *Appl. Phys. Lett.*, **2006**, *88*, 143125.

31. Weber, C.; Frank, C.; Bommel, S.; Rukat, T.; Leitenberger, W.; Schaefer, P.; Schreiber, F.; Kowarik, S. *J. Chem. Phys.*, **2012**, *136*, 204709.

CHAPTER 5

ORGANIC HETEROSTRUCTURE FORMATION: X-RAY STUDIES OF BILAYER AND MULTILAYER STRUCTURES OF PENTACENE AND PERYLENE DERIVATIVES

5.1 Overview

We have examined the formation and growth of heterostructures of the *n*-type organic semiconductors N,N-dipentylperylene-3,4,9,10-tetracarboxylic diimide (PTCDI-C_5), N,N-dioctcylperylene-3,4,9,10-tetracarboxylic diimide (PTCDI-C_8), and N,N-dioctcylperylene-3,4,9,10-tetracarboxylic diimide (PTCDI-C_{13}) with the *p*-type organic semiconductor pentacene using *in situ* synchrotron x-ray scattering and *ex situ* atomic force microscopy. From real-time x-ray scattering, we find that all three PTCDI-C_n molecules exhibit prolonged layer-by-layer growth for several monolayers when deposited on pentacene surfaces. We observe that PTCDI-C_5 grows smoothly for the longest, while PTCDI-C_{13} is the first to start roughening. In contrast, pentacene thin films grown on PTCDI-C_n surfaces display immediate 3D islanded growth, resulting in extremely rough films. In this work, we also present studies of multilayer structures, composed of alternating layers of PTCDI-C_n and pentacene. We find that the PTCDI-C_{13} displays interesting, smoothing effects when integrated into a multilayer structure with pentacene, while PTCDI-C_5 displays a strikingly different roughening effect. Such studies may be of use when choosing materials for the active layer of organic photovoltaic devices.

5.2 Introduction

Complex conjugated molecules have been extensively studied for applications in thin film electronics and photovoltaics due to their electronic properties and ability to form highly ordered films at relatively low temperatures. Of particular interest is the challenge of integrating both *p*-type (e.g. pentacene) and *n*-type small molecule organic semiconductors into the same device structure. This is necessary for the fabrication of devices such as small molecule based photovoltiacs, field effect transistors, ambipolar devices and complementary inverters **[1]**. In this study, we observe the growth of heterojunctions composed of the *p*-type organic semiconductor pentacene and a group of *n*-type organic semiconductor molecules. Each *n*-type molecule consists of an aromatic perylene core and aliphatic side chains: N,N-ditridecylperylene-3,4,9,10-tetracarboxylic diimide (PTCDI-C_{13}), N,N-dioctylperylene-3,4,9,10-tetracarboxylic diimide (PTCDI-C_8), and N,N-dipentylperylene-3,4,9,10-tetracarboxylic diimide (PTCDI-C_5). The structures of these three molecules are illustrated in Figure 5.1. Both PTCDI-C_{13} and PTCDI-C_8 have been well studied, both as thin films and as the active material in devices. Heterojunctions of pentacene or other *p*-type organic semiconductors and PTCDI-C_8 or PTCDI-C_{13} have been used to fabricate photovoltaic and ambipolar devices **[1-4]**. PTCDI-C_5 is comparatively less well studied, but has been shown to form an ordered thin film **[5-7]**.

Heterostructures composed of inorganic semiconductors have long been studied for a variety of applications **[8]**. So called superlattices composed of alternating layers of two different inorganic semiconductors have been fabricated from a variety of materials **[9]** for photonic **[10]** and photovoltaic devices **[11]**. Such inorganic superlattice structures, when examined by x-ray diffraction **[12]**,

display distinct diffraction peaks, demonstrating a well ordered superstructure. However, constructing such superlattices from organic materials is considerably more difficult, owing to the difficulty of growing epitaxial organic films as the organic molecules are bound by weak van der Waals interactions rather then strong covalent bonds **[13]**. And while roughness in inorganic heterojunctions is often driven by lattice mismatch **[14]**, for organic-organic heterostructures, surface energy and adhesion energy at the interface is a serious concern **[15]**.

In the fabrication of organic photovoltaic devices, the interface between layers of *n*-type and *p*-type semiconductors is of particular interest, as it plays a vital role in charge separation. Heterostructures more complex than simple bilayer junctions are desirable for organic photovoltaic devices due to the fact that the efficiency of a bilayer device is limited as charge separation only occurs near the donor-acceptor interface **[16]**. The desirable thickness of an active layer in such a device is limited by the relatively short exciton diffusion lengths in organic semiconductors, typically on the order of 10 nm **[17]**. This, combined with the desire for high interfacial area to facilitate charge separation, has led to investigation of more complex structures, such as co-deposited films and multilayer stacks **[18-20]**. To examine the complicated structures of such films, x-ray scattering has been shown to be a useful tool **[21]**. In addition to such structures based on small molecule organic semiconductors **[22]**, bulk heterojunctions composed of semiconducting polymers have been extensively studied **[23]**.

Here we report on the thin film growth of PTCDI-C_n on ultrathin films of pentacene and the thin film growth of pentacene on ultrathin PTCDI-C_n films using a combination of *in situ* and *ex situ* surface sensitive techniques. In addi-

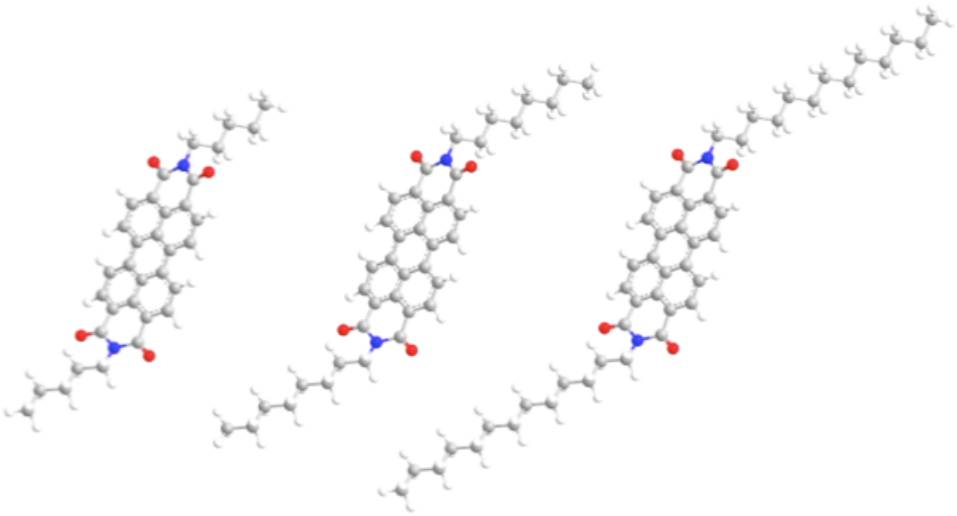

Figure 5.1: Drawings of the structure of (a) PTCDI-C_5 (b) PTCDI-C_8 and (c) PTCDI-C_{13}

tion to bilayer structures, we also examine more complex multilayer structures consisting of alternating monolayers of pentacene and PTCDI-C_n. In this work, we deposit thin films of PTCDI-C_n in ultrahigh vacuum (UHV) using a collimated supersonic molecular beam and pentacene thin films with a conventional thermal evaporator. In addition, we make use of *in situ*, real time synchrotron x-ray scattering to monitor the dynamics of thin film growth. We observe the differences in bilayer and multilayer structure caused by the differing side chain length from PTCDI-C_5 up to PTCDI-C_{13} and the difference in surface energy of pentacene and PTCDI-C_n surfaces.

5.3 Experimental procedures

The experiments were carried out in the G3 station of the Cornell High Energy Synchrotron Source (CHESS) in a custom-designed UHV system fitted with Be

windows that is described in detail elsewhere **[24]**. Briefly, the system consists of four separately pumped chambers: a main scattering chamber, a source and antechamber, which act to produce the supersonic beam, and a fast entry load-lock. All chambers are pumped by high-throughput turbomolecular pumps. The base pressure of the chamber was typically around 4×10^{-9} Torr and samples were loaded via the load-lock chamber, which was evacuated to $\sim 10^{-7}$ Torr prior to sample transfer into the main chamber.

Substrates were Si(100) wafers (Wacker-Siltronic, *p*-type, 100 mm dia., 500-550 μm thick, 38-63 Ω-cm) subject to a SC-1 clean, 15 s HF dip and a SC-2 clean followed by growth of 300-nm-thick SiO_2 films by wet thermal oxidation at 1100°C. Next, these wafers were cleaned and degreased by sonication for 15 min in anhydrous $CHCl_3$ solution (99 %+), sonicated in deionized (DI) water for 15 min, washed with DI water, dried with N_2 and exposed to UV-ozone for 15 min. These processes provided a clean and reproducible hydrophilic surface.

Supersonic molecular beams of PTCDI-C_{13}, PTCDI-C_8 and PTCDI-C_5 (99.8% Sigma-Aldrich Corp.) were generated by passing a carrier gas (He, 99.999%) through a temperature-controlled container (the evaporator) containing these species located upstream of the nozzle (150 μm orifice). The doubly differentially pumped beam passed through a trumpet shaped skimmer into an antechamber and through an aperture that produced a well-defined beam spot on the substrate surface. The mean kinetic energy of the molecules in the supersonic molecular beam can be controlled by adjusting the flow rate of the carrier gas. During deposition the substrate temperature was kept at $T_s \sim 40$°C, and in all cases the supersonic beam was incident along the surface normal.

In addition to the supersonic molecular beam source, we also make use of a

conventional thermal effusion source (CreaTec Fischer and Co. GmbH) to generate near thermal energy incident fluxes of pentacene. This source possesses a 10 cm^3 crucible constructed of pyrolytic BN, and it is fitted with a pneumatically controlled shutter. In our system, the source is mounted directly to the main scattering chamber of UHV system (angle of incidence is 45° off the substrate surface normal, 10 cm from the substrate surface), which also houses the sample. For deposition from the thermal source a translatable shadow mask, possessing a square 15 × 4 mm^2 opening, ~5 mm from the substrate surface, was used to define a beam spot on the sample. During these experiments, the thermal effusion source was heated to a temperature (ca. 105 °C) to achieve the desired flux, the shadow mask was moved into place, and the shutter was opened and then closed to produce the desired exposure.

Time-resolved and *in situ* measurements of the scattered x-ray synchrotron intensity were made using a silicon avalanche photodiode detector (APD, Oxford Danfysik, Oxford, UK). During PTCDI-C_n and pentacene thin film growth the intensity was monitored at the anti-Bragg position ($q_z = q_{Bragg}/2$), which is an effective monitor of the nature of growth, i.e., layer-by-layer (LbL) vs. 3D islanded growth **[28]**. Following deposition and x-ray analysis, the samples were removed for *ex situ* analysis using atomic force microscopy (AFM), conducted in tapping mode using a DI 3100 Dimension microscope.

The x-ray data at the anti-Bragg position was fitted using a modified version **[25,26]** of the mean-field rate equation model of growth first proposed by Cohen and co-workers **[27]**. Briefly, the equations for the coverage of individual layers (θ_n) are given by:

$$\frac{d\theta_n}{dt} = S_{n-1}F[(\theta_{n-1} - \theta_n) - \alpha_{n-1}(\theta_{n-1} - \theta_n)] + S_nF\alpha_n(\theta_n - \theta_{n+1}) \qquad (5.1)$$

where $n = 0$ represents the substrate, $n = 1$ the first molecular layer, etc., S_n is the probability of adsorption for molecules incident on the n^{th} layer, F is the incident molecular flux (ML-s^{-1}), and ?n is the fraction of molecules that after initially impacting and landing on top of the n^{th} layer, then drop down and become part of the n^{th} layer via some mechanism (e.g. overcoming the Ehrlich-Schwoebel barrier at a step edge). In this model we also assume that there are two values for the probability of adsorption: one for adsorption on the substrate (S_0), and one for that on previously existing molecular layers, independent of their thickness ($S_1 = S_2 = S_3$).

Once layer coverages have been calculated by integrating Equation 5.1, these can then be used to calculate the scattered x-ray intensity as a function of time **[25-28]**. The intensity of the scattered beam (I) depends upon the layer population, $\theta_n(t)$, according to the following relationship:

$$I(t) = \left| r_{subs} e^{-i\phi} + r_{film} \sum_{n=1}^{\infty} \theta_n(t) e^{-iq_z dn} \right|^2 \tag{5.2}$$

where r_{subs} and r_{film} are the scattering amplitudes of the substrate and the film, ϕ is the phase change upon reflection, q_z is the out-of-plane scattering vector and d is the out-of-plane interplanar spacing. At the anti-Bragg position, $q_z d = \pi$, which results in a change in the sign of the thin film terms in the summation. If each layer fills sequentially, such as in perfect LbL growth, an oscillation in the intensity results.

5.4 Results and discussion

5.4.1 Morphology and x-ray reflectivity of PTCDI-C_n films grown on ultrathin pentacene films

Thin films of pentacene of one monolayer (ML) thickness were grown on SiO_2 via thermal evaporation. Figure 5.2(a) shows an atomic force (AF) micrograph of a pentacene film approximately one ML thick deposited on SiO_2. As can be seen from the image, while the second monolayer has just begun to nucleate, the height histogram in Figure 5.2(b) shows that this still provides a smooth surface for subsequent growth of PTCDI-C_n. In Figure 5.3 we display real time scattering data at the anti-Bragg condition for growth of PTCDI-C_5 (Figure 5.3(a)), PTCDI-C_8 (Figure 5.3(b)), and PTCDI-C_{13} (Figure 5.3(c)) on 1 ML of pentacene. The intensity oscillations at the anti-Bragg condition observed here are expected for layer-by-layer growth due to the alternating contributions of the odd and even layers to the magnitude of the scattered intensity. As can be seen, all three PTCDI molecules grow in a layer-by-layer (LbL) fashion up to several monolayers. A trend is also apparent, such that the molecule with the shortest alkyl side chains (PTCDI-C_5) grows in a layer-by-layer fashion the longest, while the molecule with the shortest side chains (PTCDI-C_{13}) transitions to a rougher, three-dimensional growth mode the soonest, with PTCDI-C_8 displaying intermediate behavior. In comparison with our previous work with pentacene **[29]**, DIP **[30]** and PFP **[30]**, all three perylene derivatives grow exceptionally smoothly, while PTCDI-C_{13} growth on pentacene appears similar to its growth on SAMs **[31]**.

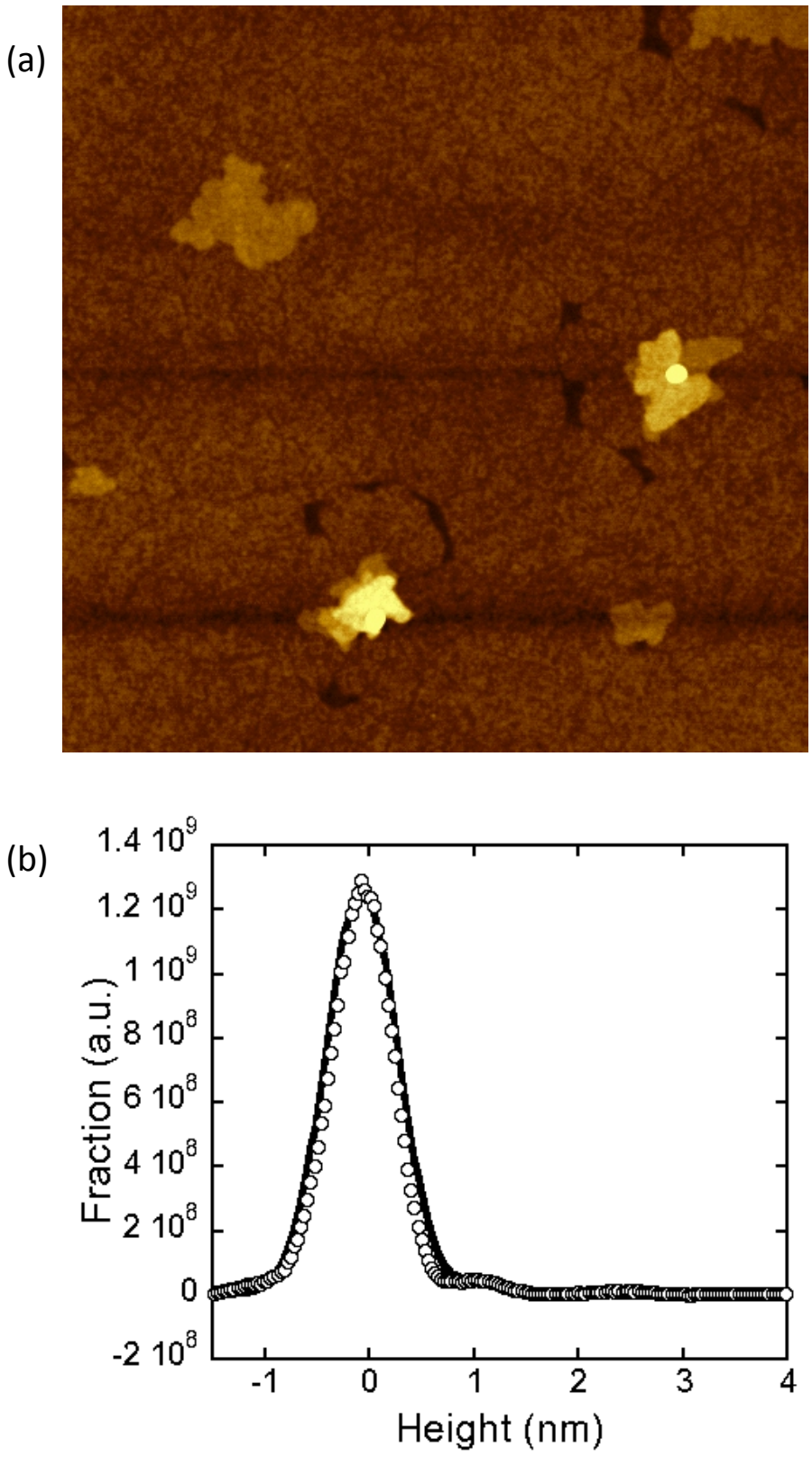

Figure 5.2: (a) 3m x 3m atomic force micrograph of 1 ML pentacene deposited on SiO_2. (b) Height distribution of the micrograph

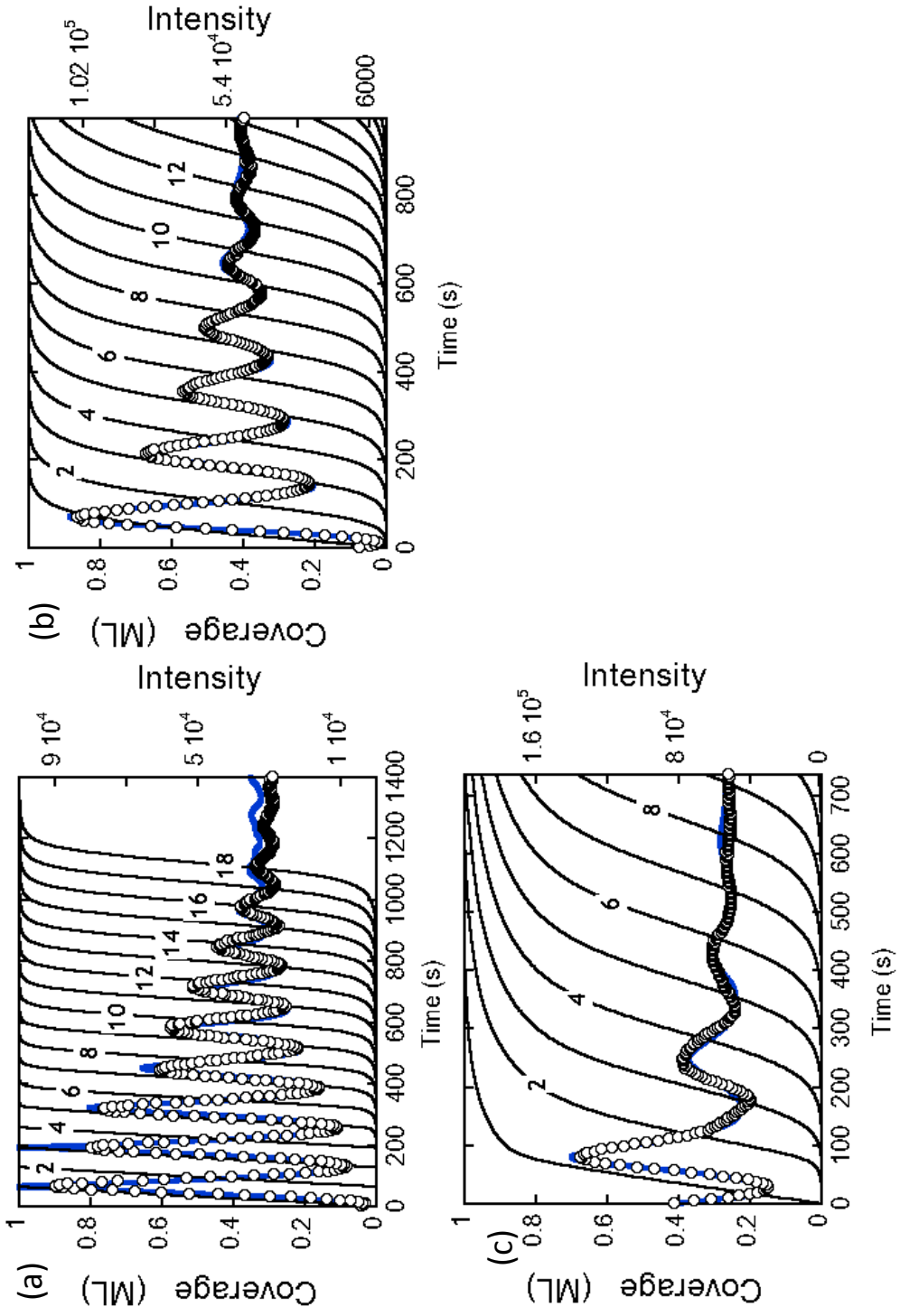

Figure 5.3: X-ray intensity at the anti-Bragg condition as a function of exposure to the molecular beam of (a) PTCDI-C_5 (b) PTCDI-C_8 and (c) PTCDI-C_{13}, grown on a pre-deposited monolayer of pentacene. Thick solid lines (right ordinate) indicate a fit of the data to a model, and thin solid curves (left ordinate) represent predicted coverages (θ_n) of the individual layers.

The kinetics of growth can be modeled more precisely by making use of Equations 5.1 and 5.2, and this result is also shown in Figure 5.3. We show the coverage of each layer (solid black curves) predicted by the fit to the intensity oscillations (solid blue line). Using the layer coverages predicted by the fit, the RMS roughness can be calculated and compared to RMS roughness measured by *ex situ* AFM.

In Figure 5.4 we present sample atomic force micrographs of PTCDI-C_n films grown on 1 ML pentacene. Along with each micrograph, we show a sample linescan to illustrate the heights of visible features. Films of PTCDI-C_5 exhibit the smoothest morphology, showing terraces roughly a single monolayer in height. PTCDI-C_{13} shows some very tall features which have been observed after growth on other surfaces **[31-33]**. PTCDI-C_8 shows intermediate behavior, not quite as smooth as PTCDI-C_5, and exhibiting some tall features, though considerably fewer than PTCDI-C_{13}. The RMS roughness of each film can be extracted from these micrographs. To compare directly to the data from AFM, we use a thickness for a monolayer of PTCDI-C_{13} of 26.8 ± 0.1Å, for a monolayer of PTCDI-C_8 of 20.3 ± 0.1Å and for PTCDI-C_5 of 18.3 ± 0.1Å, each determined from x-ray reflectivity. We note that both techniques are susceptible to inaccuracies: the roughness from *in situ* x-ray scattering depends on the accuracy of the model, but nevertheless does represent a real time result; whereas the results from *ex situ* AFM may be compromised by post-deposition reorganization of the thin film **[34]**.

In Figure 5.5 we plot the RMS surface roughness of thin films of PTCDI-C_n deposited on 1ML of pentacene as a function of total coverage as predicted by the fit to the x-ray data (smooth line) for the conditions used to deposit the

films displayed in Figure 5.3. For comparison we also plot the values obtained from the *ex situ* AFM (solid circles). While the x-ray model over predicts the roughness for some of the films, particularly those of PTCDI-C_{13}, both AFM and the x-ray data suggest prolonged layer by layer growth.

Figure 5.6 shows *ex situ* XRR data taken at the G2 station of CHESS. The scattered intensity exhibits well-defined Bragg peaks. For PTCDI-C_{13}, peaks up to the 4^{th} order can be seen with well-defined Laue oscillations indicative of a well-ordered lamellar structure. For PTCDI-C_8, peaks up to the 3^{rd} order are observed. While for PTCDI-C_5, only the 2^{nd} order peak can be seen. The PTCDI-C_5 peaks do not display the same well-defined Laue oscillations, although the data is complicated by the presence of both a bulk and a thin film phase with slightly different *d*-spacings **[5]**. We note here that the results of growing PTCDI-C_{13} on a thin film of pentacene are quite similar to previous results from PTCDI-C_{13} growth on self-assembled monolayers **[31]**. The data show that each of the three molecules forms a well ordered and oriented thin film.

5.4.2 Morphology and x-ray reflectivity of pentacene films grown on ultrathin PTCDI-C_n films

Thin films of PTCDI-C_n were grown on SiO_2 via supersonic molecular beam deposition. These films were then used as a starting surface for the growth of pentacene films via thermal evaporation. In Figure 5.7 we display real time scattering data at the anti-Bragg condition for growth of pentacene on 1 ML films of (a) PTCDI-C_5 (b) PTCDI-C_8 and (c) PTCDI-C_{13}. In all three cases, no oscillations are observed, suggesting that pentacene does not grow LbL on PTCDI-C_n, but

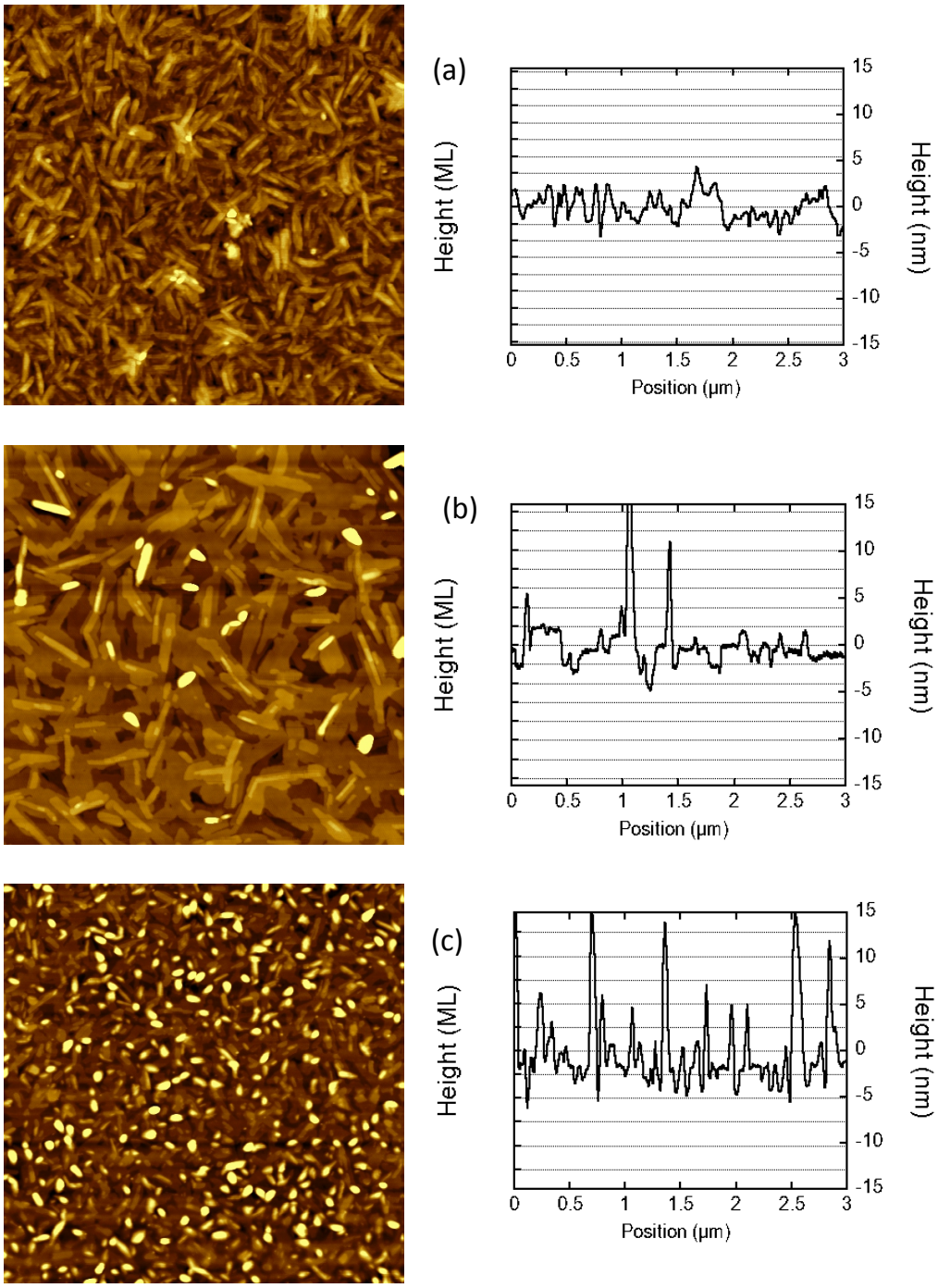

Figure 5.4: Example set of 3μm x 3μm atomic force micrographs of thin films of (a) PTCDI-C_5 (b) PTCDI-C_8 and (c) PTCDI-C_{13}, grown on a pre-deposited monolayer of pentacene. Line profiles are shown accompanying each micrograph.

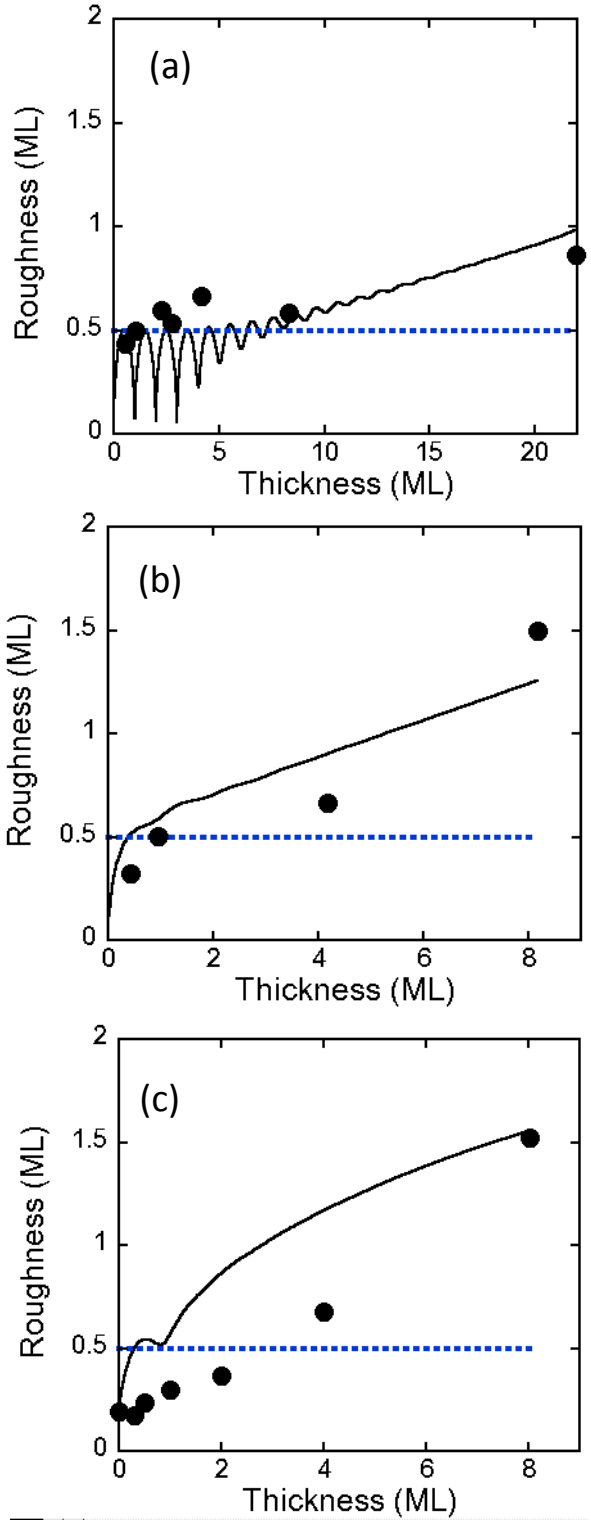

Figure 5.5: Thin film roughness as a function of film thickness for (a) PTCDI-C_5 (b) PTCDI-C_8 and (c) PTCDI-C_{13}, grown on a pre-deposited monolayer of pentacene as predicted by the fit to the X-ray data. Solid circles represent roughness obtained directly from AF micrographs.

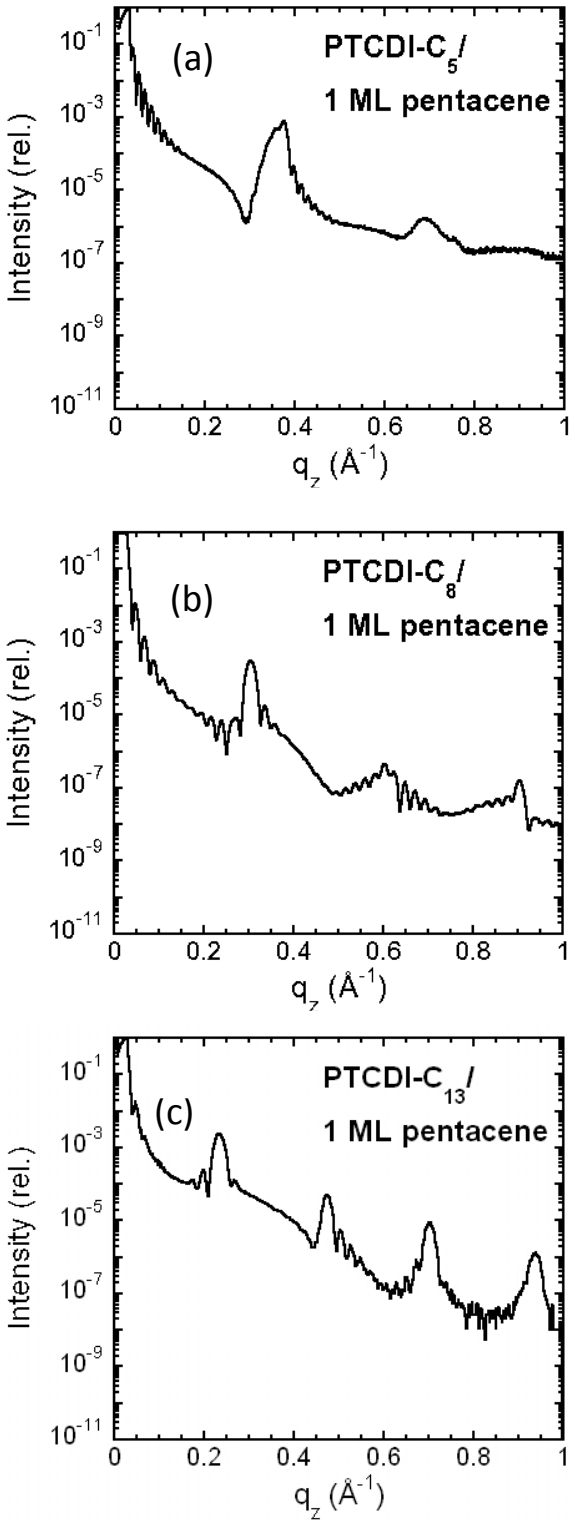

Figure 5.6: Specular x-ray reflectivity (XRR) of the films shown in Figure 5.4

immediately exhibits three-dimensional growth.

Although no oscillations are observed, the x-ray data can still be fit to our model using Equations 5.1 and 5.2. Also shown in Figure 5.7 are the coverages of each layer (solid black curves) predicted by the fit to the real time intensity (solid blue line). These fits are based on the known growth rate of pentacene on SiO_2 for the same evaporator temperature. For thermal growth the probability of adsorption is assumed to be unity; the growth rate is therefore dependent only on the flux of pentacene from the evaporator. The model can then capture the lack of oscillations by assuming large energetic barriers to interlayer transport. However, the fits are not very accurate, especially when compared with *ex situ* AFM data. The modified Cohen model cannot simulate Volmer-Weber growth.

In Figure 5.8 we show 3μm $\times$ 3μm AF micrographs of pentacene films deposited on each PTCDI-C_n film. Also shown are sample lines height profiles from each image, and height histograms of both the starting PTCDI-C_n film, and the film after 4 ML of pentacene have been deposited. In all three cases, the pentacene films display similar morphology. The pentacene does not fully cover the surface of the PTCDI-C_n film, instead forming tall, plateau-like features. This can be seen both in the linescans, with large, up to 10 ML tall features being common. Terraces of roughly 1 ML height, common for pentacene on SiO_2, are not observed here. The height histograms corroborate this observation. The height histograms are bimodal, showing that some areas of the PTCDI-C_n film remain uncovered, while other areas are covered by extremely tall, plateau-like pentacene features. This behavior is in contrast to pentacene grown on high surface energy self-assembled monolayers **[34]**. On such surfaces, pentacene

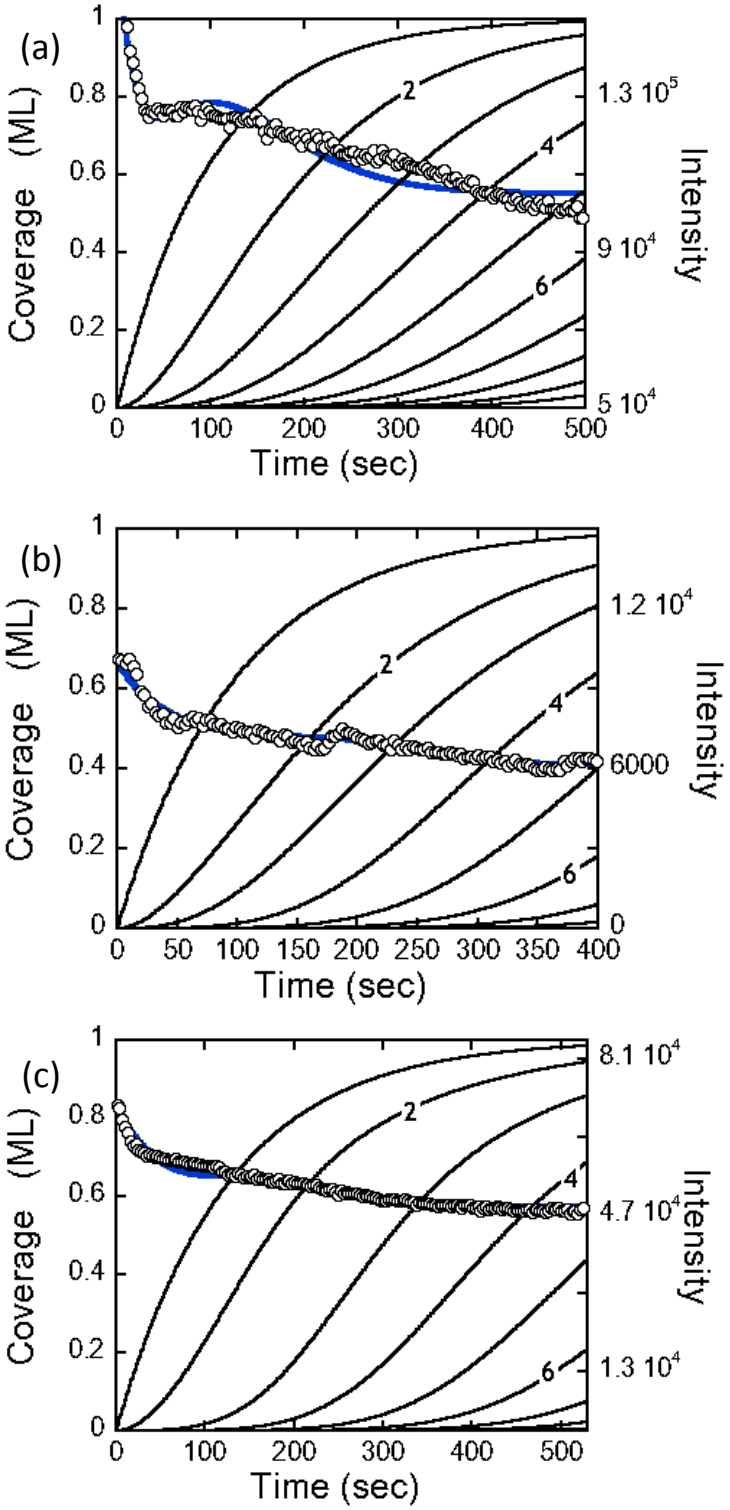

Figure 5.7: X-ray intensity at the anti-Bragg condition as a function of exposure to the effusive beam of pentacene on pre-deposited monolayers of (a) PTCDI-C_5 (b) PTCDI-C_8 and (c) PTCDI-C_{13}. Thick solid lines (right ordinate) indicate a fit of the data to a model, and thin solid curves (left ordinate) represent predicted coverages (θ_n) of the individual layers.

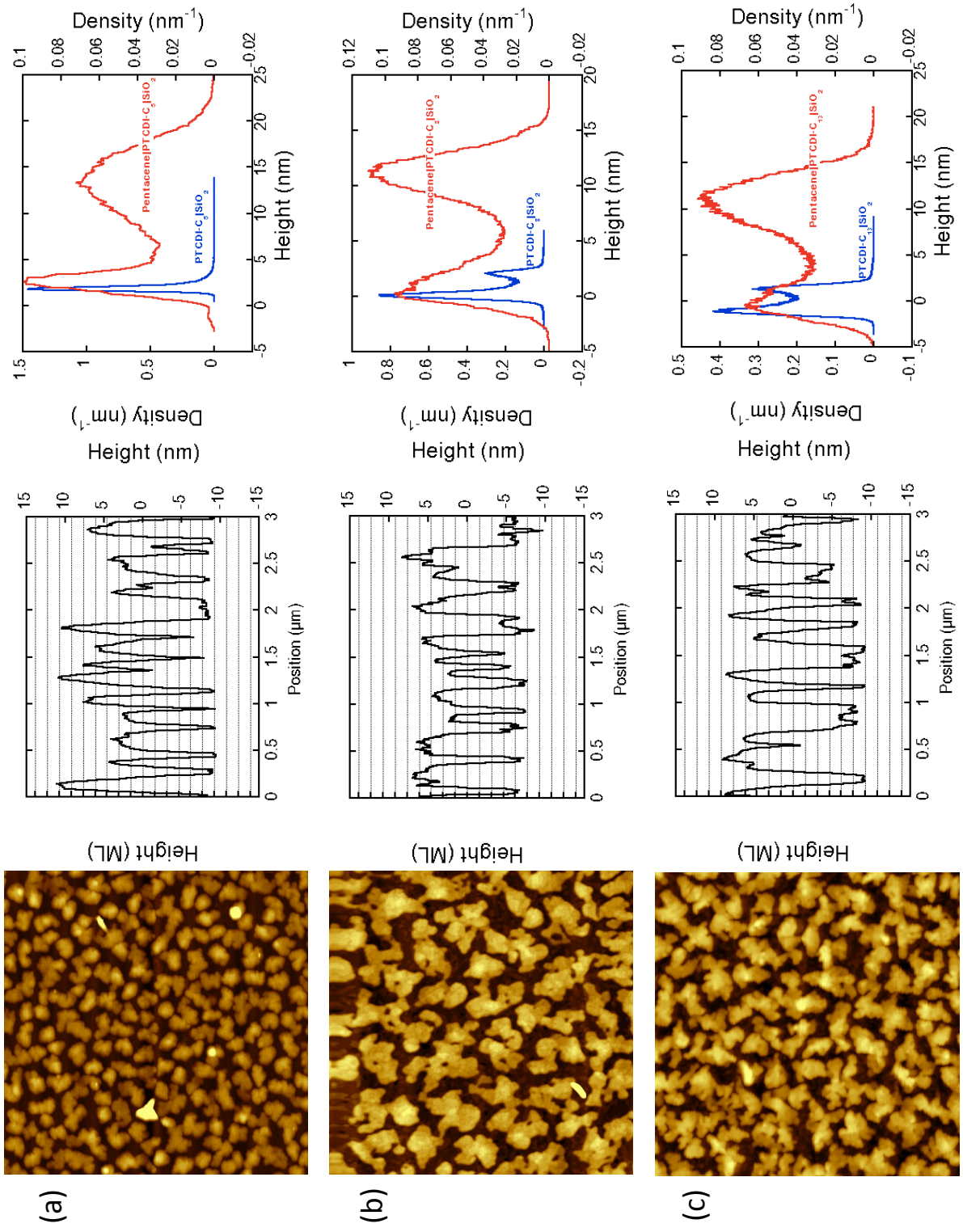

Figure 5.8: Example set of 3μm x 3μm atomic force micrographs of thin films of (a) PTCDI-C_5 (b) PTCDI-C_8 and (c) PTCDI-C_{13}, grown on a pre-deposited monolayer of pentacene. Line profiles are shown accompanying each micrograph, as well as height histograms comparing the deposited 4ML pentacene films to the starting surface of 1ML PTCDI-C_n.

grows layer-by-layer, showing oscillations at the anti-Brag point. Only after growth does the film dewet and reorganize into taller features, increasing film roughness.

The RMS roughness for these films can be calculated from these micrographs. The maximum roughness that can be predicted by the x-ray model is shown as the solid line in Figure 5.9. This corresponds to stochastic or Poisson growth mode where there is no downhill transport due to high Ehrlich-Schwoebel barriers; incident molecules remain in the layer where they adsorb. Also shown in Figure 5.9 are RMS values measured by *ex situ* AFM. This model consistently underestimates the roughness of the films as measured by AFM. This suggests that not only is there no downhill transport occurring during film growth, but that uphill transport is possibly a factor. Pentacene is likely growing here in a Volmer-Weber mode. sIt is not clear whether this occurs during growth, or as part of a post-growth reorganization process, as has been observed for pentacene on low-energy surfaces.

While the pentacene films are extremely rough, having grown in a three-dimensional manner, *ex situ* XRR data taken at the G2 station of the Cornell High Energy Synchrotron Source, shown in Figure 5.10, reveal Bragg peaks of pentacene. So although pentacene is not growing layer-by-layer and not wetting the PTCDI-C_n surface, it is still forming a crystalline film. However, the peaks are broad and relatively weak, with no Laue oscillations, suggesting that the crystallite sizes are quite small.

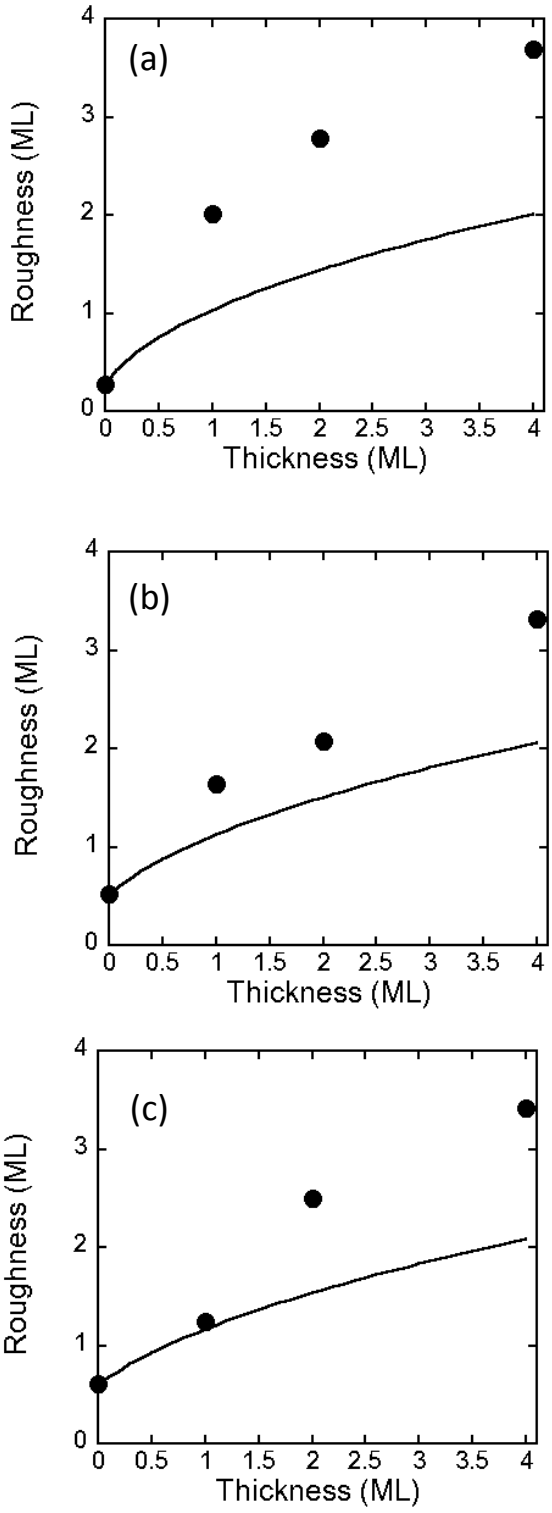

Figure 5.9: Thin film roughness as a function of film thickness for pentacene films grown on 1ML films of (a) PTCDI-C_5 (b) PTCDI-C_8 and (c) PTCDI-C_{13}, as predicted by purely stochastic (Poisson) growth. Solid circles represent roughness obtained directly from AF micrographs.

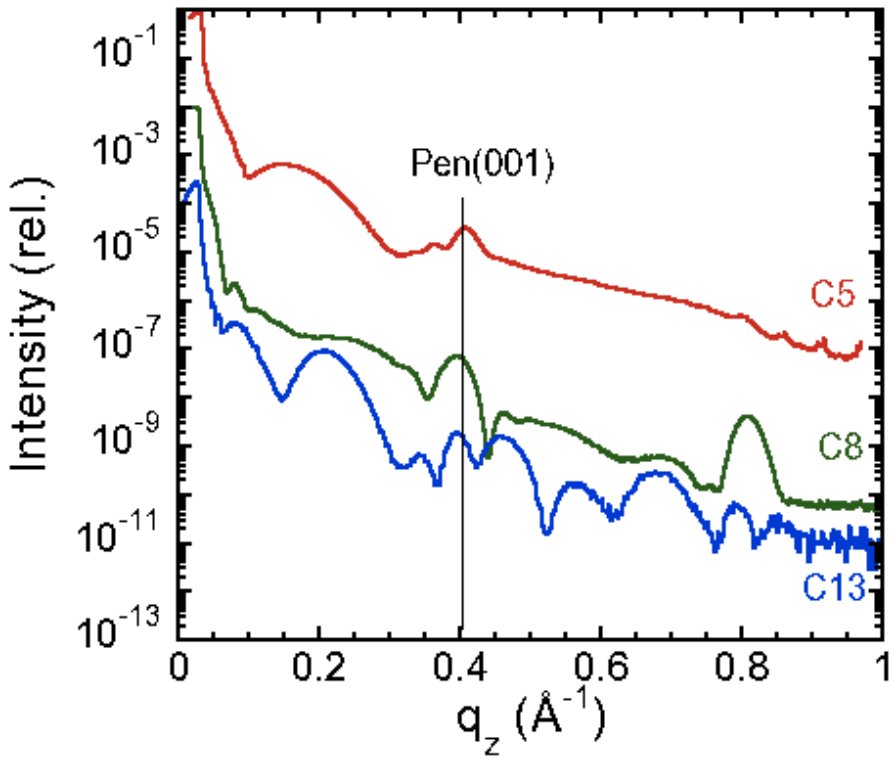

Figure 5.10: Specular X-Ray reflectivity (XRR) of each of the films shown in Figure 5.8. Data offset for clarity.

5.4.3 Multilayer structures of pentacene and PTCDI-C$_n$

Studying the growth of bilayers has shown that PTCDI-C$_n$ will grow smoothly on pentacene, but pentacene will form rough, three-dimensional features when grown on PTCDI-C$_n$. This result is interesting for its application to forming an interface between *p*-type and *n*-type organic semiconductors. However, a simple bilayer is not considered the ideal structure for an organic photovoltaic device. A large interfacial area is desired to facilitate charge separation, and continuous pathways from the interface to the electrodes are necessary. To study a more complicated device structure, we have deposited films composed of alternating layers of pentacene and PTCDI-C$_n$, then examined these films via AFM and XRR.

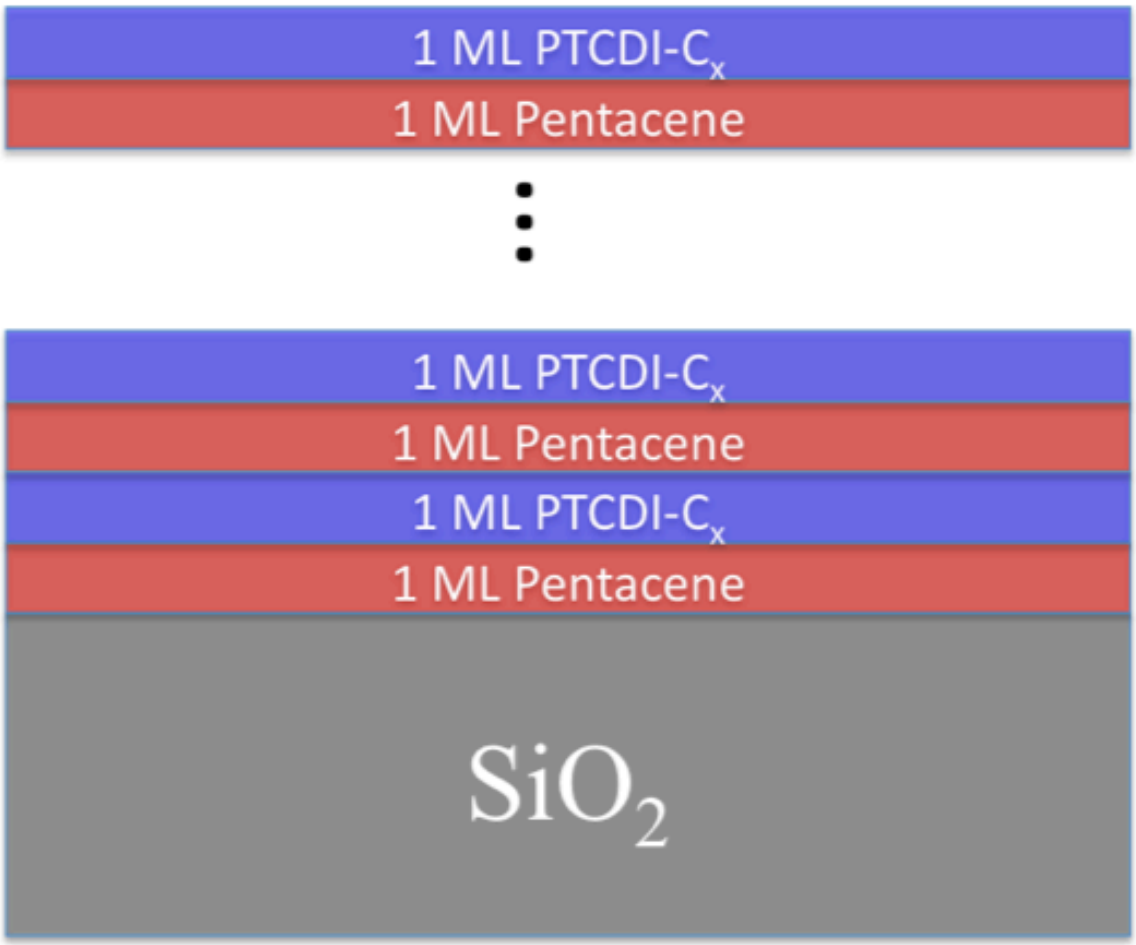

Figure 5.11: Diagram representing the structure of the multilayer films. These films are grown by depositing alternating, single monolayers of pentacene and PTCDI-C$_n$.

Knowing the growth rate from previous real time x-ray studies (*vide infra*), we were able to deposit a single monolayer worth of pentacene, and then a single monolayer of PTCDI-C$_n$. Figure 5.11 shows a schematic representation of the proposed structure. Repeating this, we grew several multilayer films of different thicknesses. These films were then studied by *ex situ* AFM and XRR in the G2 station of CHESS. In Figure 5.12 we plot the roughness measured via AFM against the total number of layers deposited.

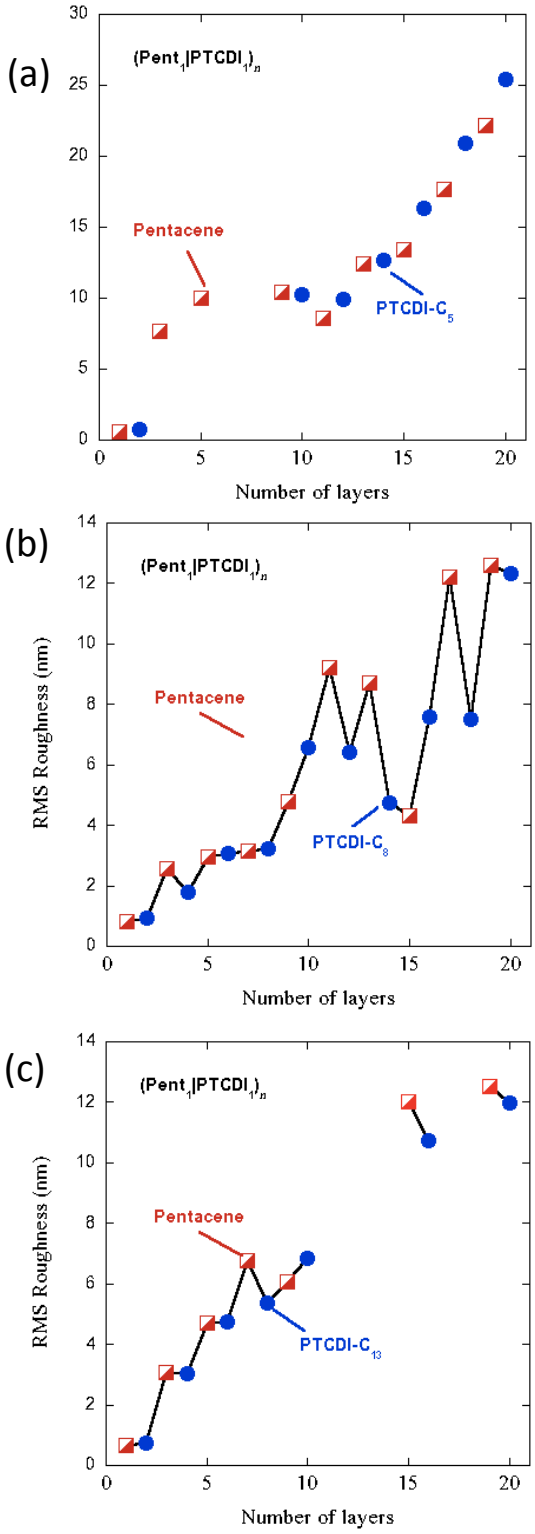

Figure 5.12: Roughness of multilayer stacks composed of alternating layers of pentacene and (a) PTCDI-C_5 (b) PTCDI-C_8 and (c) PTCDI-C_{13}, as obtained by AFM.

For the PTCDI-C_{13}/Pentacene multilayers, an interesting trend can be observed. The roughness of the multilayer film increases after pentacene is deposited, as might be expected from the three-dimensional growth mode observed previously, but the roughness remains the same or even decreases after PTCDI-C_{13} has been deposited. This can be seen more clearly in Figure 5.13(c) where we plot the change in roughness with each additional layer. This effect continues even for films up to 20 layers thick. A similar smoothing effect has also been observed for multilayers of diindenoperylene and perfluoropentacene **[35,36]**.

Thinner PTCDI-C_8 and pentacene multilayers have been reported on by Hiroshiba et. al., as have superlattices of PTCDI-C_8 and other small molecule organic semiconductors **[37,38]**. For the case of pentacene and PTCDI-C_8 we see results similar to the PTCDI-C_{13}/Pentacene multilayers where subsequent layers of PTCDI-C_8 result in a smoother film, at least for the thinner multilayers. However for thicker multilayers, the smoothing effect ceases. But as is the case for PTCDI-C_{13}, the pentacene layers typically result in significantly increased roughness. These effects are more obvious in Figure 5.13(b) where the change in roughness is plotted. The final roughness of the thickest films is comparable to the thickest PTCDI-C_{13}/Pentacene multilayers.

The PTCDI-C_5/Pentacene multilayers do not exhibit this behavior. Each layer that is deposited increases the roughness of the multilayer film. Figure 5.12(c) shows only a monotonic increase in roughness. Additionally, the roughness of these multilayer films is considerably larger than that observed for the PTCDI-C_{13}/Pentacene films. The roughness from the addition of PTCDI-C_5 layers seems to be driven by extremely tall features. A sample AF micrograph

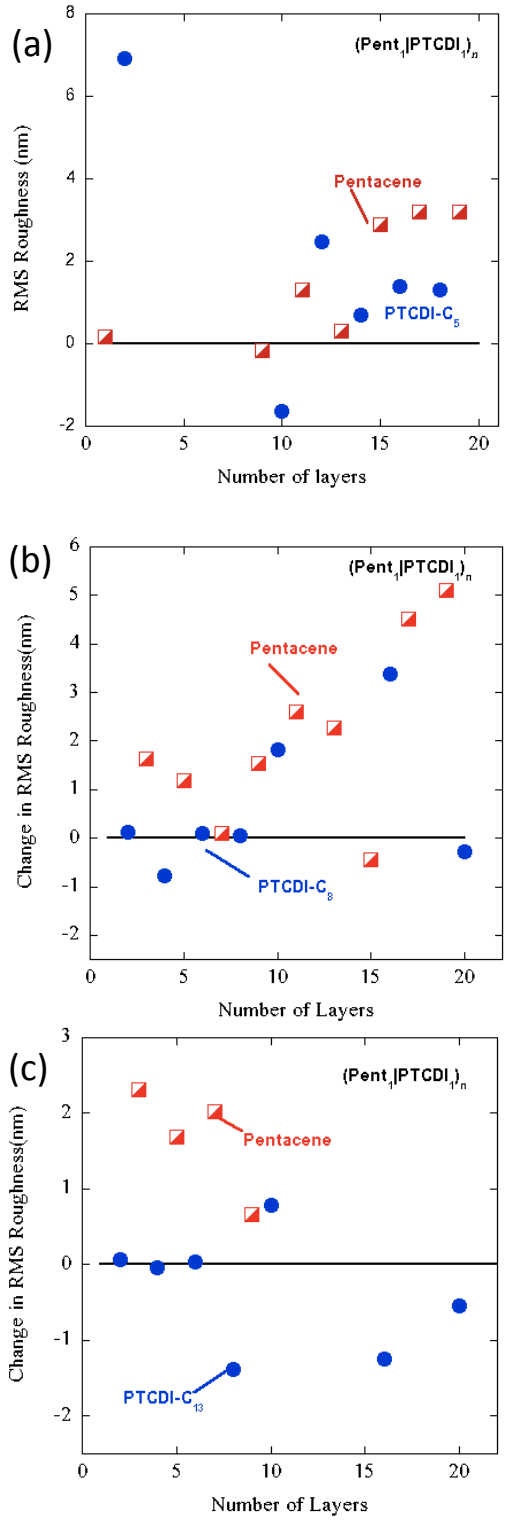

Figure 5.13: Change in roughness of multilayer stacks with each deposited layer of pentacene and (a) PTCDI-C_5 (b) PTCDI-C_8 and (c) PTCDI-C_{13}, as obtained by AFM.

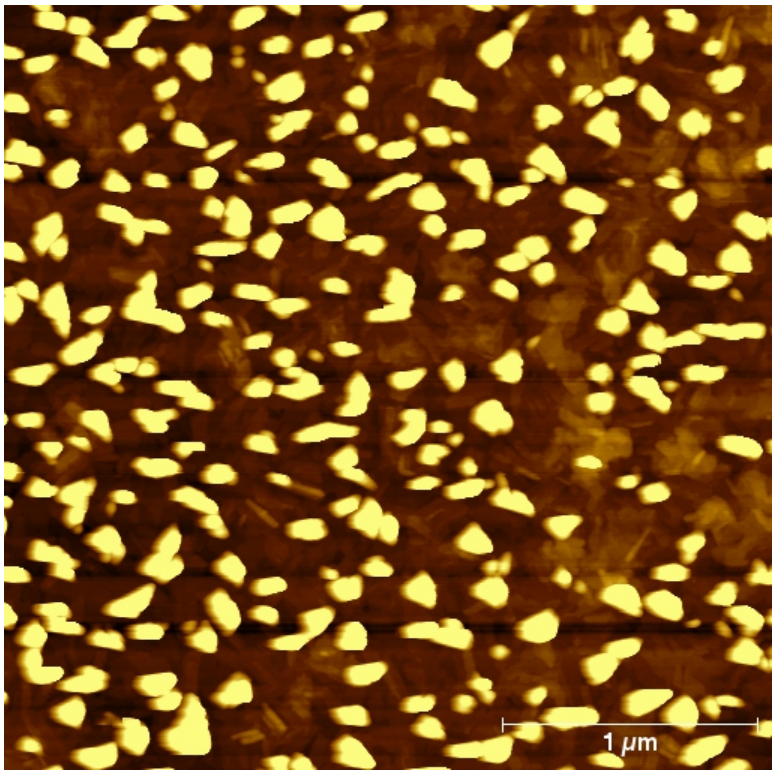

Figure 5.14: Sample 3μm x 3μm AF micrograph of a 5-layer thick PTCDI-C_5/Pentacene thin film, illustrating extremely tall features resulting in rapidly increased roughness.

of a 5 layer film illustrating these features is shown in Figure 5.14. Such obvious, large protrusions are absent from PTCDI-C_8 and PTCDI-C_{13} based heterostructures. In this case, it is not solely the pentacene layers that seem to drive the increase in roughness.

Each of these multilayer films was also examined via XRR, shown in Figure 5.15. The XRR data are difficult to interpret. For the PTCDI-C_5/Pentacene film, we see what could be the (001) and (002) Bragg peaks for both PTCDI-C_5 and pentacene, suggesting that the two materials form separate crystal domains. This idea is supported by the observation of extremely tall, narrow features in the AF micrographs of the PTCDI-C_5/Pentacene multilalyers, as shown in Fig-

ure 5.14. However, as pentacene and PTCDI-C_5 have similar d-spacings, it is difficult to resolve their Bragg peaks.

XRR of the PTCDI-C_8/Pentacene multilayer, shown in Figure 5.15, is similar to that for the PTCDI-C_5 heterostrcuture. A feature can be seen near the (001) peak of PTCDI-C_8, as well as smaller features at higher q_z near the expected (002) peaks for both pentacene and PTCDI-C_8. The XRR data for the PTCDI-C_{13}/Pentacene films in Figure 5.15 is slightly different. No (001) peak is observed for either PTCDI-C_{13} or pentacene, while higher order peaks can be seen. AF micrographs for these films are less enlightening, and no clear features can be seen. Perhaps more telling are the features that are missing from these XRR data. In each case, no Bragg peaks are observed for a superlattice, indicating that these multilayer films do not form smooth, alternating layers, but rather form more complex structures with domains of pentacene and domains of PTCDI-C_n.

5.5 Conclusions

We have examined the growth of heterostructures composed of the *p*-type organic semiconductor pentacene, and three different *n*-type organic semiconductors: PTCDI-C_5, PTCDI-C_8 and PTCDI-C_{13}. Each of the three perylene derivatives exhibits prolonged layer-by-layer growth when deposited on a thin film of pentacene. Additionally, we observe that the longer the alkyl side chain, the sooner the transition to 3D growth. Conversely, when grown on thin films of each PTCDI-C_n molecule, pentacene immediately grows in a 3D fashion, resulting in extremely rough films. The roughness measured via AFM exceeds the

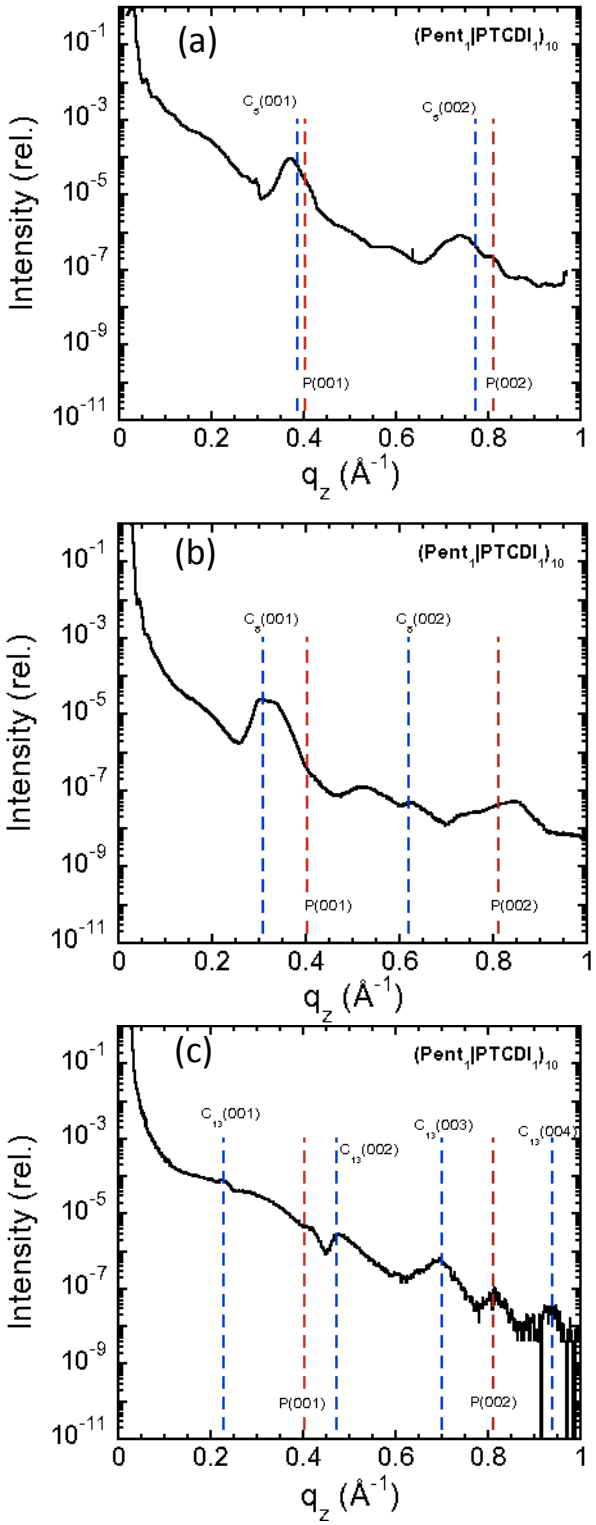

Figure 5.15: Specular x-ray reflectivity (XRR) of the thickest multilayer stacks of pentacene and (a) PTCDI-C_5 (b) PTCDI-C_8 and (c) PTCDI-C_{13}.

roughness predicted by the x-ray growth model, suggesting some sort of reorganization, though whether this occurs during or post film growth is unclear.

For the growth of more complicated multilayers, the analysis is less straightforward. Examining roughness after depositing sequential monolayers reveals an interesting result where layers of PTCDI-C_{13} or PTCDI-C_8 will result in a smoothing of the film, while pentacene layers increase roughness. However, PTCDI-C_5, which grows layer-by-layer longer than the other PTCDI molecules, does not exhibit smoothing behavior. Specular XRR of these multilayers is difficult to interpret, but shows no evidence of ordered superlattice formation.

5.6 References

1. Briseno, A. L.; Mannsfeld, S. C. B.; Reese, C.; Hancock, J. M.; Xiong, Y.; Jenekhe, S. A.; Bao, Z.; Xia, Y. *Nano Lett.*, **2007**, *7*, 2847-2853.
2. Rost, C.; Gundlach, D. J.; Karg, S.; Riess, W. *J. Appl. Phys.*, **2004**, *95*, 5782-5787.
3. Hiroshiba, N.; Hayakawa, R.; Petit, M.; Chikyow, T.; Matsuishi, K.; Wakayama, Y. *Thin Solid Films*, **2009**, *518*, 441-443.
4. Pandey, A. K.; Dabos-Seignon, S.; Nunzi, J. *Appl. Phys. Lett.*, **2006**, *89*, 113506/1-113506/2.
5. Petit, M.; Hayakawa, R.; Wakayama, Y.; Chikyow, T. *J. Phys. Chem. C.*, **2007**, *111*, 12747-12751.
6. Wiatrowski, M.; Dobruchowska, E.; Maniukiewicz, W.; Pietsch, U.; Kowlaski, J.; Szamel, Z.; Ulanski, J. *Thin Solid Films*, **2010**, *518*, 2266-2270.

7. Tang, F.; Chan, J.; Wu, F.; Cheng, H.; Hsu, S. L; Chen, J.; Chou, W. *J. Mater. Chem.*, **2012**, *22*, 22409-22417.

8. Alferov, Z. I. *Semiconductors*, **1998**, *32*, 1-14.

9. Stangl, J.; Holy, V.; Bauer, G. *Rev. Mod. Phys.*, **2004**, *76*, 725-776.

10. Istrate, E.; Sargent, E. H. *Rev. Mod. Phys.*, **2006**, *78*, 455-477.

11. Gudiksen, M. S.; Lauhon, L. J.; Wang, J.; Smith, D. C.; Lieber, C. M. *Nature*, **2002**, *415*, 617-620.

12. Zhou, Y.; Chen, J.; Q. Xu; He L. *J. Vac. Sci. Technol. B*, **2012**, *30*, 051203/1-051203/6.

13. Yang, J.; Yan, D. *Chem. Soc. Rev.*, **2009**, *38*, 2634-2645.

14. Gao, H.; Nix, W. D. *Annu. Rev. Mater. Sci.*, **1999**, *29*, 173-209.

15. Raimondo, L.; Fumagalli, E.; Moret, M.; Campione, M.; Borghesi, A.; Sassella, A. *J. Phys. Chem. C*, **2013**, *117*, 13981.

16. Brabec, C. J.; Sariciftci, N. S.; Hummelen, J. C. *Adv. Funct. Mater.*, **2001**, *11*, 15-26.

17. Lunt, R. R.; Giebink, N. C.; Belak, A. A.; Benziger, J. B.; Forrest, S. R. *J. Appl. Phys.*, **2009**, *105*, 053711.

18. Peumans, P.; Yakimov, A.; Forrest, S. R. *J. Appl. Phys.*, **2003**, *93*, 3693.

19. Pandey, A. K.; Unni, K. N. N.; Nunzi, J-M. *Thin Solid Films*, **2006**, *511*, 529-532.

20. Salzmann, I.; Duhm, S.; Opitz, R.; Johnson, R. L.; Rabe, J. P.; Koch, N. *J. Appl. Phys.*, **2008**, *104*, 114518.

21. Salzmann, I.; Duhm, S.; Heimel, G.; Rabe, J. P.; Koch, N.; Oehzelt, M.; Sakamoto, Y.; Suzuki, T. *Langmuir*, **2008**, *24*, 7294-7298.

22. Roncali, J. *Acc. Chem. Res.*, **2009**, *11*, 1719-1730.

23. Ruderer, M. A.; Mller-Buschbaum, P. *Soft Matter*, **2011**, *7*, 5482.

24. Schroeder, T. W. *Cornell University: Ph.D. Thesis* **2004**.

25. Amassian, A.; Desai, T. V.; Kowarik, S.; Hong, S.; Woll, A. R.; Malliaras, G. G.; Schreiber, F.; Engstrom, J. R. *J. Chem. Phys.* **2009**, *130*, 124701/1-124701/9.

26. Woll, A. R.; Desai, T. V.; Engstrom, J. R. *Phys. Rev. B.*, **2011**, *84*, 075479/1-075479/13.

27. Cohen, P. I.; Petrich, G. S.; Pukite, P. R.; Whaley, G. J.; Arrott, A. S. *Surface Sci.* **1989**, *216*, 222-248.

28. Kowarik, S.; Gerlach, A.; Skoda, M.; Sellner, S.; Schreiber, F. *Eur. Phys. J. Special Topics* **2009**, *168*, 11.

29. Hong, S.; Amassian, A.; Woll, A. R.; Bhargava, S.; Ferguson, J. D.; Malliaras, G. G.; Brock, J. D.; Engstrom, J. R. *Appl. Phys. Lett.*, **2008**, *92*, 253304/1-253301/3.

30. Amassian, A.; Desai, T. V.; Kowarik, S.; Hong, S.; Woll, A. R.; Malliaras, G. G.; Schreiber, F.; Engstrom, J. R. *J. Chem. Phys.*, **2009**, *130*, 124701/1-124701/9.

31. Desai, T. V.; Kish, E. R.; Woll, A. R.; Engstrom, J. R. *J. Phys. Chem. C*. **2011**, *115*, 18221-18234.

32. Vasseur, K.; Cedric, R.; Stijn, V.; Temst, K.; Froyen, L.; Heremans, P. *J. Phys. Chem. C.* **2010**, *114*, 2730-2737.

33. Jang, J.; Nam, S.; Chung, D. S.; Kim, S. H.; Yun, W. M.; Park, C. E. *Adv. Func. Mat.* **2010**, *20*, 2611-2618.

34. Amassian, A.; Pozdin, V. A.; Desai, T. V.; Hong, S.; Woll, A. R.; Ferguson, J. D.; Brock, J. D.; Malliaras, G. G.; Engstrom, J. R. *J. Mater. Chem.*, **2009**, *19*, 5580-5592.

35. Hinderhofer, A.; Gerlach, A.; Kowarik, S.; Zontone, F.; Krug, J.; Schreiber, F. *Euro. Phys. Lett.*, **2010**, *91*, 560021/1-560021/5.

36. Hinderhofer, A.; Hosokai, T.; Frank, C.; Novak, J.; Gerlach, A.; Schreiber, F. *J. Phys. Chem. C.*, **2011**, *115*, 16155-16160.

37. Hiroshiba, N.; Hill, J. P.; Hayakawa, R.; Ariga, K.; Matsuishi, K.; Wakayama, Y. *Thin Solid Films*, **2013**, (in press).

38. Hiroshiba, N.; Morimoto, K.; Hayakawa, R.; Chikyow, T.; Wakayama, Y.; Matsuishi, K. *Chem. Phys. Lett.*, **2011**, *512*, 227-230.

CHAPTER 6

SUMMARY

This thesis has discussed the deposition of small molecule organic semiconductors and the formation of organic-organic heterostructures. Small molecule organic semiconductors are of interest for their ability to form well ordered thin films at low temperatures and on flexible substrates with desirable electronic properties. Potential applications include thin film transistors, OLEDs and display technologies, flexible integrated circuits and photovoltaic devices. This thesis contains a study of the nucleation of organic semiconductors (Chapter 3), the dynamics of adsorption and thin film growth (Chapter 4) and the fabrication of heterostructures (Chapter 5). The following will briefly summarize the observations made.

Chapter three examined the nucleation of DIP and pentacene on SiO_2 surfaces over a range of incident kinetic energies from thermal energy to several eV. For DIP, at each of the incident kinetic energies studied, a critical cluster size of $i^* = 1.67 \pm 0.19$ was found, indicating that two DIP molecules must come together to form a stable island. For pentacene, a critical cluster size of $i^* = 5.18 \pm 2.04$ was observed, which is in agreement with previous studies of pentacene nucleation. For both molecules, it was found that incident kinetic energy plays no role in the size of the critical cluster. This result is easily understood by factoring in the size of the critical nucleus in each case, and the island density. For the growth conditions studied here, this implies that diffusive transport of molecules to the growing islands dominates the dynamics of growth in the submonolayer regime. This also suggests that results obtained for deposition using a supersonic molecular beam can be directly compared to

experiments conducted with a thermal evaporator. It is possible that incident kinetic energy could affect nucleation for a regime where the surface temperature is quite low (resulting in limited surface diffusion) and growth rate is very high, resulting in a greater chance of incident molecules striking islands and imparting their kinetic energy to scatter other admolecules.

Chapter four described a series of experiments probing the adsorption and growth of PTCDI-C_5 and PTCDI-C_8 on SiO_2 surfaces modified with self-assembled monolayers. A modified version of the Cohen model was applied to real time, *in situ* x-ray scattering data in order to characterize the dynamics of growth, and showed that both molecules grow in a layer by layer fashion for several monolayers. For both molecules, the probability of adsorption decreased with incident kinetic energy, demonstrating trapping mediated adsorption behavior. It was observed that the molecules with shorter side chains grew smoother films.

Chapter five examined the formation of heterostructures composed of two different organic semiconductors. The *n*-type organic semiconductors, PTCDI-C_5, PTCDI-C_8 and PTCDI-C_{13} were deposited on monolayer of the *p*-type organic semiconductor, pentacene. All three PTCDI molecules grew in a smooth, layer by layer fashion. PTCDI-C_5 exhibited LbL growth for the longest, up to 18 ML. PTCDI-C_8 displayed LbL growth for up to 12 ML, while PTCDI-C_{13} grew LbL for up to 10 ML, showing that the shortest alkyl side chains are associated with more prolonged layer by layer growth. However, pentacene growth on each molecule was immediately 3D islanded growth, and resulted in extremely rough films, even rougher than would be predicted by purely stochastic growth with no interlayer transport, implying Volmer-Weber growth. After depositing

alternating monolayers of PTCDI-C_n and pentacene, we examined the roughness of the resulting multilayer stacks. After each layer of pentacene, the roughness increased greatly, as to be expected from the results for pentacene growth on PTCDI-C_n. After depositing layers of PTCDI-C_8 or PTCDI-C_{13}, the roughness sometimes decreased. These observations imply that rather than forming an ordered superlattice, separated domains of pentacene and PTCDI-C_n are likely forming. However, PTCDI-C_5 deposition resulted in significant roughness increases. So while PTCDI-C_5 might display the most prolonged layer by layer growth on pentacene, it may not be the best choice for the fabrication of multilayer stacks, as could be found in organic photovoltaic devices.

APPENDIX A

NUCLEATION OF PERYLENE DERIVATIVES ON SELF-ASSEMBLED MONOLAYERS

As described previously, we have studied the adsorption and growth of PTCDI-C_5 and PTCDI-C_8 on SiO_2 surfaces modified with self-assembled monolayers. Here, we present an additional set of experiments studying the nucleation behavior of these two molecules on SiO_2 modified with a self-assembled monolayer of octadecyltrichlorosilane (ODTS).

Self-assembled monolayers of ODTS were deposited as per the procedure described in Chapter 4 for PHTS and NMTS. The produced self-assembled monolayers were examined via contact angle measurements. Previous studies have measured the SAM length and density via XRR measurements **[1]**. Measured contact angles of water and formamide matched those previously recorded in **[1]**. A well formed monolayer of ODTS has been measured to display a water contact angle of 94.3°, a thickness of 17.3 Å, and a 2D surface coverage of 2.83 nm^{-2}.

Thin films of PTCDI-C_5 and PTCDI-C_8 were deposited via supersonic molecular beam. Supersonic molecular beams of PTCDI-C_5 and PTCDI-C_8 (99.8% Sigma-Aldrich Corp.) were generated by passing a carrier gas (He, 99.999%) through a temperature-controlled container (the evaporator) containing these species located upstream of the nozzle (150 μm orifice). The doubly differentially pumped beam passed through a trumpet shaped skimmer into an antechamber and through an aperture that produced a well-defined beam spot on the substrate surface.

Sub-monolayer thin films were deposited at a range of different growth rates. As the supersonic molecular beam produces a well-defined spot on the sample, by translating the sample perpendicular to the deposition sources, up to four distinct thin films could be deposited on a single sample. To assist producing thin films with the desired coverages, the growth of several monolayer thin films was monitored using real time *in situ* synchrotron x-ray scattering at the anti-Bragg ($00^1/_2$) position, which gives a direct measurement of the growth rate. All thin film samples were examined *ex situ* by AFM (Digital Instruments DI-3100) to facilitate a determination of both the density of islands and the total film coverage. In the results reported below we use the thin film coverage measured from AFM and the time of exposure of the sample to the vapor source to calculate the thin film growth rates. A sample series of AF micrographs of sub-monolayer films of PTCDI-C_8 are shown in Figure A.1 and a series of sum-monolayer films of PTCDI-C_5 are shown in Figure A.2.

For a more detailed treatment of nucleation theory, refer to Chapter 3. Using Equation 3.1, we can plot the measured island density as a function of growth rate. Fitting these data to a power law allows us to extract a critical nucleus size. In Figure A.3, we plot the measured island densities as a function of growth rate for PTCDI-C_5 and PTCDI-C_8 on ODTS. The uncertainty in the measured island density can be obtained from the number of islands counted and simple Poisson statistics (cf. Chapter 3).

Previous results have shown that PTCDI-C_{13} nucleation on ODTS requires a critical nucleus size of $i^* = 1$. Indeed, the same critical cluster size was found for a variety of SAMs. Thus, we can reasonably expect that the critical cluster sizes for the nucleation of PTCDI-C_5 and PTCDI-C_8 would also remain constant

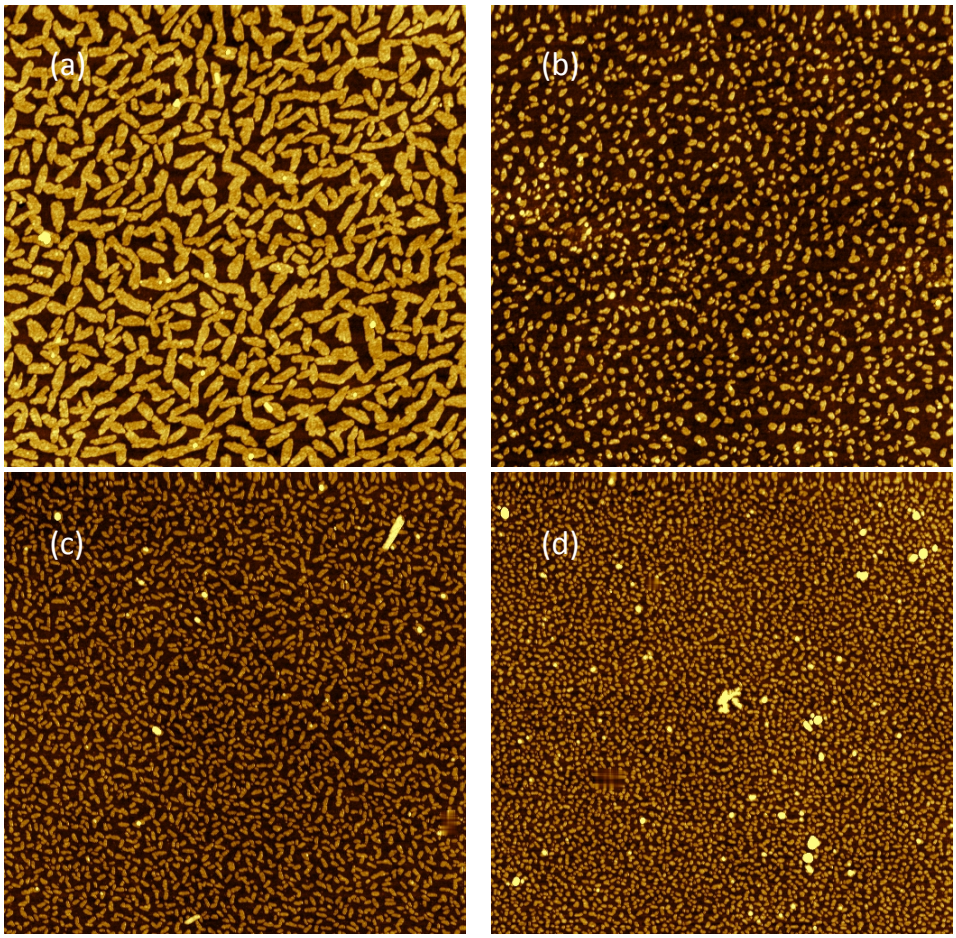

Figure A.1: A series of 5 × 5 μm^2 AF micrographs of sub-monolayer PTCDI-C_8 films grown on SiO_2 modified with ODTS. Changes in island density with growth rate are easily observed. The growth rates and coverages measured for each film are (a) 0.001756 ML-s^{-1} and 0.58 ML (b) 0.004008 ML-s^{-1} and 0.24 ML(c) 0.01551 ML-s^{-1} and 0.31 ML, and (d) 0.03319 ML-s^{-1} and 0.33 ML.

over such surfaces. Due to the structural similarity of all three molecules, it is interesting to compare the critical nucleus results. Both PTCDI-C_5 and PTCDI-C_{13} have displayed the same critical cluster size, where only two molecules must come together to form a stable island. However, PTCDI-C_8 is different, with a measured $i^* = 3 \pm 1.2$. The lowest estimate of i^* is then 2, requiring at minimum three molecules of PTCDI-C_8 to come together to form a stable island. This

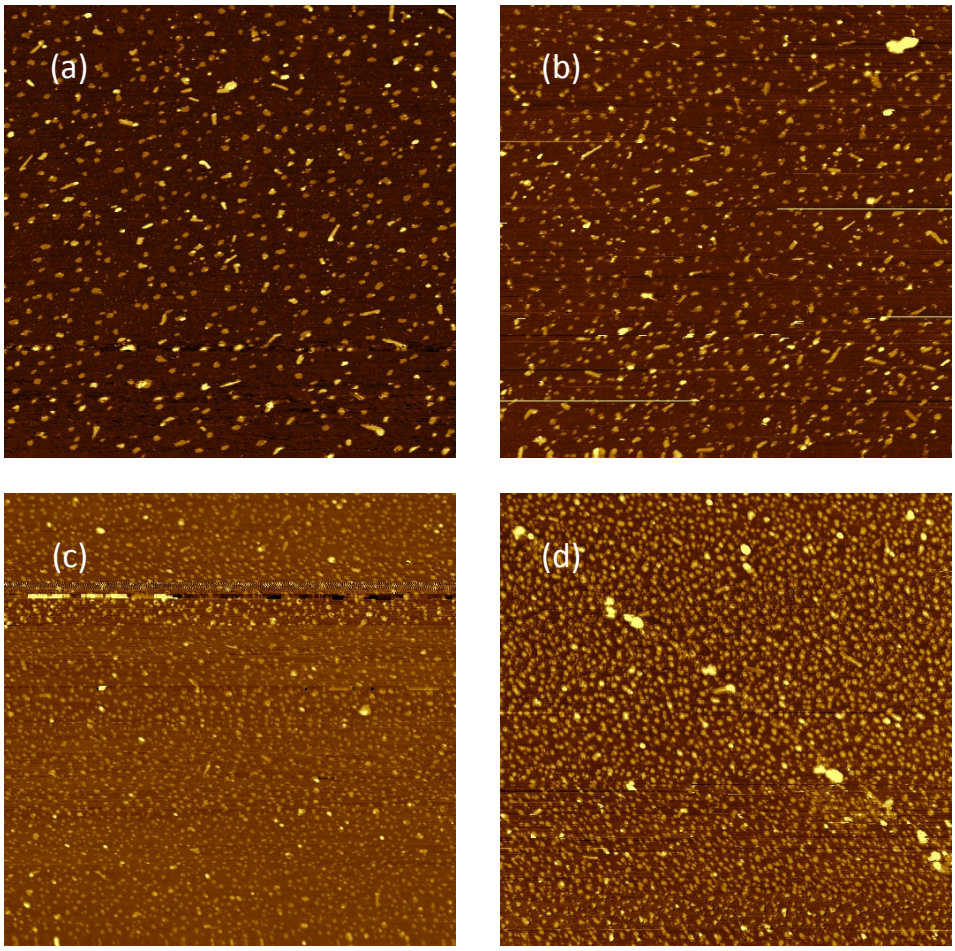

Figure A.2: A series of 5 × 5 μm^2 AF micrographs of sub-monolayer PTCDI-C_5 films grown on SiO_2 modified with ODTS. Changes in island density with growth rate are easily observed. The growth rates and coverages measured for each film are (a) 0.001547 ML-s^{-1} and 0.09 ML (b) 0.01500 ML-s^{-1} and 0.30 ML(c) 0.05584 ML-s^{-1} and 0.45 ML, and (d) 0.1100 ML-s^{-1} and 0.55 ML.

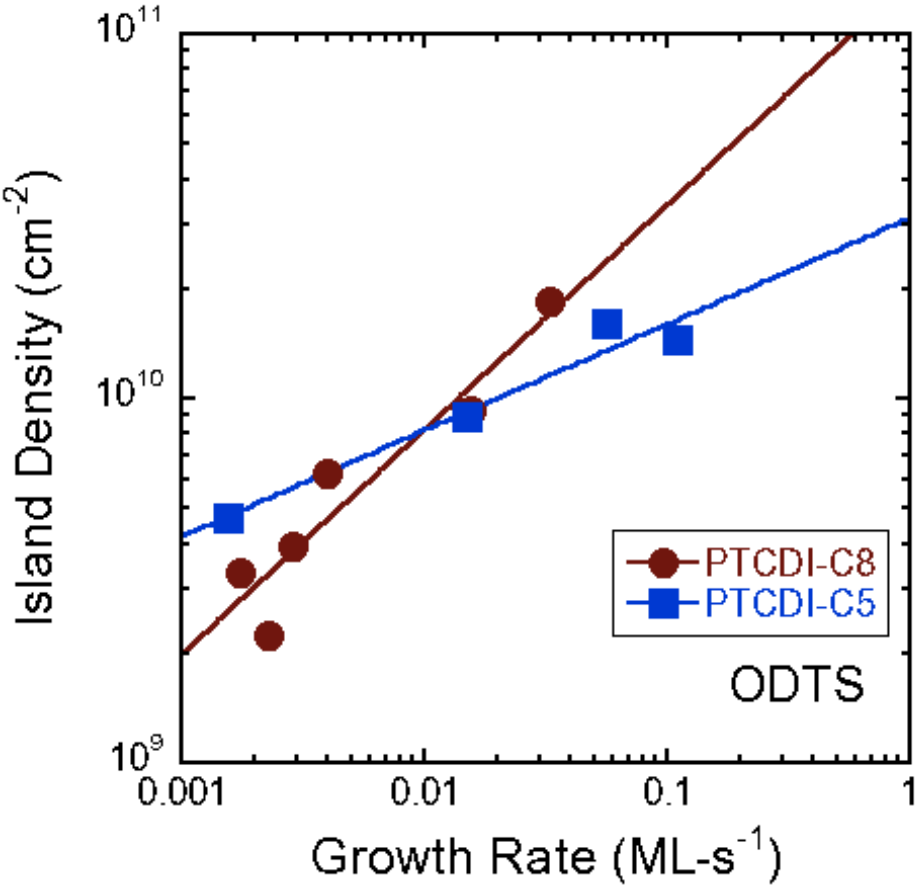

Figure A.3: A plot of island density (as obtained from data such as those shown in Figure A.1 as a function of growth rate for each incident kinetic energy studied. A fit of the data to the power law described by Equation 3.1 is shown as a solid line. From the power law fit, a critical cluster size of of $i^* = 0.8 \pm 0.48$ is obtained for PTCDI-C_5 and $i^* = 3 \pm 1.2$ for PTCDI-C_8

result is more similar to those obtained for pentacene or DIP (cf. Chapter 3).

This discrepancy is difficult to explain. As the size of a critical nucleus depends on the strength of intermolecular interactions, one would expect such similar molecules to all exhibit similar behavior. The nucleation of PTCDI-C_5 and PTCDI-C_8 are not well documented in the literature, and no other studies can be found for comparison. Many of the images here are at relatively high

coverages where islands have begun to coalesce, which makes accurate measurements of island density difficult. Further experiments could help elucidate this phenomenon.

A.1 References

1. Desai, T. V. *Cornell University: PhD Thesis* **2011**.

APPENDIX B

HETEROSTRUCTURES OF DIP AND PTCDI-C_{13}

In addition to studying heterostructures of PTCDI-C_{13} and pentacene, heterostructures of PTCDI-C_{13} and diindenoperylene were also deposited and studied via real time *in situ* x-ray scattering and *ex situ* atomic force microscopy (AFM). As per the procedures described in Chapter 5, supersonic molecular beams of PTCDI-C_{13} (99.8% Sigma-Aldrich Corp.) were generated by passing a carrier gas (He, 99.999%) through a temperature-controlled container (the evaporator) containing these species located upstream of the nozzle (150 μm orifice). The doubly differentially pumped beam passed through a trumpet shaped skimmer into an antechamber and through an aperture that produced a well-defined beam spot on the substrate surface. The mean kinetic energy of the molecules in the supersonic molecular beam can be controlled by adjusting the flow rate of the carrier gas. During deposition the substrate temperature was kept at $T_s \sim 40$°C, and in all cases the supersonic beam was incident along the surface normal.

In addition to the supersonic molecular beam source, we also make use of a conventional thermal effusion source (CreaTec Fischer and Co. GmbH) to generate near thermal energy incident fluxes of DIP. This source possesses a 10 cm^3 crucible constructed of pyrolytic BN, and it is fitted with a pneumatically controlled shutter. In our system, the source is mounted directly to the main scattering chamber of UHV system (angle of incidence is 45° off the substrate surface normal, 10 cm from the substrate surface), which also houses the sample. For deposition from the thermal source a translatable shadow mask, possessing a square 15 × 4 mm^2 opening, ~5 mm from the substrate surface, was used to

define a beam spot on the sample. During these experiments, the thermal effusion source was heated to a temperature (ca. 105 °C) to achieve the desired flux, the shadow mask was moved into place, and the shutter was opened and then closed to produce the desired exposure.

Time-resolved and *in situ* measurements of the scattered x-ray synchrotron intensity were made using a silicon avalanche photodiode detector (APD, Oxford Danfysik, Oxford, UK). During PTCDI-C_n and DIP thin film growth the intensity was monitored at the anti-Bragg position ($q_z = q_{Bragg}/2$), which is an effective monitor of the nature of growth, i.e., layer-by-layer (LbL) vs. 3D islanded growth. Following deposition and x-ray analysis, the samples were removed for *ex situ* analysis using atomic force microscopy (AFM), conducted in tapping mode using a DI 3100 Dimension microscope.

In Figure B.1 we display real time scattering data at the anti-Bragg condition for growth of PTCDI-C_{13} on 1 ML of DIP at 6.3 eV incident kinetic energy. The intensity oscillations at the anti-Bragg condition observed here are expected for layer-by-layer growth due to the alternating contributions of the odd and even layers to the magnitude of the scattered intensity. As can be seen, PTCDI-C_{13} grows in a layer-by-layer (LbL) fashion for several monolayers. In comparison with our previous work PTCDI-C_{13} growth on DIP is remarkably similar to growth on pentacene (cf. Chapter 5).

The kinetics of growth can be modeled more precisely by making use of Equations 5.1 and 5.2, and this result is also shown in Figure B.1. We show the coverage of each layer (solid black curves) predicted by the fit to the intensity oscillations (solid blue line). Using the layer coverages predicted by the fit, the RMS roughness can be calculated and compared to RMS roughness measured

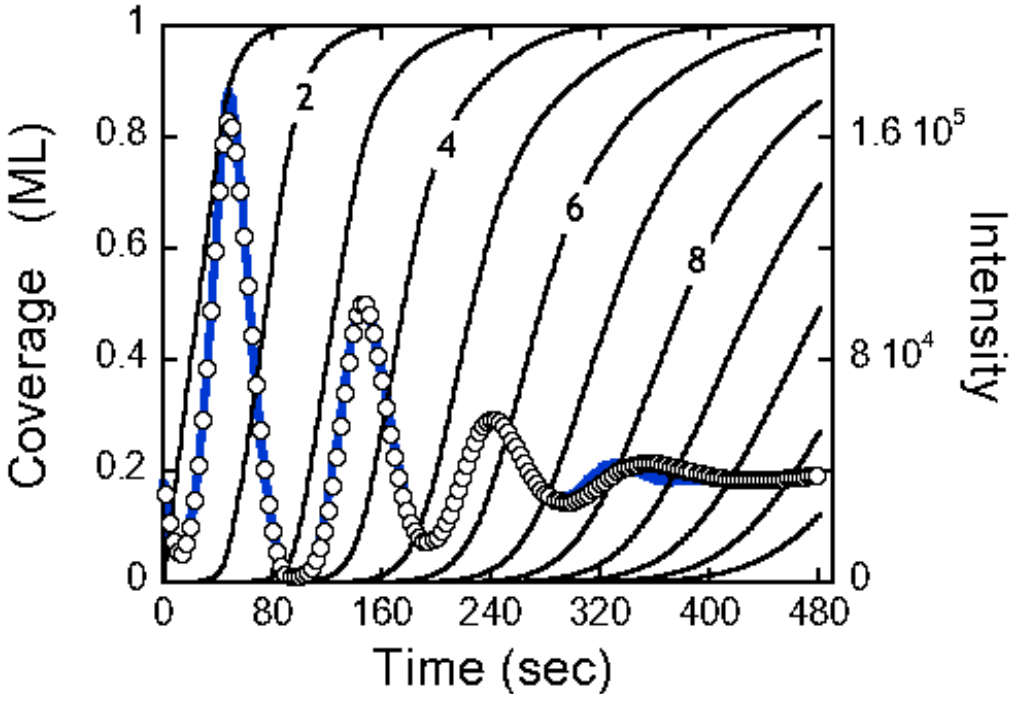

Figure B.1: X-ray intensity at the anti-Bragg condition as a function of exposure to the molecular beam of PTCDI-C_{13}, grown on a predeposited monolayer of DIP. Thick solid lines (right ordinate) indicate a fit of the data to a model, and thin solid curves (left ordinate) represent predicted coverages (θ_n) of the individual layers.

by *ex situ* AFM.

In Figure B.3 we plot the RMS surface roughness of thin films of PTCDI-C_{13} deposited on 1ML of DIP as a function of total coverage as predicted by the fit to the x-ray data (smooth line) for the conditions used to deposit the films displayed in Figure B.1. We also plot the values obtained from the *ex situ* AFM (solid circles). Although the model seems to over predict the roughness compared to AFM, both methods suggest sustained LbL growth of PTCDI-C_{13}. This is also seen for growth of PTCDI-C_{13} on pentacene, plotted in blue. This can be expected due to the structural and chemical similarity of pentacene and

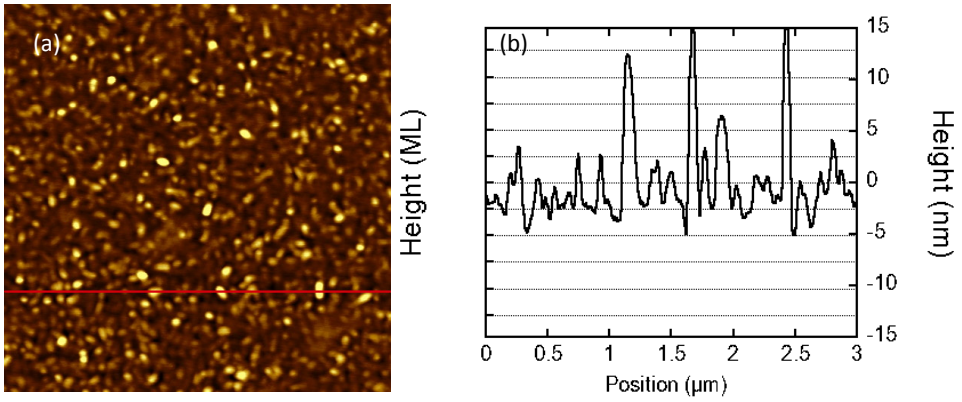

Figure B.2: Example 3μm x 3μm atomic force micrograph of a thin film of PTCDI-C_{13}, roughly 10 ML thick, grown on a pre-deposited monolayer of DIP. A line profile is shown in (b) accompanying the micrograph.

DIP.

On the other hand, when depositing DIP on a monolayer of PTCDI-C_{13}, we see quite different results. The real time x-ray data, presented in Figure B.4, exhibit no oscillations in intensity. Instead, we see a monotonic decrease, indicating the immediate onset of 3D islanded growth, rather than the LbL growth mode typically seen with DIP on SiO_2.

This behavior is quite similar to that observed for the deposition of pentacene on monolayer of PTCDI-C_{13}, as well as pentacene deposited on PTCDI-C_8 and PTCDI-C_5. This is not entirely unexpected, due to the structural similarities of pentacene and DIP. Similar surface energy effects could result in similarly high Ehrlich-Schwoebel barriers or similarly low surface diffusivity, preventing efficient interlayer transport during deposition, resulting in immediate 3D growth.

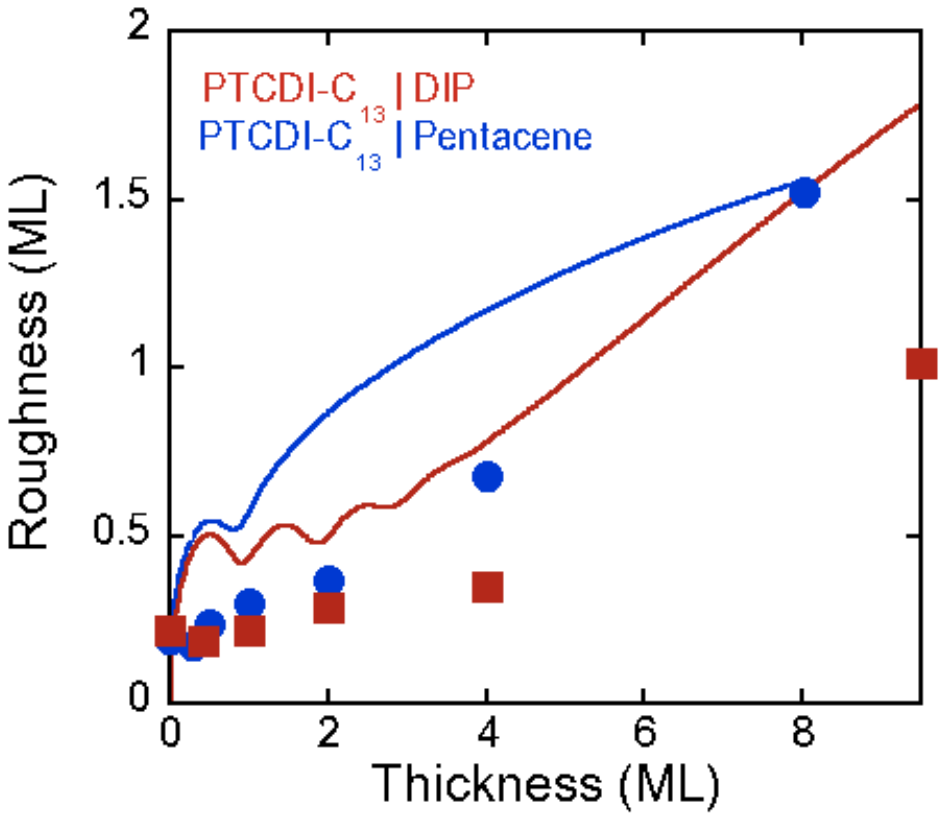

Figure B.3: Thin film roughness as a function of film thickness for PTCDI-C_{13}, grown on a pre-deposited monolayer of DIP as predicted by the fit to the X-ray data plotted in red. Solid squares represent roughness obtained directly from AF micrographs. For comparison, thin film roughness for PTCDI-C_{13} is plotted in blue, with AFM data represented by solid circles.

In addition to real time x-ray scans, *ex situ* x-ray reflectivity (XRR) scans were performed in the G2 station of CHESS. In Figure B.5 we show an XRR scan of a 10 ML thick film of PTCDI-C_{13} deposited on a monolayer of DIP. Four Bragg peaks can be easily seen, corresponding to the (001) through (004) reflections. This, along with the Laue oscillations indicates that a well ordered, lamellar thin film structure has been achieved. For reference, this can be compared to similar results for growth on pentacene (cf. Chapter 5).

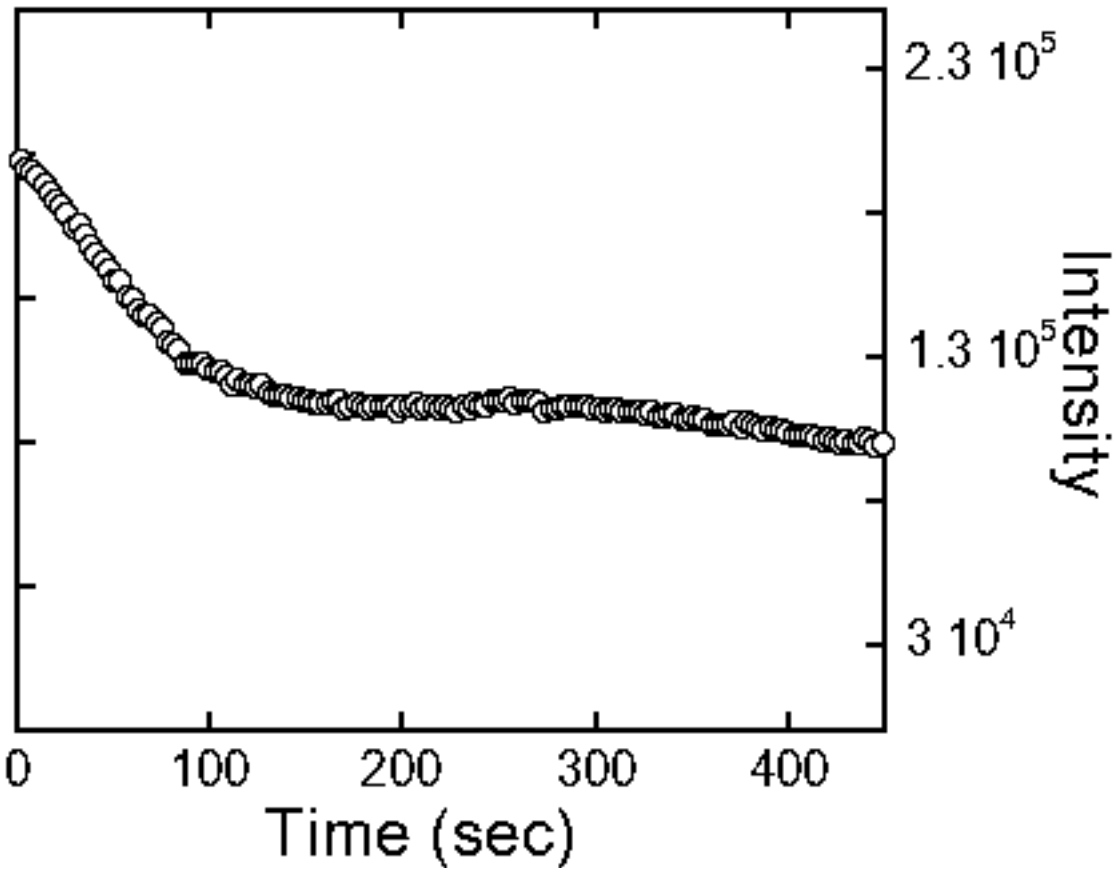

Figure B.4: X-ray intensity at the anti-Bragg condition as a function of exposure to the effusive beam of DIP on a pre-deposited monolayer of PTCDI-C_{13}. Fit to the model not shown here.

In contrast to the clear, unambiguous Bragg peaks of the PTCDI-C_{13} film, XRR of a 4 ML thick film of DIP grown on PTCDI-C_{13} shown in Figure B.6 displays several features which are difficult to identify. Peaks which could represent the (001) reflection appear, but shifted away from the expected d-spacing, however the (002) Bragg peak appears where one would expect. No Kiessig gringes are seen, and the features are broad and not as intense as observed for PTCDI-C_{13}. This indicates that while the DIP film is crystalline, the crystallite sizes are probably small. This would be consistent with a very rough film, as

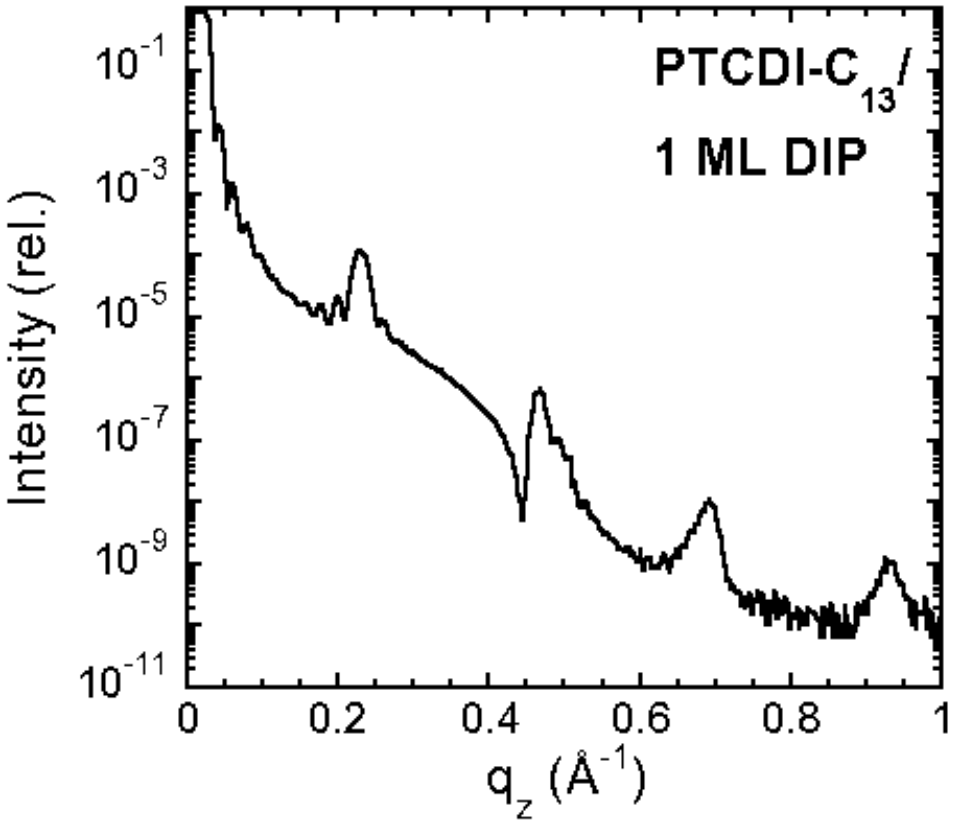

Figure B.5: Specular X-Ray reflectivity (XRR) of a PTCDI-C_{13} film deposited on 1 ML of DIP.

indicated by the 3D islanded growth observed from the real time x-ray data.

Taken all together, the data for heterostructures of PTCDI-C_{13} and DIP exhibits the same basic behavior as that observed for heterostructures of PTCDI-C_{13} and pentacene. PTCDI-C_{13} exhibits smooth, layer by layer growth when deposited on a layer of DIP (or pentacene), but when the order is reversed and DIP is grown on PTCDI-C_{13}, the result is 3D islanded growth resulting in very rough thin films.

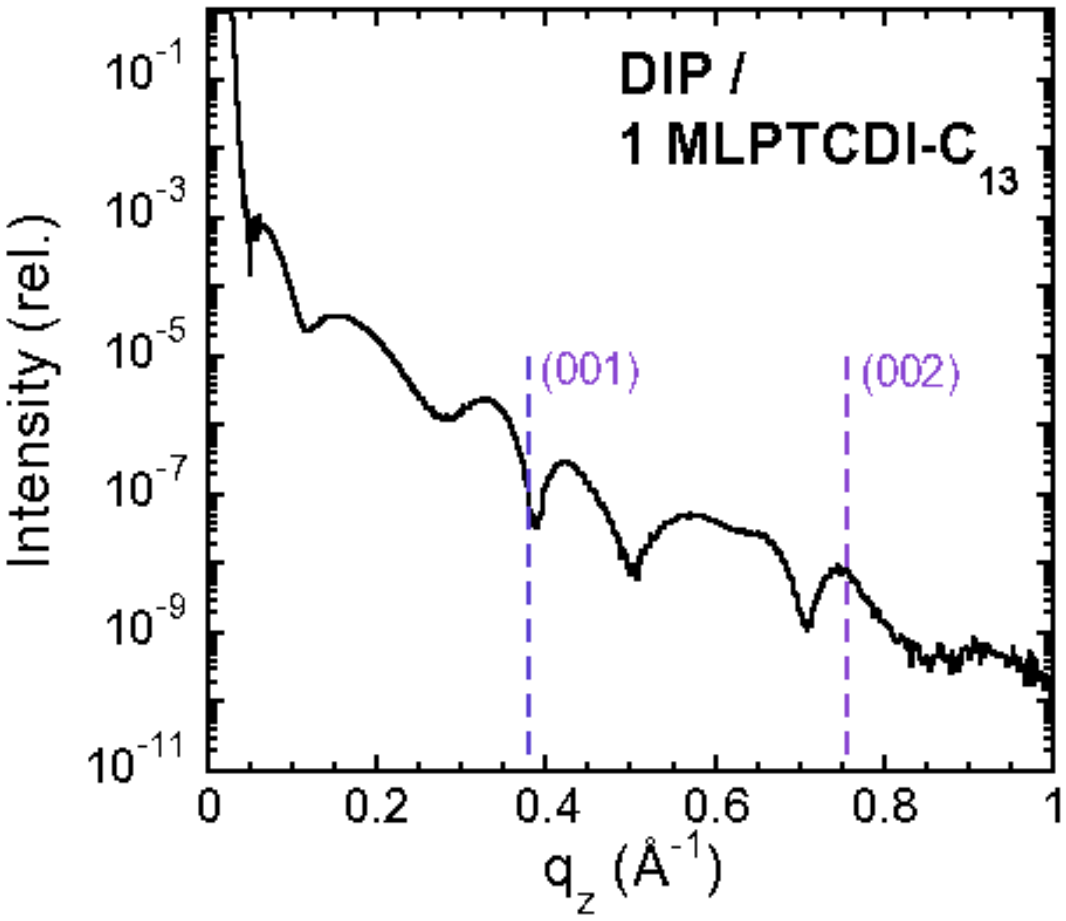

Figure B.6: Specular X-Ray reflectivity (XRR) of a DIP film deposited on 1 ML of PTCDI-C_{13}. Expected location of DIP Bragg peaks shown by dashed lines.

APPENDIX C

PARAMETERS OF THE MODIFIED COHEN MODEL

As described in Section 2.2.4, the real time x-ray data examined in this work is then fit to a modified version of the Cohen model. This appendix presents a sample set of real time x-ray data collected at the anti-Bragg position for the growth of PTCDI-C_8 on HMDS at 5.1 eV (cf. Chapter 4). For a more detailed discussion of the model, as well as a comparison to two similar models, consult reference **[1]**. The parameters of this fit are as follows:

- I_0: Measured x-ray intensity at time $t = 0$. The intensity scale is arbitrary. The data shown here are simply counts per second from the x-ray detector. The intensity data can be normalized if desired.
- ϕ_s: Phase due to substrate, based on the electron density of the substrate material. Typically, values from 2.2 to 2.5 are found to be optimal.
- $\Delta\phi$: Difference in phase between substrate and any interfacial layer (e.g. SAM). Typical values range from -0.6 to 0.2
- P_{film}: Scattering amplitude for the thin film, typical values range from 1 to 4
- R_1: Growth rate of thin film incident on original substrate, S_0F.
- ΔR: Change in growth rate for molecules incident on growing thin film, $S_{n\geq 1}F$.
- ES_1: Energy barrier to downhill transport for molecules to move from layer 2 to layer 1. Negative values mean downhill transport is favored. Typically ranges from 0 to -5

- ΔES_2: Difference between ES_1 and the energy barrier to downhill transport for molecules to move from layer 3 to layer 2
- ΔES_n: The energy barrier for layer transport from layer n+1 to layer n is approached asymptotically, such that $ES_{n\geq 3} = ES_1 + \Delta ES_2 + \Delta ES_n \times \exp((n-2)/N_0)$
- N_0: Controls how quickly ES_n will approach its asymptotic value
- C_{frac}: A parameter that can vary from 0 to 1 which controls the degree of island coalescence. This impacts the calculated step edge density, which affects the rate of interlayer transport. In practice, a C_{frac} value of 1 results in layer coverages asymptotically approaching unity, resulting in larger calculated film roughness.

As an example, the fit to the anti-Bragg data plotted in Figure C.1 was obtained with the following parameters:

- I_0: 40382.6
- ϕ_s: 2.54806
- $\Delta\phi$: -0.0811143
- P_{film}: 1.74143
- R_1: 0.0116264
- ΔR: 0.00355209
- ES_1: -0.113117
- ΔES_2: -0.103986
- ΔES_n: 1.20599
- N_0: 4.43459

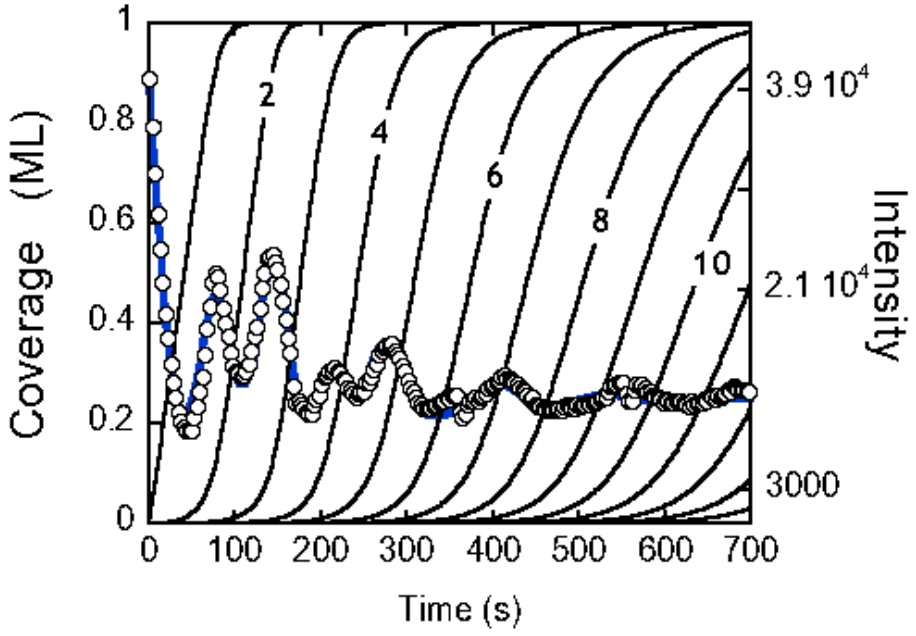

Figure C.1: Scattered x-ray intensity at the anti-Bragg position for growth of PTCDI-C_8 on HMDS at 5.1 eV.

- C_{frac}: 0.262962

For this fit with these parameters, a final χ^2 value of 45.3 was calculated. This is a relatively low value for χ^2, indicating a good fit. The other fits presented in this thesis have values of χ^2 ranging from 5 to 500. Longer thin film growth times, with more data points to fit, tend to produce higher values of χ^2. Longer growth times may also experience slow fluctuations in growth rate due to drift in bubbler or evaporator temperature, or fluctuations in x-ray beam intensity.

C.1 References

1. Woll, A. R.; Desai, T. V.; Engstrom, J. R. *Phys. Rev. B.*, **2011**, *84*, 075479/1-075479/13.

APPENDIX D

SPEC COMMANDS AND MOTOR NAMES

D.1 SIXC

This appendix is intended as a quick reference listing common commands and motor names used in the G3 hutch. SIXC is the software that controls everything in the G3 hutch. It runs on the computer g3hutch, and can be accessed from any networked computer via ssh (username specuser password CThrooMe). To start the program, type 'sixc_ssmb'. There are two versions of sixc, one for our group (ssmb) and one for the Brock group (pld). Upon startup, it will ask you a few yes/no questions. Just give the recommended answers. This should bring you to the command prompt.

D.2 Motors

All the motors are connected to a rack in the northeast corner of the hutch. The names of the motors are as follows:

- *att*: Attenuator position. Zero is no attenuation, 10 is generally enough to block the whole beam.
- *zne*, *znw*, and *zs*: Control the height of the diffractometer table.
- *y*: Controls the horizontal position of the diffractometer table.
- *mu*: Controls the angle of the diffractometer table relative to the x-ray beam (this angle is 2θ in a typical $\theta - 2\theta$ scan).

- *del*: Controls the angle of the diffractometer arm.
- *gamT*: Controls the position of the detector/flightpath on the delta arm.
- *gamR*: Controls the angle of the detector/flightpath on the delta arm.
- *mith*: Upstream mirror. Also affects G2.
- Slit openings: *s1h*, *s1v*, *s2h*, *s2v*, and *csh*.
- Slit positions: *yeast*, *ywest*, *zeast*, *zwest*, and *csx*.
- *zeta*: Controls angle of sample holder. This angle is $-\theta$ in a typical $\theta - 2\theta$ scan. Transfer position is 45, parallel to x-ray beam and perpendicular to supersonic beam is 0.
- *samz*: Controls vertical position of sample holder. Transfer position is -10. Deposition spots are separated by 5mm increments.
- *th*: Controls azimuthal rotation of sample holder. Only used in minor adjustments to ensure sample is vertical.
- *tmask*: Controls position of thermal source mask. Deposition position is around 60, should be at 0 otherwise.

D.3 Commands

For the correct usage of any command, simply type it with no argument, and sixc will give you the proper syntax. At any time, a scan can be stopped by pressing control-c.

- **ascan**: absolute scan of one motor
- **a2scan**: absolute scan of two motors

- **a3scan**: absolute scan of three motors
- **ct**: gives counts per second from each detector
- **dscan**: difference scan of one motor relative to current position
- **d2scan**: difference scan of two motors relative to current position
- **d3scan**: difference scan of three motors relative to current position
- **laser**: print current plot
- **llaser**: print current plot on log scale
- **linplot**: set current plot to linear scale
- **logplot**: set current plot to log scale
- **newfile**: create new data file: **newfile** *filename*
- **plot**: plot current data
- **plotselect**: select which data to plot (e.g. apd, I3, I2)
- **set_lm**: set limits of motion for a particular motor
- **tseries**: acquire data as a function of time: **tseries** *[length of time] [sampling time]*
- **tw**: tweak motor position by a small amount. Mostly used to adjust *mith*
- **udo**: updates any recently edited macro files.
- **umedit**: Opens text editor. Useful for editing macro files.
- **umv**: move motor to absolute position
- **umvr**: move motor relative to current position
- **wm**: returns current position of motor(s)